

**Finite Element Analysis of Damage to Highway Embankments due to Dynamic Subsidence
Resulting from Longwall Mining**

by

Mingzhou Li

Bachelor of Science, Nanjing Forestry University, 2015

Master of Science, University of Pittsburgh, 2017

Submitted to the Graduate Faculty of the
Swanson School of Engineering in partial fulfillment
of the requirements for the degree of
Doctor of Philosophy

University of Pittsburgh

2020

UNIVERSITY OF PITTSBURGH
SWANSON SCHOOL OF ENGINEERING

This dissertation was presented

by

Mingzhou Li

It was defended on

July 22, 2020

and approved by

Luis E. Vallejo, Ph.D., Professor, Departmental of Civil and Environmental Engineering

Anthony T. Iannacchione, Ph.D., Associate Professor,
Departmental of Civil and Environmental Engineering

Jeen-Shang Lin, Sc.D., Associate Professor,
Departmental of Civil and Environmental Engineering

Julie Vanndenbosche, Ph.D., Professor, Departmental of Civil and Environmental Engineering

Patrick Smolinski, Ph.D., Associate Professor,
Departmental of Mechanical Engineering and Materials Science

Dissertation Co-Advisors:

Luis E. Vallejo, Ph.D., Professor, Departmental of Civil and Environmental Engineering

Anthony T. Iannacchione, Ph.D., Associate Professor,
Departmental of Civil and Environmental Engineering

Copyright © by Mingzhou Li

2020

Finite Element Analysis of Damage to Highway Embankments due to Dynamic Subsidence Resulting from Longwall Mining

Mingzhou Li, PhD

University of Pittsburgh, 2020

A coal panel of a longwall mining site was extracted below highway I-70. A 70 ft embankment is located in the center of the panel. This study analyzed the influence of subsidence due to longwall mining on the behavior of this embankment and others along this highway. A Finite Element Method (FEM) that uses ABAQUS, and a field study that employs slope stakes, inclinometers and piezometers were used to analyze its deformation and stability. A user-defined displacement model was applied to the embankment's bottom to simulate the dynamic subsidence. This model was obtained from a regression analysis of the vertical subsidence profile obtained from the Surface Deformation Prediction System (SDPS) software. In the field study, the ARCGIS (Lidar method) was utilized to construct the vertical subsidence contour employing data from the slope stake survey conducted by PennDOT. The embankment deformations from the simulation were compared to those obtained from the field measurements. Both indicated that the location of the maximum subsidence on the embankment was the same.

Using the FEM, a slope stability analysis of the embankment was conducted at each step of the dynamic subsidence. Sections experiencing large deformations were determined. These sections were used for a slope stability analysis employing the shear strength reduction method (SRM). Factors of safety (FS) and their equivalent shear strength reduction factors (SRF) were calculated at these critical cross sections. An FS range was proposed to describe the slope stability of the embankment. The lower bound of the FS range identifies an embankment experiencing

small deformations. The upper bound of the FS range identifies an embankment that experienced large deformations. This upper bound FS developed in response to the strain hardening behavior of the soils. This behavior was obtained from triaxial compression tests. Thus, as a result of the deformations induced by the longwall mining, the embankment became stronger and safer.

Also, a parametric study was conducted to explore the influence that the orientation of the longwall mining and the overburden level have on the deformations and stability of the embankments. It was found that these parameters have a significant influence.

Table of Contents

Acknowledgements	23
1.0 Introduction and Motivation	1
1.1 Subsidence due to Longwall Mining	3
1.2 Geologic Profiles of Embankment #1 and #5	4
1.3 Objectives of the Research.....	8
2.0 Literature Review	11
2.1 Empirical Modeling of Subsidence due to Longwall Mining	11
2.1.1 Basic Characteristics in a Longwall Mining Subsidence Basin	11
2.1.1.1 Potential Maximum Subsidence	11
2.1.1.2 Actual Maximum Subsidence	12
2.1.1.3 Angle of Draw	12
2.1.2 Profile Function.....	13
2.2 Numerical Method in Slope Stability Analysis	14
2.2.1 Introduction to the Shear Strength Reduction Method	15
2.2.2 Implementation of the Shear Strength Reduction Method in ABAQUS.....	16
2.3 Previous Research on the Influence of Longwall Mining Subsidence on Highways in South-West Pennsylvania	17
2.3.1 Field Monitoring	18
2.3.2 Numerical Modeling	20

2.4 Previous Research on the Influence of Longwall Mining on the Slope Stability Problem	21
2.4.1 Field Monitoring	21
2.4.2 Numerical Modeling	23
3.0 Laboratory and Field Investigations of Embankment #1 and Highway I-70	26
3.1 Analysis of Soil Tests	26
3.2 Analysis of Field Monitoring and Surveys	34
3.2.1 Inclinometers	34
3.2.2 Slope Stake Surveys	39
3.2.2.1 Analysis of the Vertical Subsidence on the North-Facing Slope of Embankment #1	39
3.2.2.2 Analysis of Vertical Subsidence on the South-Facing Slope of Embankment #1	41
3.2.2.3 Analysis of Vertical Subsidence on the South-Facing Slope of Embankment #2	43
3.2.2.4 Subsidence Contour Generated by ArcGIS Using the Slope Stake Measurements	46
3.2.3 Piezometers	47
3.2.4 Lidar Surveys	49
4.0 Building up a Three-Dimensional Regression Model of the Ground Subsidence.....	51
4.1 Regression Modeling of the Vertical Subsidence.....	51
4.2 Influence of Topography on the Profile of Subsidence	54

5.0 Developing a Finite Element Model of the Highway Embankment Impacted by Longwall Mining Subsidence.....	60
5.1 Geometry of Embankment #1	60
5.2 Interior Soil Profiles for Different Layers in Embankment #1	63
5.3 Material Properties of the Simplified Layered Finite Element Model.....	67
6.0 Results of Finite Element Analysis of Embankment #1 Subjected to the Successive Subsidence due to Longwall Mining	76
6.1 Deformation Analysis.....	76
6.2 Stress and Strain Field in Embankment #1 due to Subsidence.....	83
6.3 Slope Stability Analysis	85
6.3.1 Potential Critical Cross Section in Embankment #1	86
6.3.2 Factor of Safety of Embankment #1 Impacted by a Successive Subsidence	87
6.4 Sensitivity Tests on the Shear Strength Parameters of Soil and Ground Water Table that Influence the Maximum Subsidence of Embankment #1.....	96
6.4.1 Sensitivity Tests on the Shear Parameters.....	96
6.4.2 Effects of the Ground Water Table on the Behaviors of the Embankment at the Critical Cross Section	100
7.0 Parametric Study	106
7.1 Three-Dimensional Analysis of Embankment #1 with respect to the Longwall Mining Orientation	106
7.1.1 Deformation analysis	107
7.1.2 Slope stability analysis	108

7.2 Three-Dimensional Analysis of Embankment #1 with Different Overburden Thickness.....	111
7.2.1 Deformation Analysis	111
7.2.2 Slope Stability Analysis.....	114
7.2.2.1 Embankment #1 Subjected to Longwall Mining at an Orientation of 35-Degree with respect to the Highway	114
7.2.2.2 Embankment #1 Subjected to Longwall Mining at an Orientation of 90-Degree with respect to the Highway	116
7.3 Chart for the Analysis of the Behavior of Embankment #1 Considering Factors of Safety, Directions of Mining and Overburden Levels	118
8.0 Finite Element Analysis of Embankment #5	121
8.1 Deformation Analysis of Embankment #5	123
8.2 Slope Stability Analysis of Embankment #5	125
9.0 Conclusions.....	134
Appendix A Pseudo Code for Duncan-Chang’s Model in UMAT Subroutine	136
Appendix B Subsidence Contour on Embankment #1	142
Appendix C Factor of Safety for the Case of 0-Degree with Different Overburdens.....	149
Appendix D Subsidence Contour on Embankment #5.....	152
Appendix E Mesh Refinement Tests on Embankment #1.....	157
Bibliography	158

List of Tables

Table 1.1. Basic parameters for Panel 15	3
Table 1.2. Soil type and thickness from Test Boring No. 1 at cross section 720+00 of Embankment #1	8
Table 3.1. Summary of laboratory Shelby tube CU triaxial test results.....	29
Table 3.2. Percentage of rock fragments in samples.....	33
Table 3.3. Original soil properties of different layers of Embankment #1	33
Table 4.1. Overburden of areas near the three positions of longwall face	59
Table 5.1. Parameters utilized in the Duncan-Chang E-v model.....	74
Table 5.2. Material properties of the two-layered Finite Element model of Embankment #1	75
Table 6.1. Shear Parameters in Five cases with resulted maximum subsidence.....	97
Table 7.1. Calculation of the settlements in the embankment with different overburdens	113
Table 7.2. Critical Factor of Safety of Embankment #1 subjected to longwall mining with different overburdens and orientations	120
Table 8.1. Generated jointly random variables of shear parameters and the corresponding factor of safety	131

List of Figures

Figure 1.1. Planview of Panel 15 and locations of two embankments.....	1
Figure 1.2. Overview of highway I-70 and Embankment #1 undermined by Panel 15.....	2
Figure 1.3. Columnar diagrams of two core test holes of the strata above the Pittsburgh coalbed in southwestern Pennsylvania [4]	4
Figure 1.4. Geometry of Embankment #1 in two and three dimensions	5
Figure 1.5. Geometry of Embankment #5 in two and three dimensions	6
Figure 1.6. Variation in the N60 of soil in Test Boring No. 1 at cross section 720+00 of Embankment #1	7
Figure 2.1. Cross section of a subsidence basin illustrating the angle of draw [10]	13
Figure 2.2. Longwall panels which have influenced the interstates in south western Pennsylvania [25]	18
Figure 2.3. Dynamic subsidence projected to z-plane [29].....	19
Figure 2.4. Coordinate system of the panel [29].....	20
Figure 2.5. Location of the bench mark [33]	22
Figure 2.6. Over view of the subsidence with an embankment on it [29]	24
Figure 3.1. Locations of test borings at two cross sections 720+00 and 720+50 of Embankment #1.....	26
Figure 3.2. Geometry of layered Embankment #1 in two dimensions at cross sections (a) 720+50 and (b) 720+00.....	27
Figure 3.3. Locations of Shelby tubes at cross sections (a) 720+50 and (b) 720+00.....	28

Figure 3.4. Stress strain relationship of soil sample in Embankment #1 Fill from lab results	29
Figure 3.5. Configurations and locations of the gravelly silt at (a) TB-6, on the crest of the embankment and (b) TB-7, in the middle of the embankment at cross section 720+50...	31
Figure 3.6. Configurations and locations of the gravelly sand layers at (a) TB-, in the middle of the embankment and (b) TB-4, near the toe of the embankment at cross section 720+00	31
Figure 3.7. Clayey/Silty gravel in the lateral region of embankment at cross section 720+00	32
Figure 3.8. Original soil properties versus depth in Embankment #1	34
Fig. 3.9. An overview horizontal displacements along two directions A and B measured by inclinometers in four test borings in Embankment #1	35
Fig. 3.10. Cumulative displacement along A axis measured by inclinometer at TB-8	36
Fig. 3.11. Cumulative displacement along B axis measured by inclinometer at TB-8	37
Figure 3.12. Field measurement of inclinometers(cumulative) after subsidence denoted on a 3D model of Embankment #1	38
Figure 3.13. Locations of slope stakes categorized by groups	39
Figure 3.14. Numbers of selected slope stake survey points located on the north slope of Embankment #1	40
Figure 3.15. Vertical subsidence measured by selected slope stake survey points on the north-facing slope of Embankemnt #1	40
Figure 3.16. Maximum subsidence measured by the slope stake survey points on the north-facing slope of Embankment #1	41

Fig. 3.17. Locations and numbers of slope stakes on the south-facing slope of Embankment #1..... 42

Fig. 3.18. Vertical displacement measured by selected slope stakes on the south-facing slope of Embankment #1 42

Figure 3.19. Maximum subsidence measured by selected slope stakes on the south-facing slope of Embankment #1 at cross section 720+50 43

Figure 3.20. Locations and numbers of slope stake survey points on the south slope of Embankment #2 44

Figure 3.21. Subsidence measured by the slopes stakes on the south-facing slope of Embankment #2 45

Figure 3.22. Maximum subsidnece at the selected slope stake survey points on the south-facing slope of Embankment #2..... 45

Fig. 3.23. Vertical subsidence contour on the highway embankments with face position of mining on 2/14/2019 generated by ArcGIS using the slope stake survey data..... 46

Figure 3.24. An overview of the layout of three piezometers..... 47

Figure 3.25. Ground water level through dates on three piezometers..... 48

Figure 3.26. Plot of the magnitude of rainfall on different dates 48

Figure 3.27. Vertical subsidence of the highway embankment from Lidar scans (a) before mining (b) during mining and (c) after mining..... 50

Figure 4.1. Regression model of the vertical subsidence (a) along the transversal axis; (b) along the longitudinal axis and (c) in three dimensions. (The SDPS data is denoted by the blue solid circles; the numerical regression profile with topography is denoted by colored rectangles)..... 53

Figure 4.2. Three positions of working faces and the corresponding ground surface data sets	55
Figure 4.3. Numerical regression results considering the topography at three longwall face positions (a) 29 January 2019; (b) 5 February 2019 and (c) 14 February 2019.	57
Figure 4.4. The subsidence regression model with topography was compared to that without topography on the following longwall position dates: (a) 29 January 2019; (b) 5 February 2019 and (c) 14 February 2019	58
Figure 5.1. Topography map of Embankment #1	61
Figure 5.2. Overview geometry of Embankment #1	61
Figure 5.3. Geometry of the uniform 3D model of Embankment #1	62
Figure 5.4. Simplified cross section in 3D model obtained from the simplified 2D model at 720+00	64
Figure 5.5. Simplified cross section in 3D model obtained from the simplified 2D model at 720+50	64
Figure 5.6. All twelve control faces in constructing the three-dimensional layered model.	65
Figure 5.7. Configuration of three-dimensional Embankment #1 with two layers	66
Figure 5.8. Overview of the resulted 3-D FE model of Embankment #1 in the Panel 15.	67
Figure 5.9. Variation of shear strength of sand-clay gravels with changes of rock ratios [39] [40]	68
Figure 5.10. Stress-strain relationship for soil forming part of Embankment #1	73
Figure 5.11. Comparison between the laboratory test and the Duncan-Chang model in the stress -strain curve	74
Figure 6.1. Numerical regression of a 3D subsidence basin	77

Figure 6.2. Locations of the working face on different dates.....	78
Figure 6.3. Subsidence on Embankment #1 subjected to successive subsidence on selected dates.....	79
Figure 6.4. Subsidence on the highway Embankment #1 due to longwall mining from (a) Finite Element model (b) field measurement and (c) Comparison between the two on the crests.....	80
Figure 6.5. Comparison between the measured and simulated vertical displacement at the crest of a highway embankment on different dates	81
Figure 6.6. Simulated vertical displacement of a highway embankment at the critical transversal cross section with maximum subsidence on different stages of subsidence... 	82
Figure 6.7. Simulated vertical displacement of a highway embankment at the longitudinal cross section along the southern edge of highway on different stages of subsidence.....	82
Figure 6.8. Vertical stress inside Embankment #1 at the critical transversal cross section on different stages of subsidence.....	84
Figure 6.9. Principal tensile strain at the critical transversal cross section of Embankment #1 at different stages of dynamic subsidence.....	85
Figure 6.10. Critical cross section for the factor of safety analysis	87
Figure 6.11. Total displacement at the crest of the critical cross section versus the shear strength reduction factor for the case without subsidence.....	88
Figure 6.12. Shear band at the critical cross section from SRM	88
Figure 6.13. Failure surface and the factor of safety calculated by LEM in SLIDE using the same material properties (FS=3.4 in SLIDE).....	89
Figure 6.14. Embankment #1 subjected to subsidence #4.....	90

Figure 6.15. Total displacement at the crest of the critical cross section versus the shear strength reduction factor for the case of working face position #4 91

Figure 6.16. Plastic strain at the critical cross section with SRF equals to (a)1.1 ;(b)1.5 ;(c)2.2 and (d)3.4 92

Figure 6.17. Horizontal displacement perpendicular to the highway direction at the critical cross section with SRF equals to (a)1.1 ;(b)1.5 ;(c)2.2 and (d)3.4..... 92

Figure 6.18. Plot of factor of safety versus the number of working face position when the orientation of highway is 35-degree with respect to the direction of mining and the overburden is 675-ft..... 95

Figure 6.19. Subsidence contour of Embankment #1 generated using the field measurement from the slope stake surveys 98

Figure 6.20. Final simulated vertical subsidence contours on Embankment #1 in Case #2 (units:ft) 98

Figure 6.21. Final simulated vertical subsidence contours on Embankment #1 in Case # (a) 0;(b) 1;(c) 3;(d) 4 (units:ft) 99

Figure 6.22. Two elevations of the phreatic surface at TB-7 indicated by pore water pressures (units:psf)..... 101

Figure 6.23. The elevation of the phreatic surface indicated by the positive pore water pressure resulted from the observed saturation zone (units: psf) 102

Figure 6.24. Total displacement in the Embankment #1 at cross section 720+50 with (a) no water and with phreatic surface at an elevation of (b) 1204-ft; (c) 1208-ft and (d) 1206-ft with field saturated zone (units: ft) 103

Figure 6.25. Total displacement versus the vertical distance between the phreatic surface and the lower toe.....	104
Figure 6.26. Determination of the factor of safety by plotting the total displacement at the crest versus the shear strength reduction factor	105
Figure 6.27. Factor of safety of Embankment #1 at cross section 720+50 with different ground water tables before subsidence.....	105
Figure 7.1. Three angels between the direction of highway and the direction of mining ..	107
Figure 7.2. The vertical subsidence on Embankment #1 when the angle between the orientation of highway and mining is (a) 0-degree; (b) 35-degree and (c) 90-degree (units:ft)	108
Figure 7.3. Plastic strain at the critical cross section of Embankment #1 when the angle between the orientation of highway and mining is (a) 0-degree; (b) 35-degree; and (c) 90-degree with SRF equals to one.....	109
Figure 7.4. Factor of safety for Embankment #1 at different angles with respect to the mining direction	110
Figure 7.5. Plastic strain and deformations inside Embankment #1 when subjected to longwall mining at an angle of 90-degree	110
Figure 7.6. Final vertical subsidence on Embankment #1 subjected to longwall mining with different overburdens (units: ft).....	112
Figure 7.7. Influence of overburden on the subsidence on the ground.....	113
Figure 7.8. Variation of the settlement in the embankment with different overburdens ..	113

Figure 7.9. Plastic strain inside Embankment #1 due to longwall mining with different overburdens of (a) 400-ft; (b)500-ft; (c)600-ft; (d)675-ft at an angle of 35-degree with respect to the highway 115

Figure 7.10. Influence of overburdens on the factor of safety of Embankment #1 at the orientation of 35-degree with respect to the longwall mining..... 116

Figure 7.11. Plastic strain inside Embankment #1 due to longwall mining with different overburdens of (a) 400-ft; (b)500-ft; (c)600-ft; (d)675-ft at an angle of 90-degree with respect to the highway 117

Figure 7.12. Influence of overburdens on the factor of safety of Embankment #1 at the orientation of 90-degree with respect to the longwall mining..... 118

Figure 7.13. Model for the behavior the embankment located in the center of the panel using lower bound FS values, overburden and direction of mining levels 120

Figure 8.1. Topography of Embankment #5 121

Figure 8.2. Regression model of the subsidence basin with an overburden of 500-ft..... 122

Figure 8.3. Working face positions for Embankment #5 123

Figure 8.4. Vertical displacement on Embankment #5 with working face position (a) #0; (b) #4; (c) #5; (d) #8..... 124

Figure 8.5. (a) Plastic strain contours and (b) Displacement inside Embankment #5 after subsidence 125

Figure 8.6. Potential slipping surface of Embankment #5 under gravity indicated by plastic strain..... 126

Figure 8.7. Determination of the factor of safety of Embankment #5 under gravity 126

Figure 8.8. Embankment #5 subjected to subsidence from a developing longwall panel with working face #4 showing the position of the longwall face..... 127

Figure 8.9. Total displacement at the crest of the critical cross section in Embankment #5 versus the shear strength reduction factor for the case with subsidence #4..... 128

Figure 8.10. Rupture surface at the critical cross section when SRF equals to a)0.8 and b)2.8 128

Figure 8.11. Horizontal displacement at the critical cross section when SRF equals to a)0.8 and b)2.8..... 129

Figure 8.12. Factor of safety for Embankment #5 subjected to subsidence with different working face positions 129

Figure 8.13. Distribution of the generated random shear parameters 132

Figure 8.14. Resulting factor of safety calculated in FEM using the random shear parameters 132

Appendix Figure 1 Vertical displacement on Embankment #1 with working face position #0 142

Appendix Figure 2 Vertical displacement on Embankment #1 with working face position #1 142

Appendix Figure 3 Vertical displacement on Embankment #1 with working face position #2 143

Appendix Figure 4 Vertical displacement on Embankment #1 with working face position #3 143

Appendix Figure 5 Vertical displacement on Embankment #1 with working face position #4 144

Appendix Figure 6 Vertical displacement on Embankment #1 with working face position #5
..... 144

Appendix Figure 7 Vertical displacement on Embankment #1 with working face position #6
..... 145

Appendix Figure 8 Vertical displacement on Embankment #1 with working face position #7
..... 145

Appendix Figure 9 Vertical displacement on Embankment #1 with working face position #8
..... 146

Appendix Figure 10 Vertical displacement on Embankment #1 with working face position #9
..... 146

Appendix Figure 11 Vertical displacement on Embankment #1 with working face position #10
..... 147

Appendix Figure 12 Vertical displacement on Embankment #1 with working face position #11
..... 147

Appendix Figure 13 Vertical displacement on Embankment #1 with working face position #12
..... 148

Appendix Figure 14 Variation of the FS of Embankment #1 subjected to subsidence with an orientation of 0-degree and an overburden of 400-ft
..... 149

Appendix Figure 15 Variation of the FS of Embankment #1 subjected to subsidence with an orientation of 0-degree and an overburden of 500-ft
..... 149

Appendix Figure 16 Variation of the FS of Embankment #1 subjected to subsidence with an orientation of 0-degree and an overburden of 600-ft
..... 150

Appendix Figure 17 Variation of the FS of Embankment #1 subjected to subsidence with an orientation of 0-degree and an overburden of 675-ft..... 150

Appendix Figure 18 Influence of overburden on the factor of safety of Embankment #1 when the highway orientation with respect to the mining is 0-degree 151

Appendix Figure 19 Vertical displacement on Embankment #5 with working face position #0..... 152

Appendix Figure 20 Vertical displacement on Embankment #5 with working face position #1..... 152

Appendix Figure 21 Vertical displacement on Embankment #5 with working face position #2..... 153

Appendix Figure 22 Vertical displacement on Embankment #5 with working face position #3..... 153

Appendix Figure 23 Vertical displacement on Embankment #5 with working face position #4..... 154

Appendix Figure 24 Vertical displacement on Embankment #5 with working face position #5..... 154

Appendix Figure 25 Vertical displacement on Embankment #5 with working face position #6..... 155

Appendix Figure 26 Vertical displacement on Embankment #5 with working face position #7..... 155

Appendix Figure 27 Vertical displacement on Embankment #5 with working face position #8..... 156

Appendix Figure 28 Mesh refinement tests with respect to the vertical subsidence 157

Appendix Figure 29 Mesh refinement tests with resepect to the vertical stress 157

Acknowledgements

First, I would like to express my deep appreciation to the thesis advisors, Dr. Luis E. Vallejo and Dr. Anthony T. Iannacchione for their valuable instructions and encouragement throughout the procedure of this research.

Dr. Jeen-Shang Lin, Dr. Julie Vandebossche and Dr. Smolinski are appreciated for their previous advice and for serving as the thesis committee members.

I am rather thankful to Emily Adelson and Robert Winn for their great help in SDPS and ArcGIS respectively in this study.

Roy Painter, P.E., Geotechnical Engineer from PennDOT District 12 and other participants in the study WO 16 are acknowledged for always providing useful data and comments.

I would also thank Dr. Xiangnan Qin, Dr. Jie Yang, and Dr. Zhiqiang Lai for providing generous help in ABAQUS in this study.

Lastly, I am grateful to my parents and my wife Xuewen Yao for their love and support.

1.0 Introduction and Motivation

Longwall mining coal panels were extracted from the Alliance Coal's Tunnel Ridge mine in Washington County, Pennsylvania in early 2019 [1] [2]. Panel 15 went through a segment of interstate highway I-70 between the West Virginia/Pennsylvania (WV/PA) border and West Alexander interchange. Fig. 1.1 depicts the overview of Panel 15 and the future panels that will be mined under the interstate highway I-70.

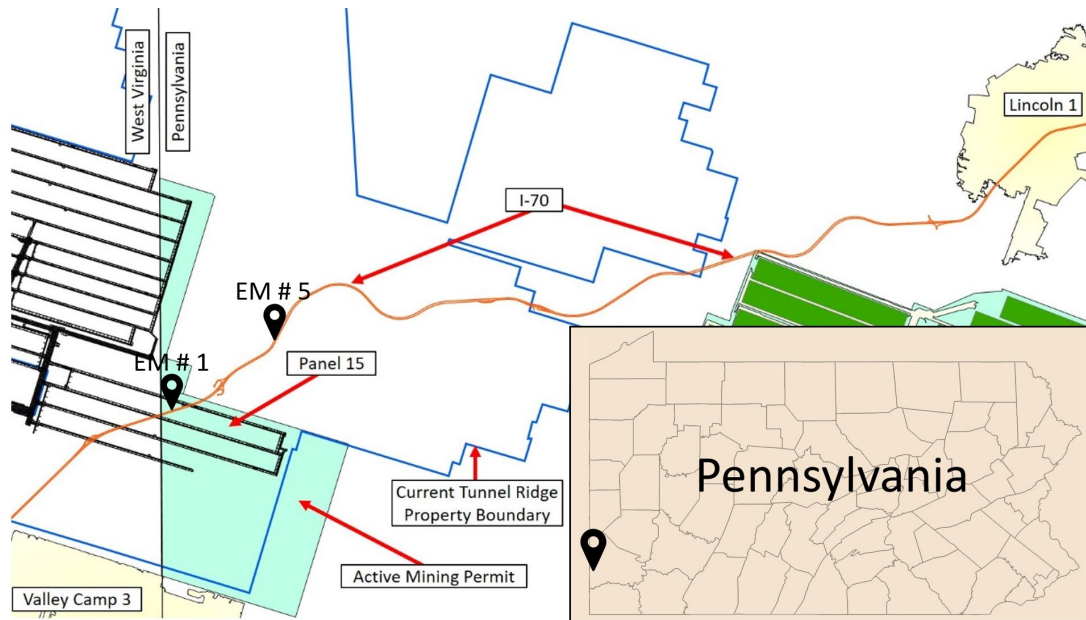


Figure 1.1. Planview of Panel 15 and locations of two embankments

Embankment #1 is located in the middle of Panel 15 shown in Fig. 1.2. The subsidence caused by longwall mining with an overburden of 675 ft took place below this embankment. The direction of the long axis of Embankment #1 (which is the same as the direction of Highway I-70) with respect to the direction of mining is 35° . Numerical analysis was conducted to investigate the

deformation and slope stability of the highway embankment on I-70 due to longwall mining subsidence. A field study was conducted by Penn DOT that involved collecting data related to the deformation of the embankment from slope stake surveys, inclinometers, piezometers, and LIDAR surveys [1] [2].

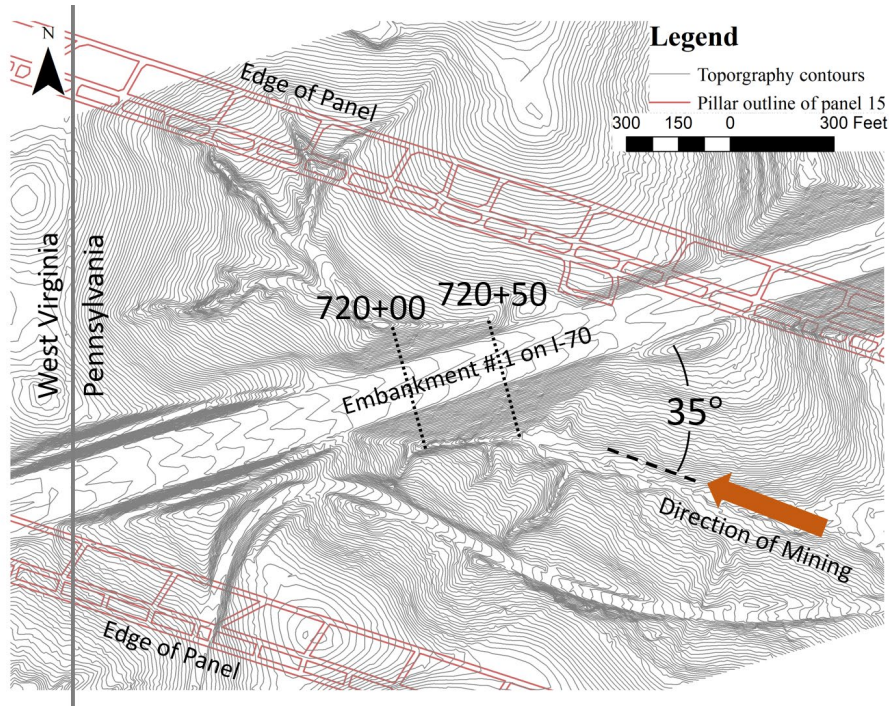


Figure 1.2. Overview of highway I-70 and Embankment #1 undermined by Panel 15

The methodology used to analyze Embankment #1 will also be employed to analyze the deformation and stability due to longwall mining induced subsidence of other embankments located along Highway I-70.

1.1 Subsidence due to Longwall Mining

Background knowledge of subsidence due to a longwall mine is introduced here. When a panel of longwall mining is excavated, a large void is produced in the coalbed. As a result, the immediate roof rock fractures and caves into the recently created void. The strata above the immediate roof rock bends downward. The greater the overburden, the less pronounced the strata bending becomes [3]. Such movements will continue as long as the working face of the longwall mining moves forward, causing a dynamic subsidence basin on the ground surface.

Basic characteristics of Panel 15 subjected to long wall mining are summarized in Table 1.1. In addition, the percentage of hard rock in the strata above the longwall panel is approximately 37% according to the previous core test holes (see Fig. 1.3) in the study area conducted by Jeran and Adamek in 1988 [4]. In this study, a regression model was utilized to fit the subsidence data using genetic algorithm. The subsidence data was obtained from the Surface Deformation Predict System (SDPS) software that was calibrated using field measurements of the site.

Table 1.1. Basic parameters for Panel 15

Average overburden under the highway segment (ft)	Panel length (ft)	Panel width (ft)	Mining height (ft)
675	18,000	1,200	7.25

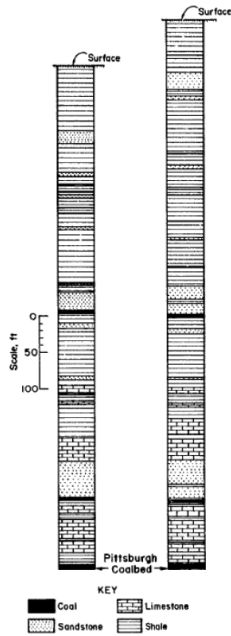
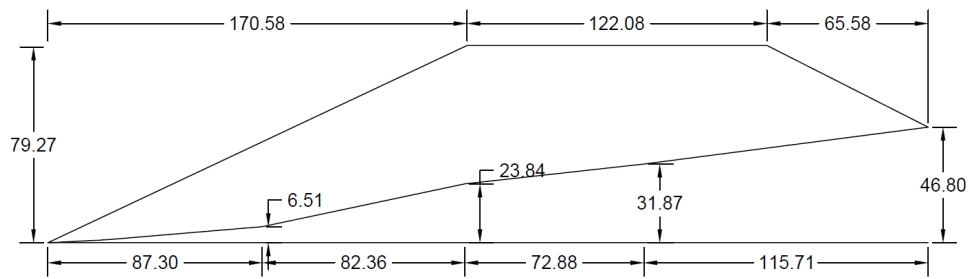


Figure 1.3. Columnar diagrams of two core test holes of the strata above the Pittsburgh coalbed in southwestern Pennsylvania [4]

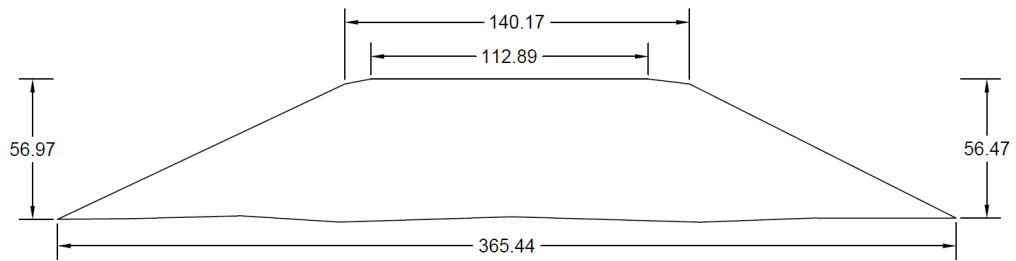
1.2 Geologic Profiles of Embankment #1 and #5

The segment of I70 in the study area is located at the Washington County between the boundary of Pennsylvania/West Virginia and the West Alexander interchange. This section takes a glance at the exterior profiles of the embankment. Besides, the basic configuration of soil that composes the embankment is introduced.

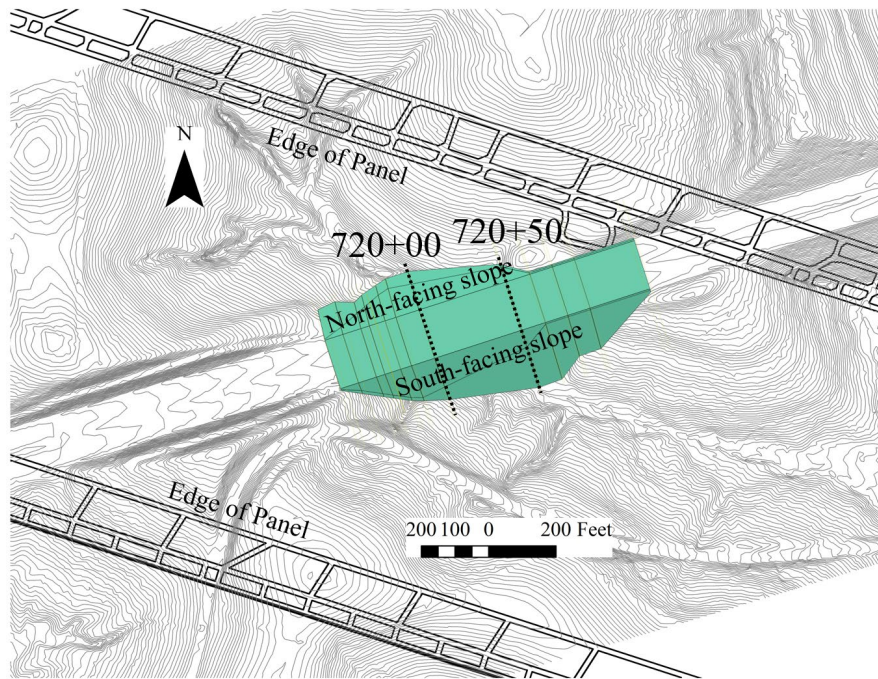
The geometry of two cross sections 720+00 and 720+50 as well as the three-dimensional of embankment #1 are shown in Fig. 1.4. The embankment is 79-ft high from the crest to the lowest toe and 360-ft wide.



(a) Two-dimensional Embankment #1 at cross section 720+50 (unit: ft)



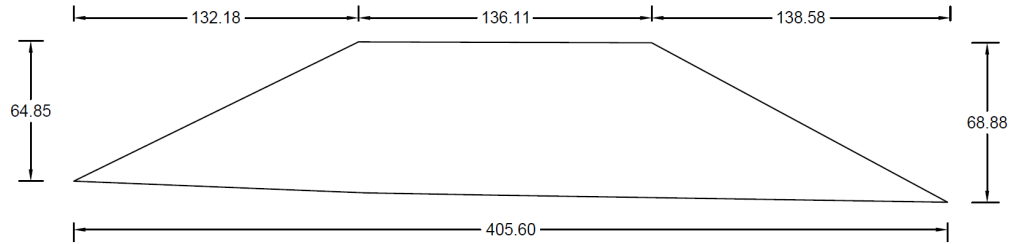
(b) Two-dimensional Embankment #1 at cross section 720+00 (unit: ft)



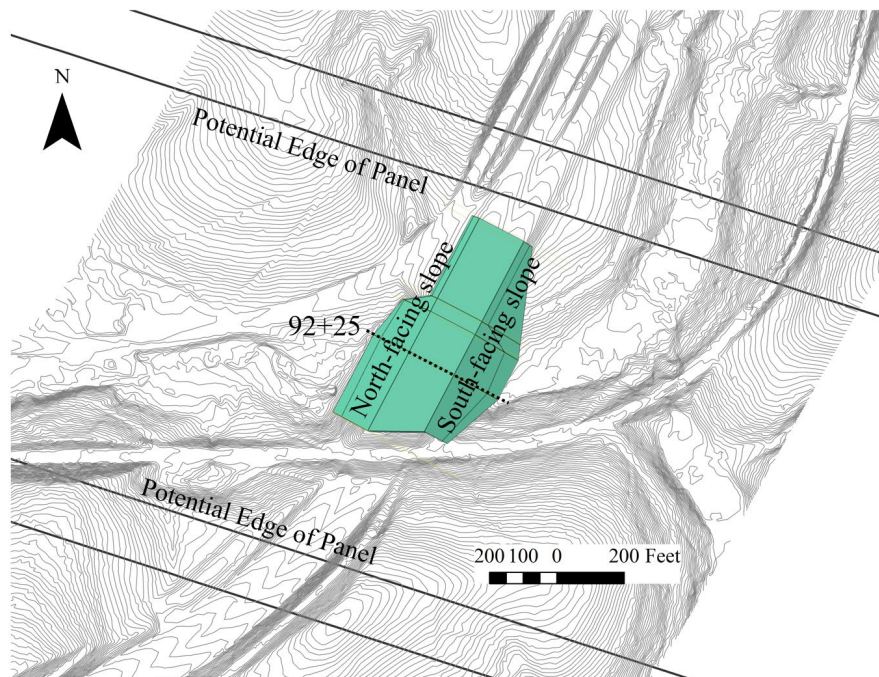
(c) Three-dimensional Embankment #1

Figure 1.4. Geometry of Embankment #1 in two and three dimensions

The cross section 92+25 of Embankment #5 as well as the three-dimensional geometry was shown in Fig. 1.5. The embankment was 68-ft high and 428-ft wide. It is noticed that the slope on both sides of Embankment #5 are identical to that of Embankment #1, around 1(rise):2(run) (26.5°).



(a) Cross section 92+25 of Embankment #5



(b) Three-dimensional Embankment #5

Figure 1.5. Geometry of Embankment #5 in two and three dimensions

According to a geologic profile of southwestern Pennsylvania (Fig. 1.3), the strata in the study area consists of different beds of shale, sandstone, limestone and several thin coal beds.

Embankment #1 was constructed on a valley along Highway I-70. It appears that the original natural material on the ground surface (colluvium) was not removed when constructing the earth embankments according to the existing boring logs (personal communication with Patrick Brown from Earth, Inc.). As shown in Fig. 1.6, Standard Penetration Test (SPT) values collected at the bottom of the embankment above the bedrock also support the existence of the colluvium layer. There is also a layer of mechanically broken rocks at the bottom of the embankment at cross section 720+50. More details about the soil profiles are presented in the field study in Chapter 3.

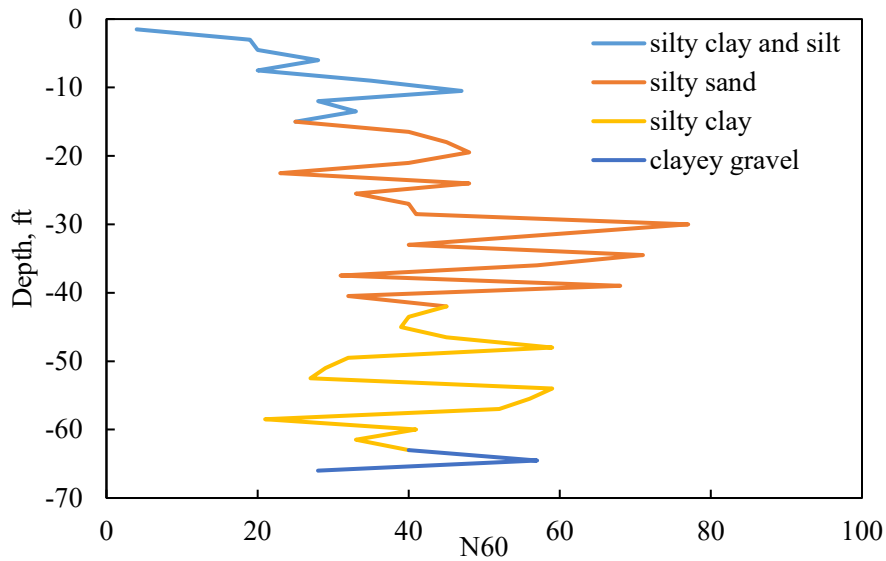


Figure 1.6. Variation in the N60 of soil in Test Boring No. 1 at cross section 720+00 of Embankment #1

The soil boring log from TB-1 on Embankment #1 is shown in Table 1.2. The majority of the soils in the fill are a-6, a-7-6, and a-2-5 in AASHTO definitions. The embankment is constructed of a combination of silt, clay, sand, and some embedded gravel.

Table 1.2. Soil type and thickness from Test Boring No. 1 at cross section 720+00 of Embankment #1

Layer thickness, ft	Soil/Rock type	AASHTO / USCS
15	Silt and Clay	a-7-6 / cl-ml (lean clay - lean silt)
27	Silt and Sand	a-2-5 / sm (silty sand)
6	Silt and Clay	a-7-6 / cl-ml (lean clay - lean silt)
15.5	Silt and Clay	a-6 / cl-ml (lean clay - lean silt)
2.5	Sand and Gravel	a-2-7/ gc (clayey gravel)
0.4	Mechanically broken rock	-
6.9	Siltstone	-
3.1	Limestone	-

1.3 Objectives of the Research

The objectives of this research are:

- To analyze the deformation as well as the slope stability of embankments located on Highway I-70, near the West Alexander interchange as a result of longwall mining using a combination of field and numerical analyses. The emphasis of this research is concentrated on one of the embankments on Highway I-70 (Embankment #1). The methodology used for Embankment #1 is also used to analyze other embankments along I-70.

- To obtain subsidence profiles that will be used for the numerical analysis employing a regression analysis of the profiles obtained from the SDPS method. These subsidence profiles are effective at the bottom of the embankments analyzed.
- To investigate the deformations as well as the slope stability of the embankments. To this end a commercially available finite element method named ABAQUS is utilized. The shear strength reduction method (SRM) implemented into ABAQUS is used to calculate the factor of safety of the embankments. The finite element results of the factor of safety will be validated by applying it to cases that have well-established theoretical results. A sensitivity test of the maximum vertical displacement as well as the factor of safety will be carried out with respect to the size and type of mesh used in the FEM studies.
- To conduct an analysis of field studies on Embankment #1 using data obtained from PennDOT surveys (involving inclinometers, piezometers), elevation measurements using slope stake surveys conducted by the SPK Engineering, and LIDAR scans conducted by T3 Global Strategies, Inc.
- To compare the results of the field studies on Embankment #1 with those obtained using the finite element analysis. This comparison will help in the validation of the numerical model.
- To conduct a sensitivity analysis on the effect of the shear strength parameter values on the deformation and slope stability of the Embankment #1.
- To generate a parametric study on the effect of the direction of longwall mining with respect to the long axis of Embankment #1, as well as the direction of Highway I-70 on the levels of subsidence and stability of this embankment.

- To conduct a parametric analysis on the effect of the overburden depth on the levels of deformation and stability of Embankment #1.
- To conduct a numerical analysis of the deformation and slope stability of other embankments along Highway I-70 using the same methodology utilized for Embankment #1.
- To obtain relationships in the form of graphs relating two parameters (orientation and overburden) and the levels of deformation and factors of safety for the embankments analyzed. These graphs will be very helpful for the prediction of instabilities in highway embankments subjected to future longwall mining in the state of Pennsylvania.

2.0 Literature Review

2.1 Empirical Modeling of Subsidence due to Longwall Mining

As illustrated in the last section, mining activities can produce ground movement in the form of subsidence. Previous research has proposed different kinds of approach to characterize the ground subsidence due to mining using the empirical, theoretical, and numerical methods [6]. This section will introduce the empirical method using profile function and the hyperbolic tangent function.

2.1.1 Basic Characteristics in a Longwall Mining Subsidence Basin

2.1.1.1 Potential Maximum Subsidence

In the empirical method, the first step in constructing the empirical function is to determine the maximum subsidence. The potential maximum subsidence happens when the gob reaches the critical size and the ground surface has reached fully deformed stage. The magnitude of the potential maximum subsidence can be calculated as [7]

$$S_{max} = a \cdot M \quad (2.1)$$

where S_{max} is the maximum potential subsidence, a is the maximum subsidence factor, and M is the extraction thickness.

The maximum subsidence factor depends on the properties of the overburden strata and the mining method. For the case of longwall mining, the subsidence factor is in the range from 0.5 to

0.6 [8]. When considering the coal bed in southwestern Pennsylvania, the factor can be calculated as

$$a = 0.6760821 \times 0.9997678^h \quad (2.2)$$

where h is the height of overburden.

2.1.1.2 Actual Maximum Subsidence

The subsidence basin will reach the potential maximum subsidence only when the mining panel is supercritical or critical, and when the ratio of panel width to the mine bed depth is larger than or equal to one. However, for the case of subcritical panels, we need to know another parameter, actual maximum subsidence, in order to construct the empirical model. A general method of determining the maximum subsidence for the coal bed south west of Pittsburgh is proposed by Karmis et al. [9], which is applied for all conditions including subcritical, critical, and supercritical panels. The subsidence factor in this model is dependent on the percentage of hard rock and the ratio of panel width to overburden depth. The percentage of hard rock, H.R., is defined as the percentage of the cumulative thickness of limestone, sandstone, and other hard rock layers in the length of core pieces.

2.1.1.3 Angle of Draw

The angle of draw is the angle of a line connecting the edge of the panel to a point experiencing no subsidence with respect to a vertical line at the edge of the panel, as shown in Fig. 2.1. It is an important parameter in defining the area of the region which is influenced by mining activities.

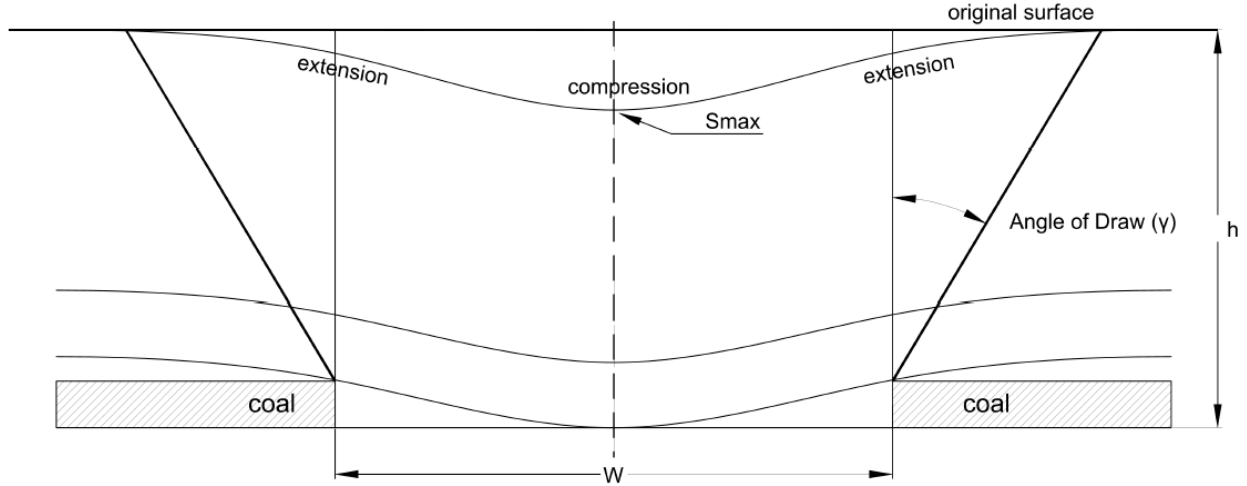


Figure 2.1. Cross section of a subsidence basin illustrating the angle of draw [10]

2.1.2 Profile Function

Profile function method is actually a regression fitting method based on the measured subsidence profile in a certain mine field. One of the most widely utilized profile functions in the Appalachian coalfield is the hyperbolic tangent function as [11]

$$S = 0.5S^* \left[1 - \tanh\left(\frac{cx}{B}\right) \right] \quad (2.3)$$

where S^* denotes the maximum subsidence, c the fitting constant, x is the distance from the observed point to the inflection point, and B the distance from the closest-to-edge point with maximum potential subsidence to the inflection point.

According to Eq. 2.3, the maximum subsidence is not located exactly at the panel center, hence, a correction is needed for the maximum subsidence expressed as

$$S'_{max} = \frac{S^*}{S_{center}} S^* \quad (2.4)$$

where S'_{max} represents the corrected maximum subsidence, S_{center} the magnitude of subsidence at the panel center before correction, and S^* the estimated maximum subsidence.

Distance B is dependent on the edge effect of the panels, which is defined as the horizontal distance from the inflection point to the vertical projection line of the edge of the panel. This distance should be calculated by subtracting the edge effect distance from the total distance between the closest-to-edge point with maximum potential subsidence and the vertical projection line from the edge of panel.

The steps for using SDPS to build up a subsidence basin are [12] :

- a. Input the basic properties of the mine panel, including the width, thickness, depth of panel, as well as the percentage of hard rock in the overburden;
- b. Calculate the estimated maximum subsidence and edge effect distance using the input panel properties;
- c. If the ratio of width to the depth of the panel is equal to or larger than 1.2, then use the fitting constant of 1.8, otherwise, use 1.4;
- d. If the ratio is less than 1.2, then calculate B distance as half width minus the edge effect distance, otherwise as 0.6 times B minus edge effect distance;
- e. Calculate the corrected location;
- f. Calculate the corrected maximum subsidence;
- g. Calculate the subsidence at each point using the profile function.

2.2 Numerical Method in Slope Stability Analysis

A large amount of research has been conducted to analyze slope stability using numerical methods in both two dimensions and three dimensions [13][14][15][16][17]. However, little

research has been conducted on the stability and deformation analyses of embankments located in highways when subjected to longwall mining [18].

2.2.1 Introduction to the Shear Strength Reduction Method

Strength reduction method (SRM) is widely utilized in slope stability analysis, having been initially developed by Zienkiewicz et al. [19]. Further improvements of the approach were contributed by Griffiths and Lane [20], Matsui and San [21], Zheng et al. [22], and Dawson et al. [23].

In conventional slope stability analysis using the limit equilibrium method (LEM), the critical slip surface needed to be determined. The factor of safety in the conventional method is defined as the ratio of shear strength to the inducing shear stress along the potential slip surface. When using the finite element method (FEM), there is no need to define the slip surface in advance and the stress-strain relationship of soil in the slope is considered. However, it is difficult to trace the failure slip surface in a slope based on a certain stress failure criterion, and it is difficult to derive the factor of safety equivalent to the LEM. This has been solved using SRM technique. Griffith and Lane [20] have suggested that the widespread use of SRM should be seriously taken into consideration as a powerful alternate method to the traditional limit equilibrium method.

Centrifuge tests have indicated that the plastic shear strain zone in unstable slopes coincides with the rupture surface [24]. In other words, the development of plastic shear strain reflects the potential failure and the stability of the slope depending on the shear strength of the soil in the slope. The SRM is applied to see in which part of the slope the plastic strain will develop.

On one hand, SRM associated with FEM has the following advantages. The final result of shear strain will show the critical failure surface in the slope under gravity and with strength

reduction. Besides, the interslice shear force assumption is not needed in this method. Furthermore, it is applicable to many complicated cases and can give the stresses and movements that the traditional LEM cannot provide. On the other hand, the method has the disadvantage of the long time needed to set up the computer model and perform the analysis. However, due to the development of commercial computer software, this is no longer a problem.

2.2.2 Implementation of the Shear Strength Reduction Method in ABAQUS

In SRM, in order to obtain the factor of safety (FS) equivalent to LEM, a strength reduction factor (SRF) is utilized. The factor is applied to reduce the original cohesion (c) and $\tan\phi$ until the slope fails. The original shear strength parameters are divided by this factor to obtain the reduced shear strength parameters c' and ϕ' as follows:

$$c' = \frac{c}{FS}, \tan \phi' = \frac{\tan \phi}{FS} \quad (2.5)$$

or using the equivalent equations using the SRF,

$$c' = \frac{c}{SRF}, \tan \phi' = \frac{\tan \phi}{SRF} \quad (2.6)$$

where c and ϕ are the laboratory measured shear strength parameters, and SRF the shear strength reduction factor.

The critical SRF occurs when the instability of the slope reaches the reduced strength parameters. The critical value of the ratio is approximately consistent with the factor of safety using Bishop's limit equilibrium method. The slipping surface can be traced from the development of the plastic shear strain.

When applying the SRM in FE analysis, the increasing SRFs are applied successively on the model to reduce the soil strength in the model until the solution runs out of convergence. In

ABAQUS, the procedure is implemented by creating a field value to represent SRF applied on the FE model. The field value is set at less than one before the SMR step in order to make the slope stable in the gravity and deformation steps. Then in the SMR step, the field value increases until the solution goes out of convergence. This largest SRF when failure occurs is equivalent to FS from LEM.

While applying SRM to practical analysis, according to the analytical test using the shear strength reduction method conducted by Tamotru Matrui and Ka-Ching San [24], the critical SRF can only be utilized as the factor of safety in analyzing an embankment slope, but not in analyzing an excavated slope. The well-defined failure shear strain zone in an embankment slope is not formed in the excavation slope due to the uncertainty of the initial shear strains before excavation and the shear strain increment is not normally distributed.

2.3 Previous Research on the Influence of Longwall Mining Subsidence on Highways in South-West Pennsylvania

Since the 1980s, two interstates, I-79 and I-70, have been impacted by the longwall mining activities in southwestern of Pennsylvania. In total 25 panels that have been undermined in Washington and Greene counties, which have influences on the interstates as shown in Fig. 2.2.

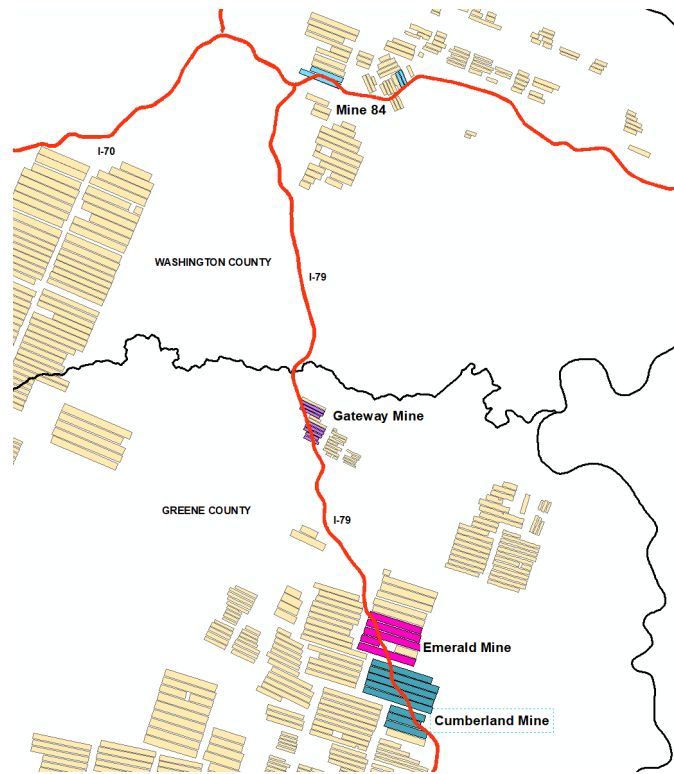


Figure 2.2. Longwall panels which have influenced the interstates in south western Pennsylvania [25]

Researchers have been studying the influence of Gateway Mine, Emerald Mine, and Cumberland Mine on I-79 as well as Mine 84 on I-70 [26]. Gateway Mine is the first mine built under an interstate highway, as being one of the deepest [27]. Previous research showed that it has a minor influence on the highway.

2.3.1 Field Monitoring

Early studies with respect to the influence of longwall mining on the highway provide us with some methodologies for observing the deformations, analyzing the data and taking actions to ensure safety.

When analyzing the effect of longwall mining on I-70 in 2001, O'Connor [28] detected movement using the data from tiltmeters installed along highway, which activate an alarm when reaching a tilt of 0.002ft/ft. However, he found that the predicted subsidence was different from the field data. In addition, he observed longitudinal cracks between lanes and some transverse cracks due to mining. PennDOT temporarily closed the lanes where damage occurred and milled the bumps in order to keep the road in a safe condition.

In a similar project working on the influence of the Cumberland Mine on I-79, Gutiérrez, J.J. et al. [29] collected survey data of subsidence along the highway alignments. They normalized the data through dividing the subsidence data from five panels by the maximum subsidence. The data collection is conducted during the mining procedure; in other words, the dynamic subsidence basin is obtained from the collected data. A projection is developed on the subsidence data with respect to the longitudinal axis. Fig. 2.3. indicates dynamic subsidence profiles projected on the z plane based on the coordinate system shown in Fig. 2.4.

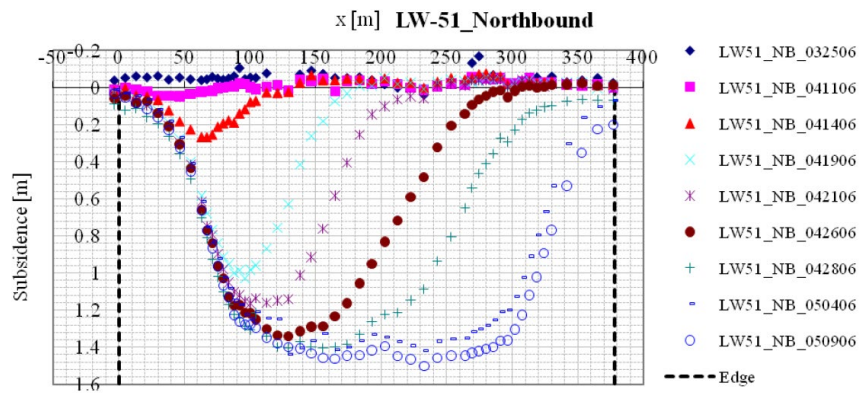


Figure 2.3. Dynamic subsidence projected to z-plane [29]

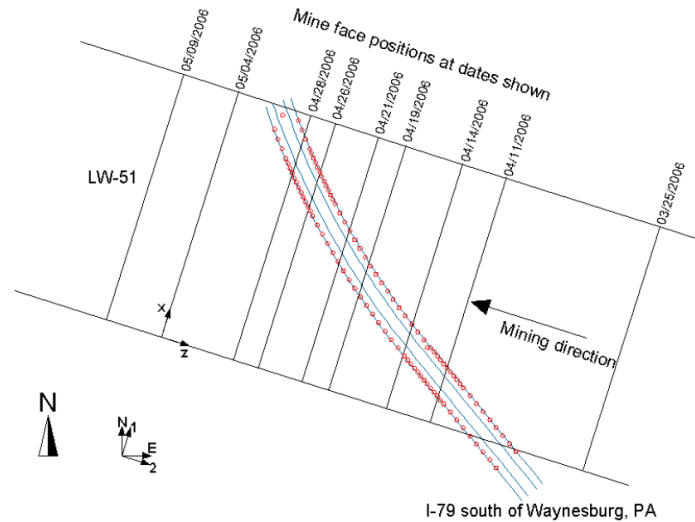


Figure 2.4. Coordinate system of the panel [29]

2.3.2 Numerical Modeling

When doing the data modeling of the subsidence basin of the Cumberland Mine, Gutiérrez, J.J. et al. [30] found that the Richard's model [31] performs well in obtaining a 3D subsidence basin, having the least amount of error compared to the data. In addition, they utilized this model to build up basins for longwall mining panels.

They also simulated the three-dimensional subsidence using FEM with the commercial software LS-DYNA. Layers model was utilized to simulate the overburden. They used a tiebreak definition for the contact and the friction angle between the layers. Calibration was carried out using the criterion based on the trough shape, maximum subsidence, and post-mining vertical stress distribution, all of which are important parameters in depicting a 3D subsidence basin. It turns out that the FEM model is suitable in some cases. Horizontal stresses are found to be extremely high in southwestern Pennsylvania, which will play an important role in simulating the subsidence.

2.4 Previous Research on the Influence of Longwall Mining on the Slope Stability Problem

Longwall mining subsidence results in the variation of the slope and curvature of the ground surface which will impact the slope stability of the embankments which are high. In addition, the movement of the ground surface will deform the soil of the embankment and will contribute to the consolidation of the soil of the embankment under gravity. In the 37th International Conference on Ground Control in Mining (ICGCM), Nicole E. Evaneck [18] conducted a review of the last 36 years of reports at the ICGCM regarding mining-induced subsidence. This important paper indicated that little research had been done on the influence of longwall mining on the slope stability of highway embankments. The only research activity that exists is related to the study of slope stability in open pit mining which is quite different from longwall mining. The current study will explore this under-researched problem. Two practical cases will be examined in this section. One study focuses on the slope stability of a highwall impacted by longwall mining which was presented at the conference mentioned above. Another case explores the impact of longwall mining on the construction procedure of a highway embankment. Both cases refer to sites in Australia.

2.4.1 Field Monitoring

An undermined highwall was inspected in Australia [32]. The field work was carried out by a coal company which found that traditional survey stations or latest laser technologies are limited when dealing with problems in areas where the topography varies dramatically.

In the initial observations, a tiltmeter is utilized to observe the movement of the highwall in front of the longwall mining face. It showed that the resulting shear movement is toward the

center of the void produced by the longwall mining. The tension force is generated as the overburden falls into the gob, causing the backward movement of the soil. In other words, the longwall mining subsidence actually pulls the highwall back and makes the highwall more stable.

A more advanced monitoring was then conducted using GroundProbe SRM-XT radar as the longwall working face neared the final locations. This instrument is capable of scanning a distance of 100-ft to 11500-ft from the place where the radar is set up. In addition, with the aid of the visual inspection functions, a two by two pixel is utilized with the integrated visual imaging system. These techniques enabled real-time graphical display of total displacement and rate of wall movement. The scan was carried out every 13-min. Finally, the total movement generated by the longwall and rate of movement are observed using these instruments.

Another monitoring activity was carried out under the supervision of Silesian Technical University on a motorway embankment under construction after mining [33]. They monitored the subsidence of the ground surface resulting from underground mining activities and then the embankment subsidence due to the weight of the embankment.

The researchers monitored the motorway on both sides at a distance of 160-ft m to 260-ft from the center line to measure the subsidence of the ground surface due to mining activities. In addition, they inspected the subsidence of the embankment using specially designed bench marks inserted on the bottom of the central section of the embankment, shown in Fig. 2.5.

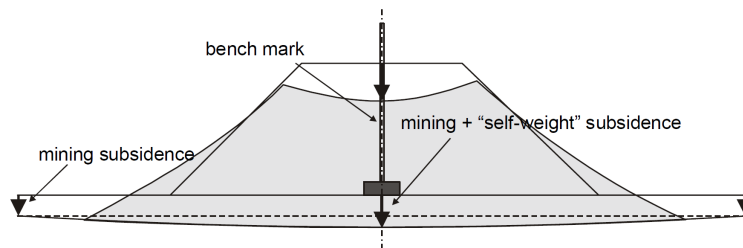


Figure 2.5. Location of the bench mark [33]

The bench mark is composed of a square reinforced concrete slab and a steel rod fixed vertically within it. The slab is located at the bottom of the embankment in the center. The rod consists of several sections which are 1m in length. New sections are connected to the top of the rod as the height of embankment grows during construction. The height of the embankment can be easily obtained using this rod. In addition, the subsidence due to the embankment's weight can also be reflected with this instrument.

2.4.2 Numerical Modeling

When dealing with slope instability analysis due to longwall mining, numerical methods such as Finite Element Method are utilized to understand the mechanism of the deformation and failure of the embankment as well as to help predict the failure in a similar condition.

FEM-DYNA software was utilized by Gutiérrez, et al. [29] to analyze the influence of longwall mining on three-dimensional embankments. The mining direction is perpendicular to the highway direction, as shown in Fig. 2.6. The author compared the horizontal deformation and subsidence with embankments and without embankments. The horizontal deformation is found to be larger in the case of embankments than that in the overburden.

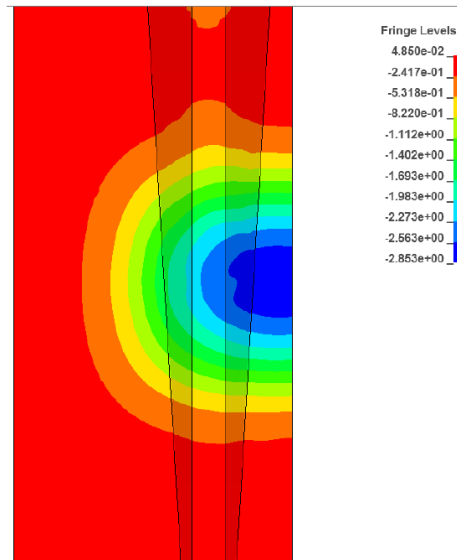


Figure 2.6. Over view of the subsidence with an embankment on it [29]

Two-dimensional FEM embankments were constructed by K. Sternik [33] to consider the influence of longwall mining on the construction of the embankment. The author analyzed the subsidence on the embankment surface by considering its weight and influence of mining separately and compared both. The process of construction and soil consolidation was simulated with a certain increment in the height of layers per day. Elasto-plastic material properties were utilized to simulate the behavior of the embankment fill [33] [34]. The results compared well. Stilger-Szydło and Tutaj [35] illustrated the slope instability under subsidence using an FEM model. In this model constructed using ABAQUS, a highway embankment is subject to subsidence. Loosening of the embankment soil occurs in the tensile strain zone. Large areas of high strain appear, which may cause instability in the embankment. Different failure criteria were considered such as those assumed by the Mohr-Coulomb Model, the Drucker-Prager Model, the Cam-Clay Model, and the Cap Model.

A two-dimensional FEM was developed by Clarkson [36] in 2016 to investigate the influence of longwall mining on the movement of a high wall. The vectors of ground movement generated by the model show that the high wall moves away from the longwall, which is consistent with the field monitoring results.

Generally, little research has been conducted to analyze the influence of longwall mining subsidence on highway embankments. Moreover, none of the previously conducted research explored the slope stability analysis of three-dimensional highway embankments due to longwall mining. This study will investigate the influence of longwall mining subsidence on the slope stability of highway embankments. It will also explore the influence of different parameters on the stability of the embankments including the angle of the direction of the embankment with respect to the mining direction of the embankment in the panel, which will in turn influence the performance of the embankment. Finally, the effect of the height of overburden on the subsidence will also be investigated.

3.0 Laboratory and Field Investigations of Embankment #1 and Highway I-70

3.1 Analysis of Soil Tests

Boreholes were made at two cross sections (720+00 and 720+50) of Embankment #1 as indicated in Fig. 3.1. An analysis of the materials from the boreholes provided the two-dimensional soil profiles of the interior layers of Embankment #1 as shown in Fig. 3.2. The body of the embankment was found to be composed of three type of soils: fill, alluvium, and a mixture of soil and rock fragments at the bottom of the embankment. The fill, which constitutes the major part of the embankment, is made of a sandy-silt soil. It is worth noting that the soil type at the bottom of the embankment and above the soil with rock fragments is an alluvium type of soil. This alluvium could have been the original soil of the ground surface on top of which Embankment #1 was constructed.

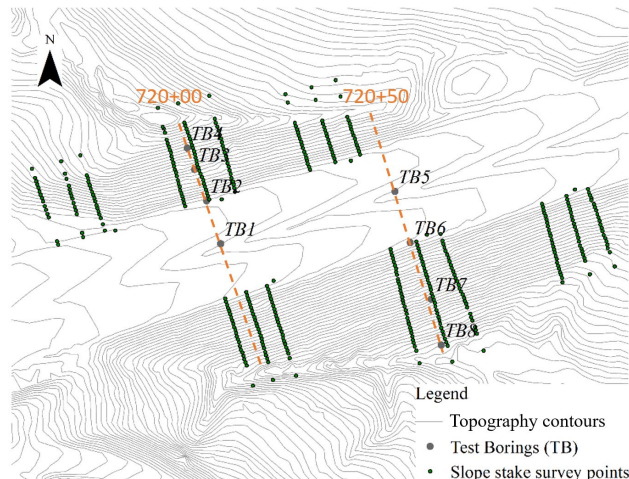


Figure 3.1. Locations of test borings at two cross sections 720+00 and 720+50 of Embankment #1

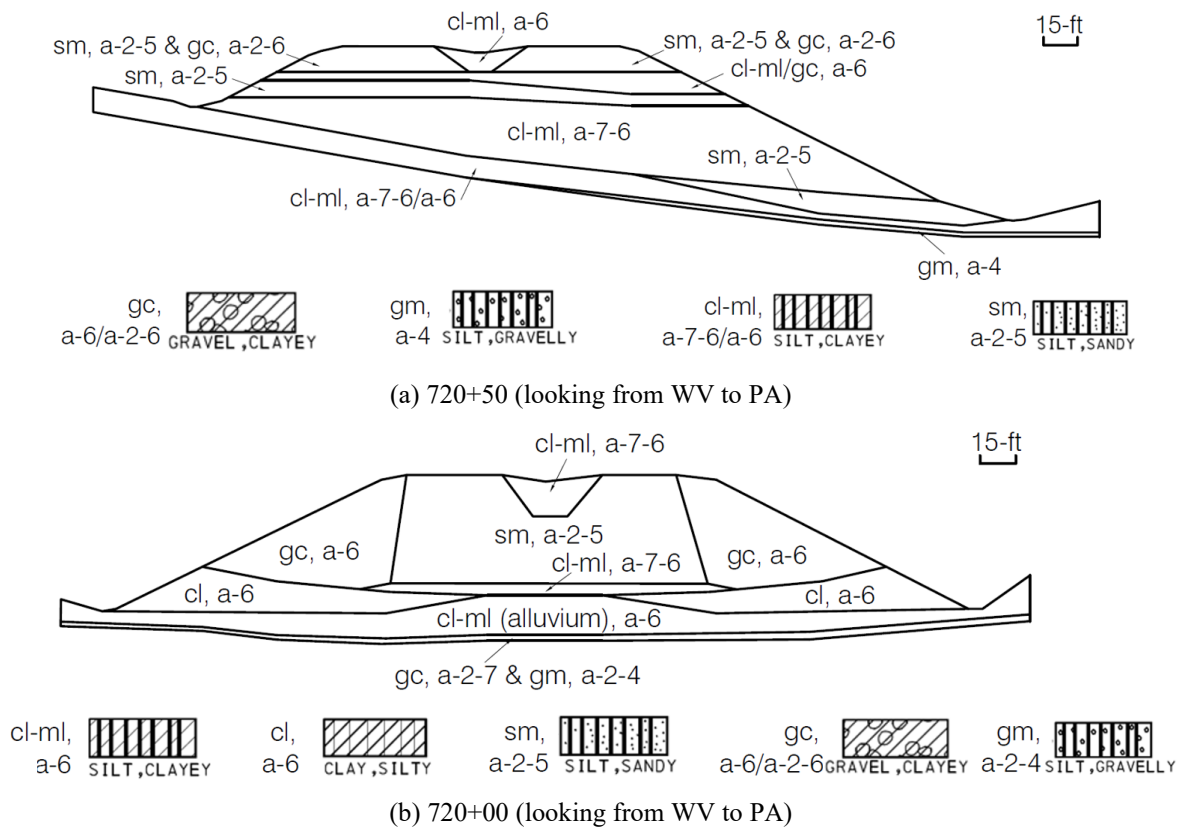


Figure 3.2. Geometry of layered Embankment #1 in two dimensions at cross sections (a) 720+50 and (b)

720+00

Consolidated undrained (CU) triaxial tests with pore pressure measurements were conducted on soil samples obtained at different locations of the embankment. The types of soils in these boreholes are shown in Figures 3.3 (a) and (b). The results of CU triaxial tests are summarized in Table 3.1. The stress-strain relationships obtained from the triaxial tests are also shown in Fig. 3.4. These relationships indicate that the materials forming part of Embankment #1 behave like a slightly strain-hardening soil. That is, the soil becomes somewhat stronger as it deforms. Soil data in the form of classification, unit weights, water contents, and shear strength parameter values are provided in Table 1. This data covers the four different types of soils that were used in the construction of Embankment #1. The material properties of the first two samples

Table 3.1. Summary of laboratory Shelby tube CU triaxial test results

	depth(ft)	USCS	AASHTO	γ (pcf)	ω (%)	ϕ (°)	c(psf)
TB1	6-11	CL	a-6 Fill	115.1	12.8	33.5	28.8
TB1	21-23.6	CL	a-2-5 Fill	98.5	8.6	25.6	633.6
TB5	24.2-26	CL	a-7-6 Fill	118.9	12.2	30.2	72
TB8	6.5-8.5	MH	a-7-5 Alluvium	89.2	37.7	23.2	316.8

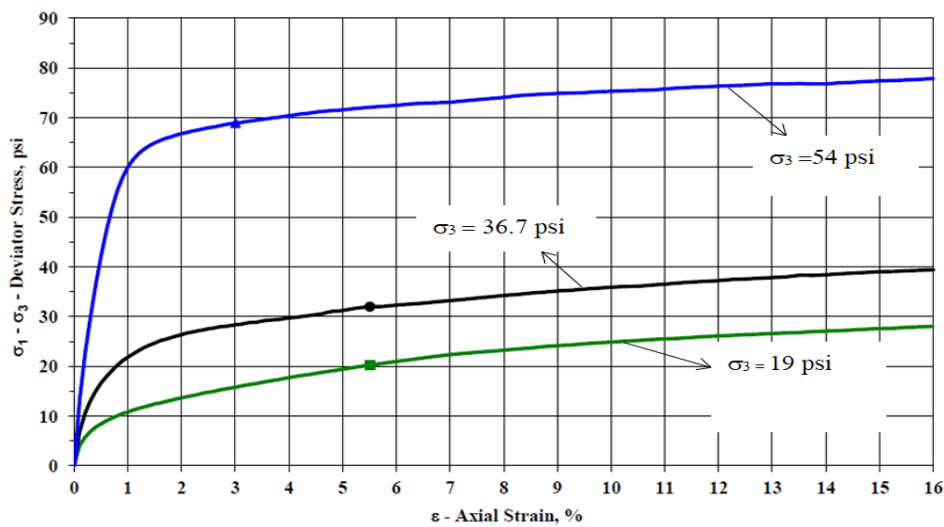


Figure 3.4. Stress strain relationship of soil sample in Embankment #1 Fill from lab results

The average Young's modulus of elasticity for the soils forming part of Embankment #1 is calculated using the results shown in Fig. 3.4 and Table 3.1 and the relationship proposed by Briaud [37] as follows,

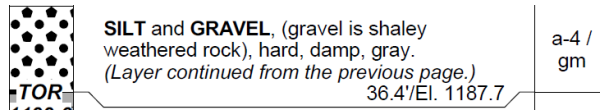
$$E = \frac{\sigma_1 - 2\mu\sigma_3}{\epsilon_f} \quad (3.1)$$

The average bulk unit weight of the soil forming part of Embankment #1 is calculated using the average water content of 12.5% of the soils from boreholes TB-1 and TB-8 (Table 3.1). The average bulk unit weight was obtained using the relationship proposed by Wu [38] as follows,

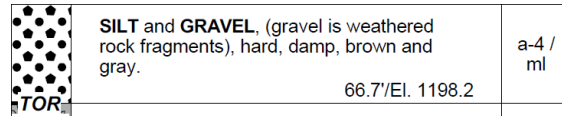
$$\overline{\gamma}_{bulk} = \overline{\gamma}_{dry}(1 + \bar{w}) \quad (3.2)$$

There are two layers of soil containing high percentages of gravels in the embankment according to the boring logs TB-1, TB-4, TB-6 and TB-7 (Figures 3.5 and 3.6). One is located on the bottom of the embankment, and the other is located on the lateral region of the embankment at cross section 720+00.

The gravel on the bottom of the embankment is indicated in the boring logs of cross section 720+00 and 720+50 shown in Figs. 3.5 and 3.6, respectively. Gravelly-silt and gravelly-sand are located in the bottom of the embankment. Another part of clayey gravel is located at the lateral parts of embankment #1 at cross section 720+00 (see Fig. 3.7). The gravel here refers to weathered limestone fragments. It should be noted that no triaxial tests were conducted on the soil containing high percentages of rock fragments at cross sections 720+00 and 720+50. The tests were conducted only on the soil matrix.

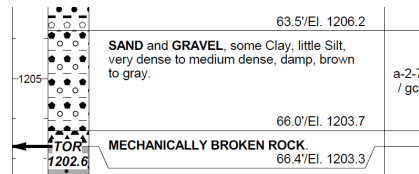


(a) TB-6

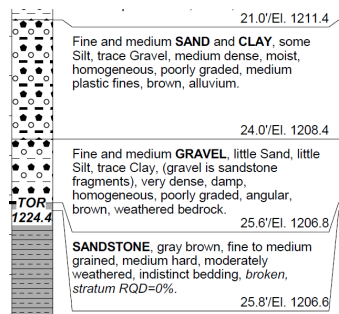


(b) TB-7

Figure 3.5. Configurations and locations of the gravelly silt at (a) TB-6, on the crest of the embankment and (b) TB-7, in the middle of the embankment at cross section 720+50



(a) TB-1



(b) TB-4

Figure 3.6. Configurations and locations of the gravelly sand layers at (a) TB-, in the middle of the embankment and (b) TB-4, near the toe of the embankment at cross section 720+00

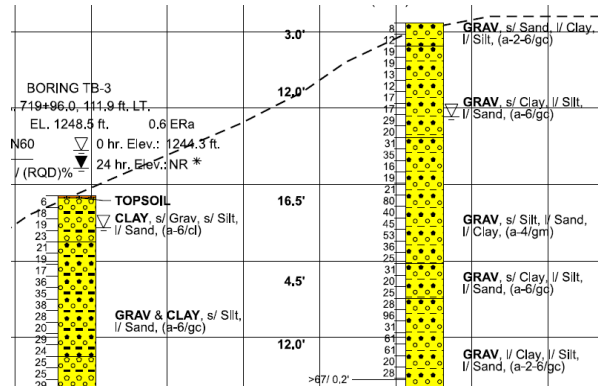


Figure 3.7. Clayey/Silty gravel in the lateral region of embankment at cross section 720+00

However, Iannacchione and Vallejo [39] have determined that the shear strength of soil-gravel mixtures is enhanced by the concentration of the rock fragments in the soil matrix. That is, the higher the concentration of the rock fragments in the mixtures, the higher are their shear strengths. These higher shear strengths are translated into higher friction angles and higher cohesion intercept values for the soil-rock mixtures. From an analysis of the types of soils obtained from the boring logs, it was determined that the concentration by weight of the rock fragments in the soil-rock mixtures obtained from boreholes TB-1, TB-4, TB-5, TB-6, TB-7 and TB-8 varied between 5% and 44% , with an equivalent concentration by volume between 2 and 23 % (Table 3.2). Thus, according to Iannacchione and Vallejo [35], these high concentration values of rock fragments will result in higher friction angles and higher cohesion intercept values for the soil-gravel mixtures.

Table 3.2. Percentage of rock fragments in samples

Borehole	Depth, ft	USCS	AASHTO	C _w = % of Rock Fragments by Weight	C = % Rock Fragments by Volume*
TB-1	21.0-23.6	CL	a-6	7	2.8
TB-4	3.0-12.0	GC	a-7-6	44	23
TB-5	24.2-26.0	CL	a-7-6	33	15.7
TB-6	55.5-64.5	CL	a-7-6	25	11.2
TB-7	22.5-31.5	GC	a-2-6	41	20.8
TB-8	6.5-8.5	MH	a-7-5	5	2

*C = [C_w]/[G_s - (G_s - 1)C_w], G_s = specific gravity = 2.65

The resulting shear strength parameters based on the laboratory tests are summarized in Table 3.3 and plotted in Fig. 3.8. In the 3D model in the following chapters, the material properties are further adjusted using sensitivity tests.

The resulting shear strength parameter values measured in the soil matrix forming part of Embankment #1 are shown in Table 3.3. The values presented in Table 3.3 are the original values without the effect of the rock fragments. For the stability analysis, the values reported in Table 3.3 will be adjusted later to take into consideration the effect of the dispersed gravels on the shear strength of the soils forming the matrix of the soil-rock mixtures.

Table 3.3. Original soil properties of different layers of Embankment #1

Bore hole	Depth, ft	Soil type	Bulk Density, pcf	cohesion, psf	Friction angle, °
1	6.0-11.0	Clay	130	29.0	33.5
7	3.0-18.0	Clayey Gravel	127	446	-
1	21.0-23.6	Clay	107	634	-
2	15.0-31.5	Clayey Gravel	128	418	30.0
5	24.2-26.0	Clay	133	72.0	30.0
3	21.0-33.0	Clay	122	317	-
3	33.0-43.5	Clay	123	792	-
6	30.0-45.0	Clayey Gravel	136	734	-

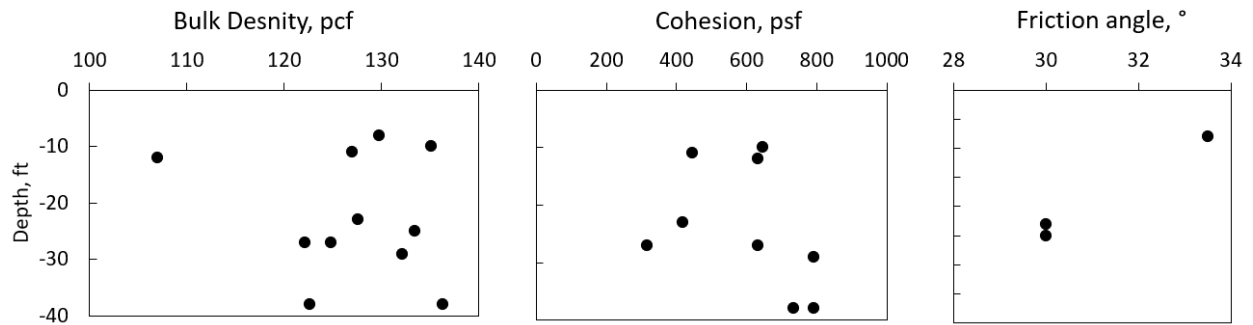


Figure 3.8. Original soil properties versus depth in Embankment #1

3.2 Analysis of Field Monitoring and Surveys

3.2.1 Inclinometers

Inclinometers were placed in six test borings in order to measure the lateral deformations of the embankments. The author is focusing on four of them which are on the crests and toes of Embankment #1 (Fig. 3.9). The displacements along the B-axis represent deformations parallel to the highway direction. The deformations along the A-axis are normal to the highway direction and represent deformations away from the slope face of the embankment (Fig. 3.9), which is more important to the slope stability in this study.

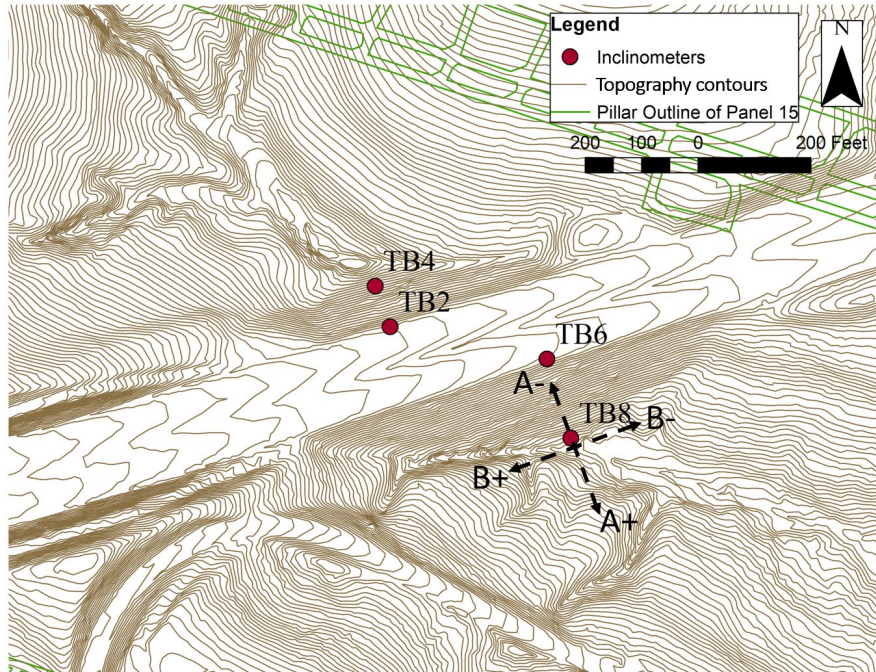


Fig. 3.9. An overview horizontal displacements along two directions A and B measured by inclinometers in four test borings in Embankment #1

Readings of inclinometers were recorded every 2 ft from the bottom to the top of each test boring. When analyzing the data, the cumulative movements at certain depth were calculated by adding up the readings at each interval from the bottom to this depth. The cumulative displacements in two directions measured by the inclinometer at TB-8 are shown in Figs. 3.10 and 3.11 as an example.

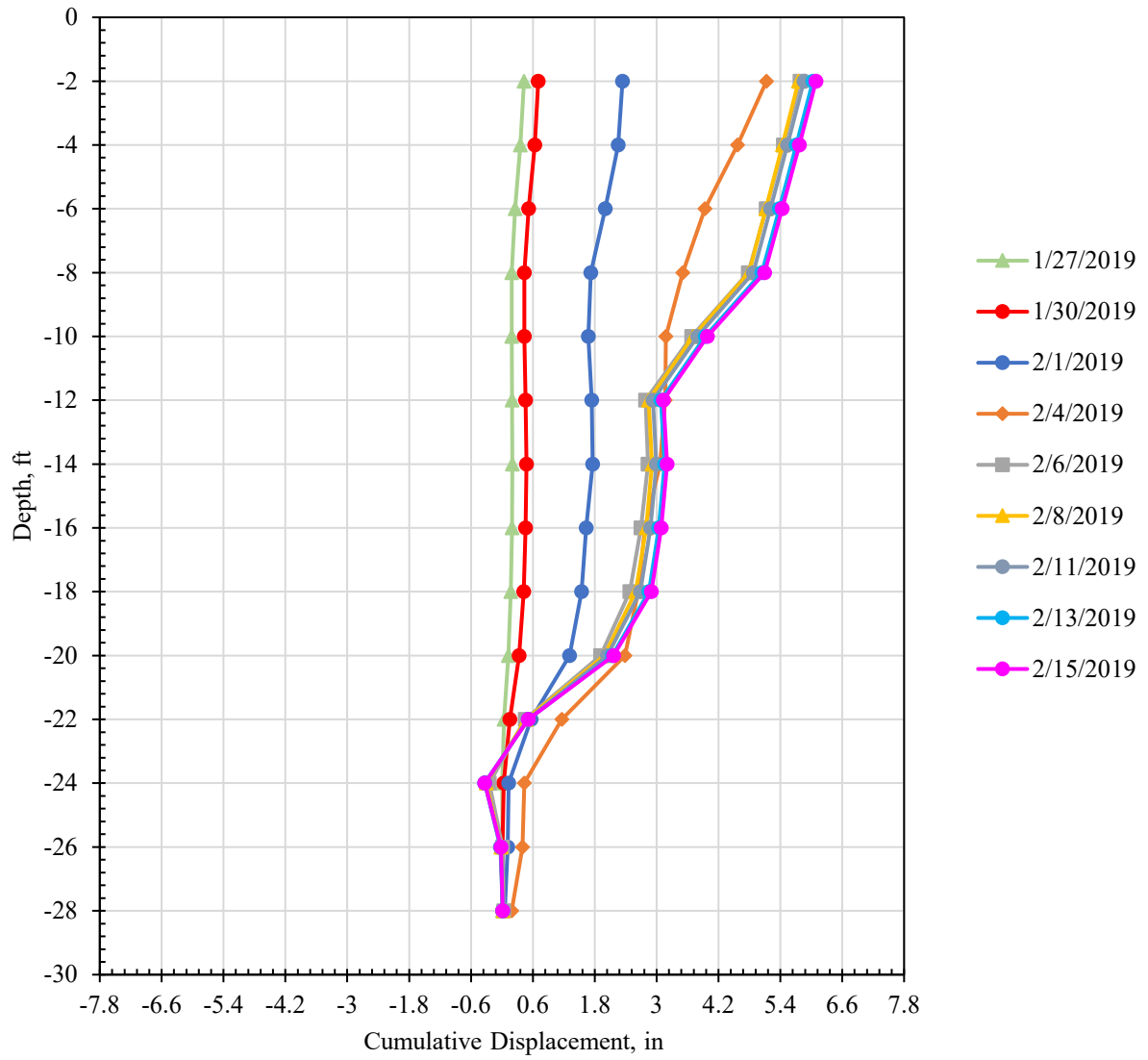


Fig. 3.10. Cumulative displacement along A axis measured by inclinometer at TB-8

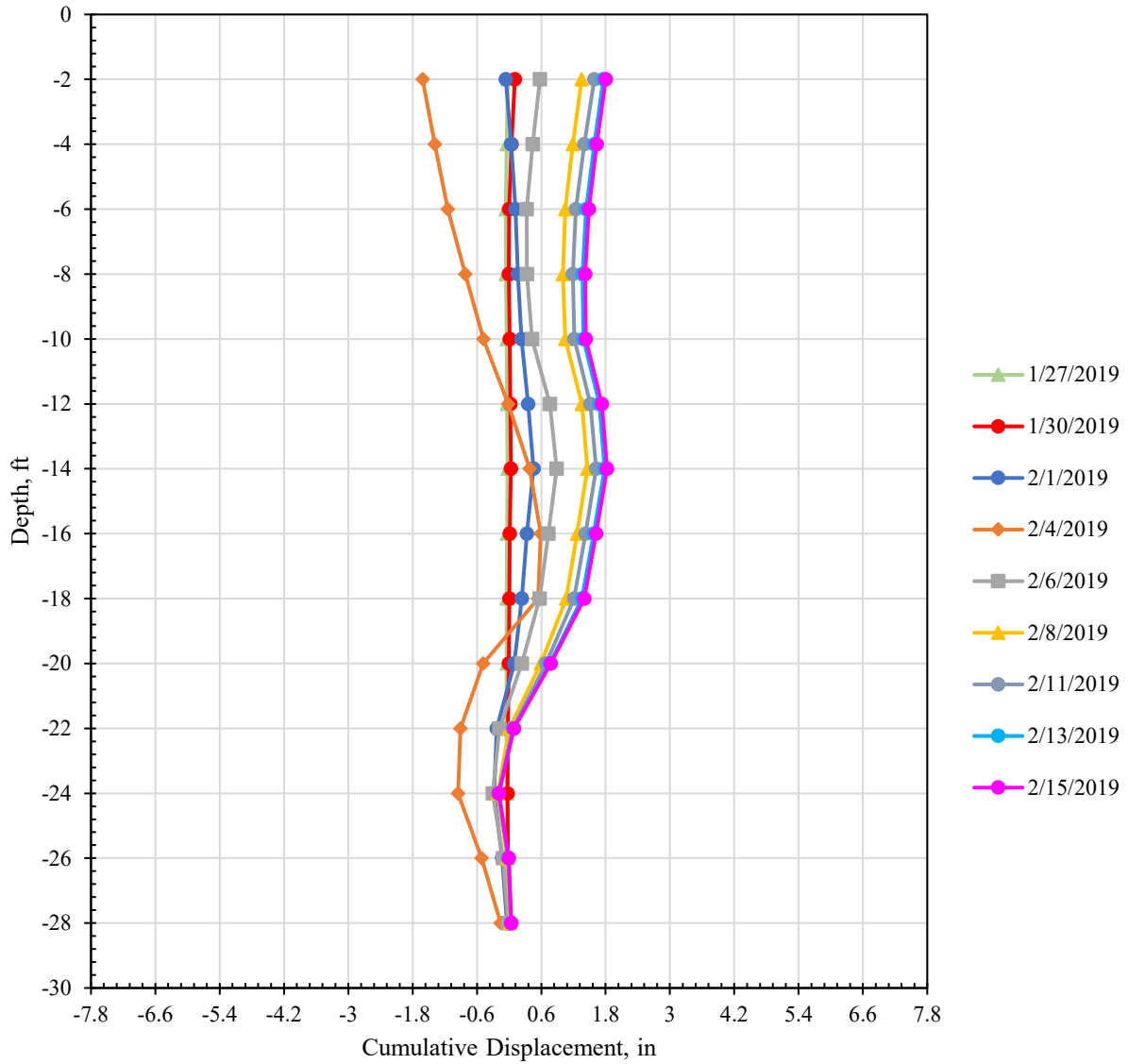


Fig. 3.11. Cumulative displacement along B axis measured by inclinometer at TB-8

An analysis of Figs. 3.10 - 3.12 indicates that more deformation took place at the surface than at the bottom of the embankment at each of these four borings. The lateral spreading on the surface is around three times to that at the bottom deformation on the north-facing slope. On the south-facing slope, the lateral spreading on the surface is nine times to that at the bottom of the crest. For the area of toe, the spreading on the surface is four times that of the spreading at the bottom.

The resulting lateral spreading on the surface at these four test borings is summarized in a 3D model of Embankment #1 shown in Fig. 3.13. These movements are calculated through the cumulative displacements measured by inclinometers along A axis after the embankment settled in the field. These horizontal deformations from field measurements will be compared to the numerically simulated deformations in the following chapters. It is shown that the embankment moved outward, and lateral spreading occurred as a result of the longwall mining induced subsidence. The maximum magnitude of the outward movement occurred at the toe area. It indicates that the toe area experienced larger deformations than those measured on the crest of the embankment. Also, the lateral spreading on the south-facing slope is larger than that on the north-facing slope, which means that the south-facing slope experienced more sliding deformation due to subsidence.

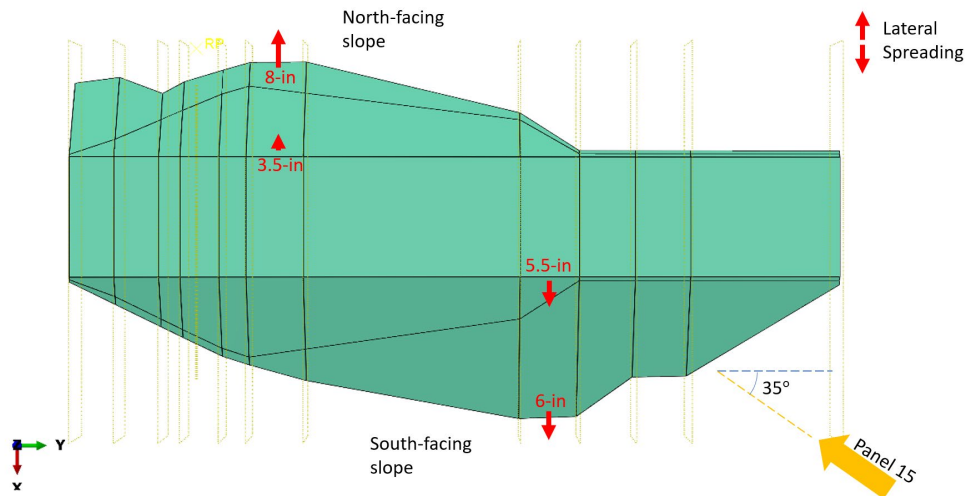


Figure 3.12. Field measurement of inclinometers(cumulative) after subsidence denoted on a 3D model of Embankment #1

3.2.2 Slope Stake Surveys

The SPK Engineering company conducted the slope stake surveys in the field, placing over five hundred stakes in the study area to measure the deformation on the slope surfaces of Embankments #1 and #2. The stakes are aligned from the toe to the crest of the slopes. An overview of these stakes is shown in Fig. 3.13. The group-sets, named 2N, 3N, and 4N, are located on the north slope of Embankment #1. The group-sets, named 2S, 3S and 4S, are located on the south slope of Embankment #1. The group-set, named 6S is located on the south slope of Embankment #1.



Figure 3.13. Locations of slope stakes categorized by groups

3.2.2.1 Analysis of the Vertical Subsidence on the North-Facing Slope of Embankment #1

The slope stakes on the north-face slope of Embankment #1 present similar behavior during the longwall mining. One of these alignments starting from the crest to the toe of a slope is selected

as an example and is shown in Fig. 3.14. It is located at the north-face slope of one of the two critical cross sections of the embankment.

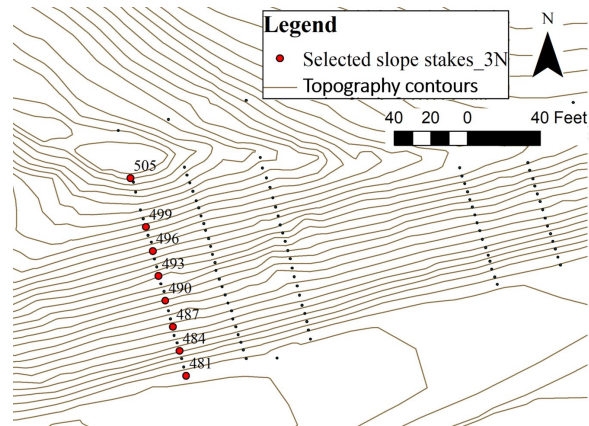


Figure 3.14. Numbers of selected slope stake survey points located on the north slope of Embankment #1

The vertical displacements measured by these points on the north-facing slope of Embankment #1 are plotted against dates shown in Fig. 3.15. It is indicated that the north-facing slope showed an expansion upward of 0.2-ft on February 4th, 2019 and started to move downward after that time. It reached the maximum subsidence on February 18th, 2019. On February 25th, 2019 it moved downward 0.07-ft and totally stopped with no further movement since then.

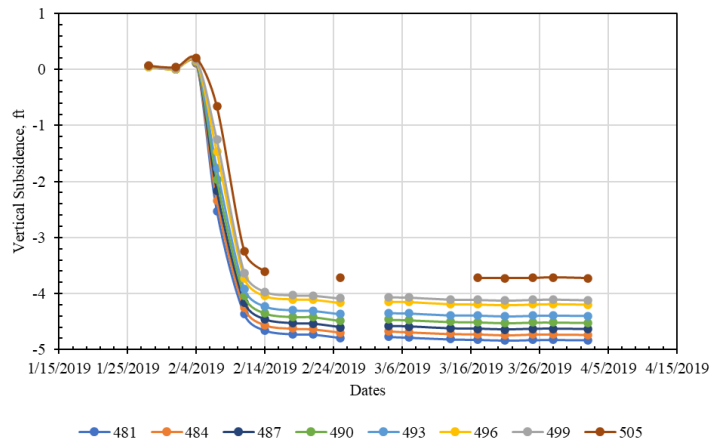


Figure 3.15. Vertical subsidence measured by selected slope stake survey points on the north-facing slope of Embankment #1

In addition, the maximum subsidence on the crest of the north-facing slope is 4.73 ft, which is larger than the toe shown in Fig. 3.16. The thickness of the embankment at the crest is larger than that at the toe. Thus, the crest of the embankment will experience more soil consolidation as a result of the longwall mining.

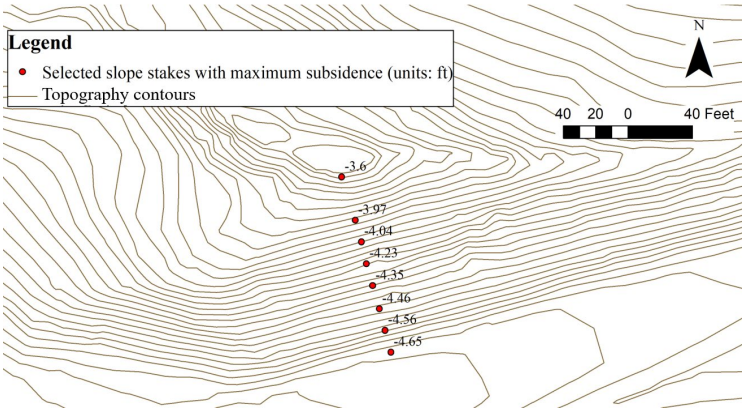


Figure 3.16. Maximum subsidence measured by the slope stake survey points on the north-facing slope of Embankment #1

3.2.2.2 Analysis of Vertical Subsidence on the South-Facing Slope of Embankment #1

The locations of the selected slope stakes on the south-face slope of Embankment #1 are shown in Fig. 3.17. They are aligned from the crest to the toe of the south-facing slope at the critical cross section of the embankment.

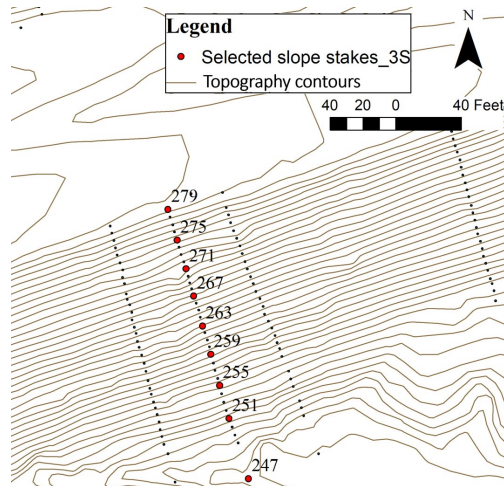


Fig. 3.17. Locations and numbers of slope stakes on the south-facing slope of Embankment #1

The vertical displacements measured by these stakes on the south-facing slope of Embankment #1 are shown in Fig. 3.18, indicating how the subsidence basin developed with time. The south-facing slope started to move downward on February 1st, 2019. It reached the maximum subsidence on February 18th, 2019. It then totally stopped moving with a maximum vertical subsidence of 5.08-ft.

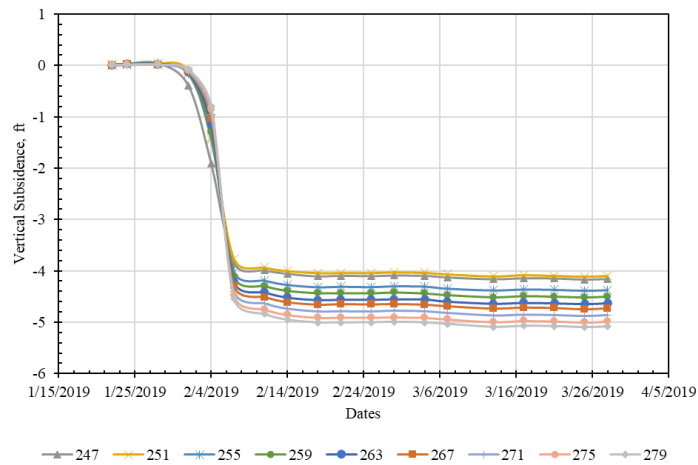


Fig. 3.18. Vertical displacement measured by selected slope stakes on the south-facing slope of Embankment #1

The maximum subsidence measured at each survey point after the mining working face passed is shown in Fig. 3.19. A similar phenomenon to that at the north-facing slope was observed. The points on the crest where the embankment is thicker showed a larger maximum subsidence than those on the toe. Furthermore, the maximum subsidence on the crest is larger than that on the north-facing slope as a result of the fact that the embankment's thickness on the south facing slope at 720+50 is greater than that on the north-facing slope at cross section 720+00.

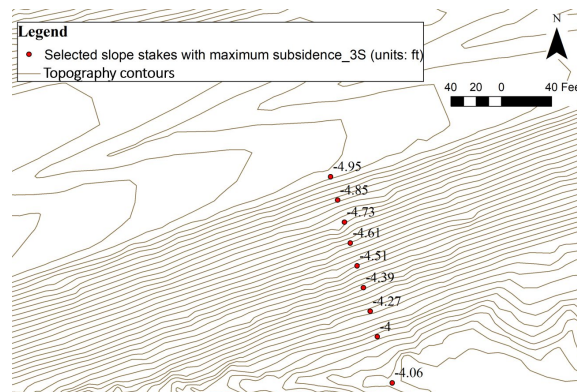


Figure 3.19. Maximum subsidence measured by selected slope stakes on the south-facing slope of Embankment #1 at cross section 720+50

3.2.2.3 Analysis of Vertical Subsidence on the South-Facing Slope of Embankment #2

The Embankment #2 is located on the edge of the panel on the gate road. Only the south-facing slope is located inside the gate road. The selected slope stakes are located at the toe of the south-facing slope that are close to the area of the coal seam shown in Fig. 3.20.

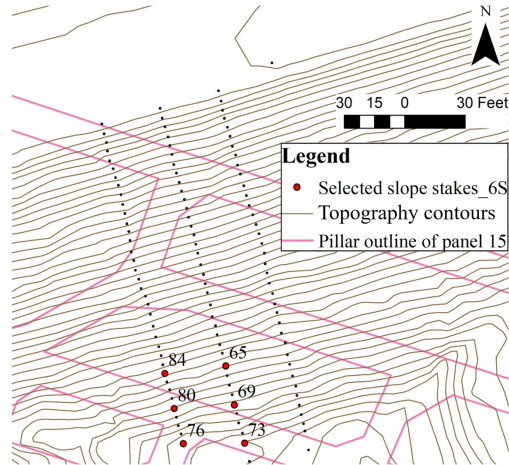


Figure 3.20. Locations and numbers of slope stake survey points on the south slope of Embankment #2

The vertical subsidence measured by these slope stakes is plotted in Fig. 3.21. It is shown that the slope began to expand upward on January 28th, 2019 and reached a level of 0.16-ft four days later. The slope began to move downward on February 4th, 2019 and settled with a subsidence of 0.03-ft. In conclusion, the slope seems to move as a whole and few deformations occur due to longwall mining subsidence. It established that the ground above the gate road moves upward a little bit when the working face is underneath it, and will settle to the original position, and experience almost no subsidence after mining.

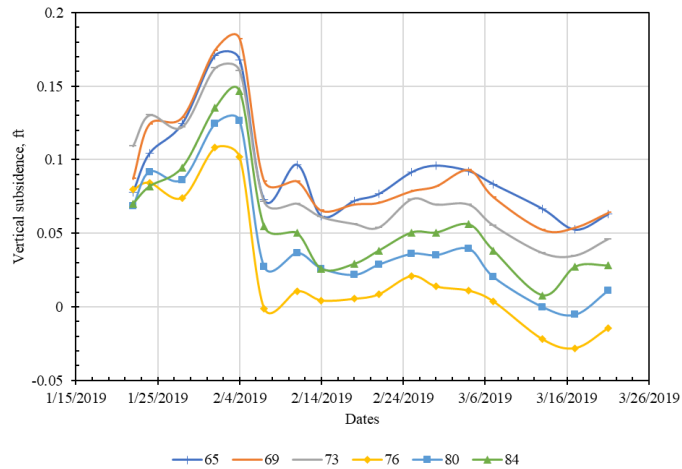


Figure 3.21. Subsidence measured by the slopes stakes on the south-facing slope of Embankment #2

The maximum subsidence at these survey points is summarized in Fig. 3.22. In addition to the point at the toe where the subsidence is rounded to zero, other points represent a small amount of upward expansion after subsidence. The point close to the boundary of the panel shows no subsidence. The ground away from the boundary will move upward at the edge of the panel in the process of subsidence.

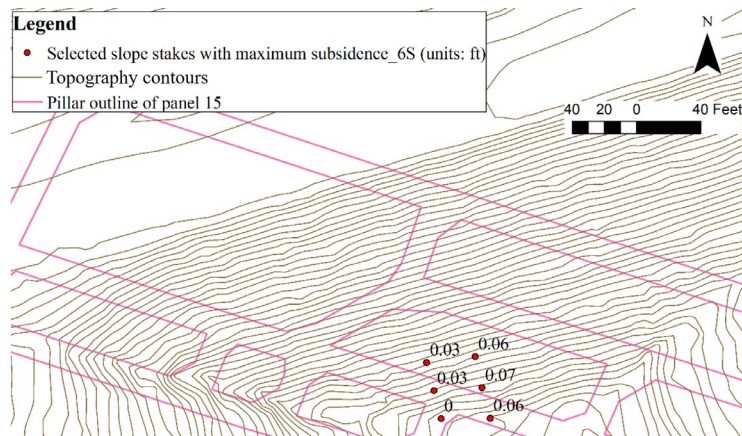


Figure 3.22. Maximum subsidence at the selected slope stake survey points on the south-facing slope of Embankment #2

3.2.2.4 Subsidence Contour Generated by ArcGIS Using the Slope Stake Measurements

Fig. 3.23 shows an overview of the subsidence contours in Embankment #1 when the working face of mining went through the study area reaching a position beyond the location of the embankment. The contour indicates that the maximum subsidence of 5 ft occurred in the middle of east-bound lane of Embankment #1 that is in the center of the panel whereas nearly no subsidence occurred in Embankment #2 that is on the gate road. In addition, the vertical subsidence is related to the thickness of the embankment fill. The regions with a deeper thickness of fill tend to exhibit larger subsidence values. The vertical subsidence contour will be compared to that in the three-dimensional Finite Element embankment to calibrate the model.

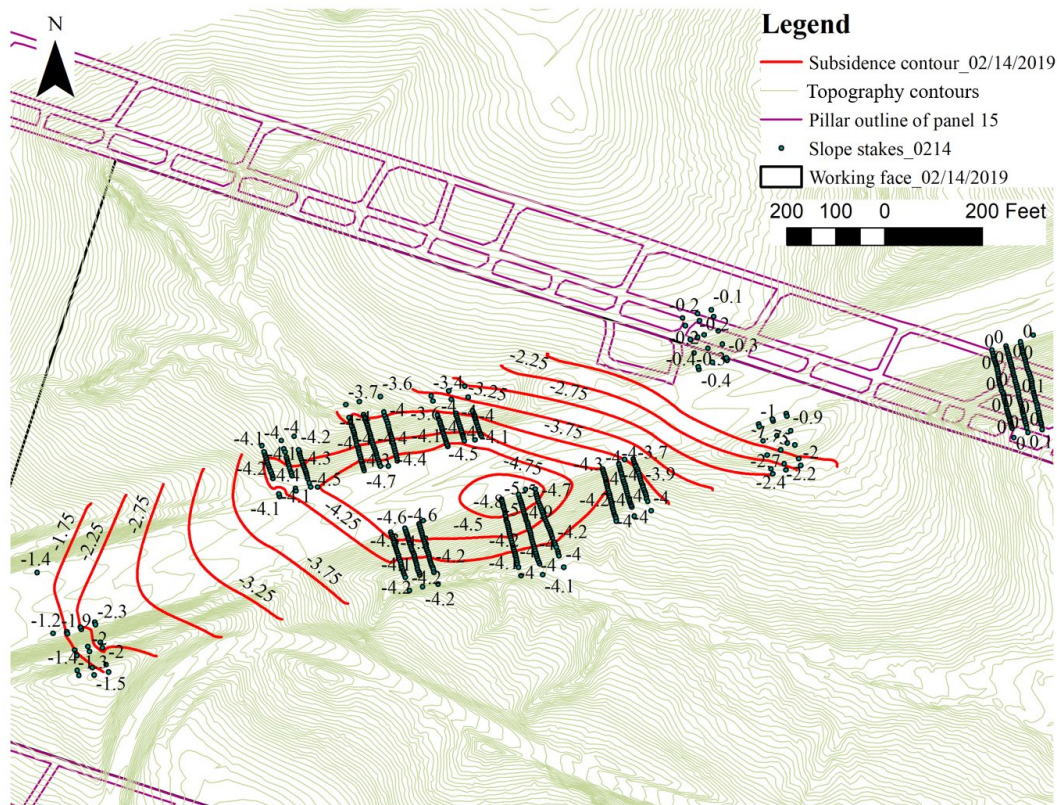


Fig. 3.23. Vertical subsidence contour on the highway embankments with face position of mining on 2/14/2019 generated by ArcGIS using the slope stake survey data

3.2.3 Piezometers

In total there are three piezometers monitoring the variation in water levels in the embankments. An overview of locations of these three piezometers is shown in Fig. 3.24. They are located in three test borings, TB-3 on the north-facing slope of Embankment #1, TB-7 on the south-facing slope of Embankment #2, and TB-12 on the south-facing slope of Embankment #2. The piezometer data shown in Fig. 3.25 were recorded by PennDOT and Earth Inc. from 12/15/2018 to 03/27/2019. The raw data represented the distance from the water level to the ground surface. The real elevation of water table was obtained by subtracting the piezometer measurement from the ground elevation at the location of the bore holes. Besides, the rainfall in this area is shown in Fig. 3.26. The high magnitude of rain fall on the night before the recording data dates (for instance Feb 7th 2019) has an influence on the piezometer measure.

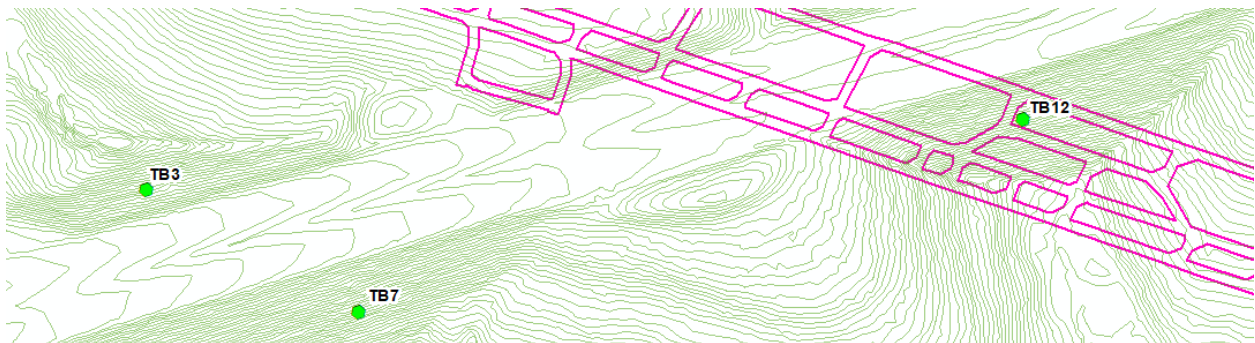


Figure 3.24. An overview of the layout of three piezometers

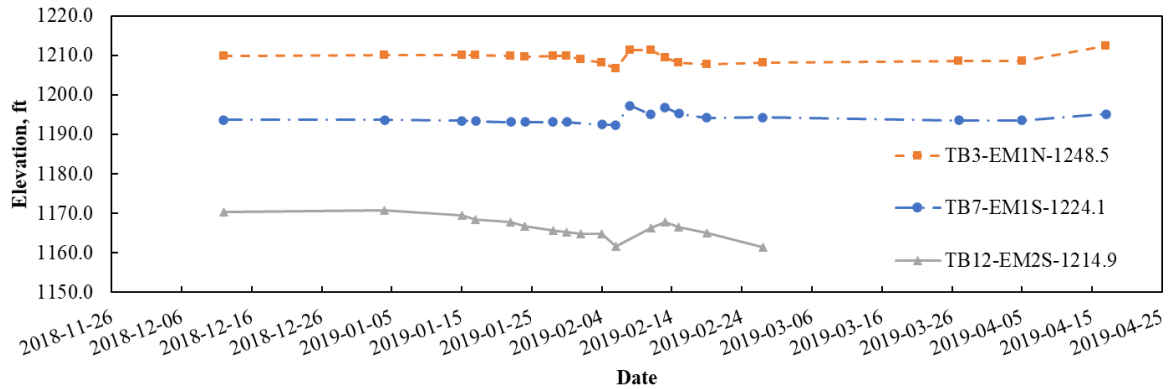


Figure 3.25. Ground water level through dates on three piezometers

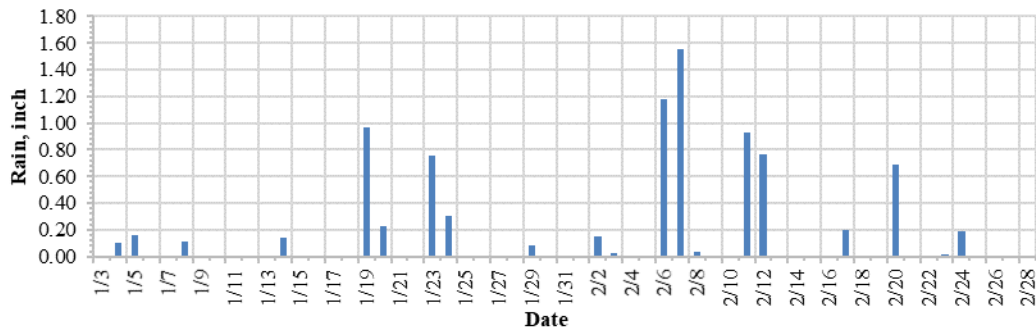


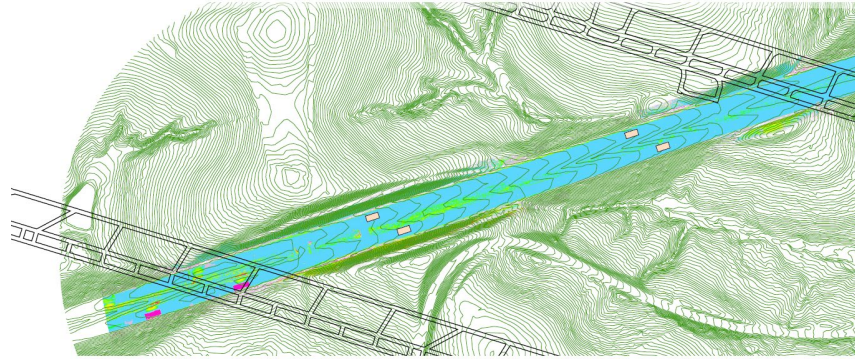
Figure 3.26. Plot of the magnitude of rainfall on different dates

In addition, different variations of water levels in different locations are observed. The different influences of mining on the ground movements in the center and on the edge of the panel contributed to the differing impacts on the water table. The ground on the edge experienced tension or compression permanently during the mining process while the ground in the middle of panel first underwent tension and then compression before stabilizing. The water table will change in response to the movement of the ground. Consequently, the water table in the middle of the panel (TB-3 and TB-7) first dropped and then increased, staying elevated during rainfall and ultimately dropping to a level slightly lower than the pre-mining conditions. Moreover, the water table on the edge of panel (TB-13) continued dropping until the bottom of the bore hole was dry. It never returned to the pre-mining conditions even during periods of rainfall. The water table location will

be considered in the Finite Element analysis in order to explore its influence on the slope stability of the embankments.

3.2.4 Lidar Surveys

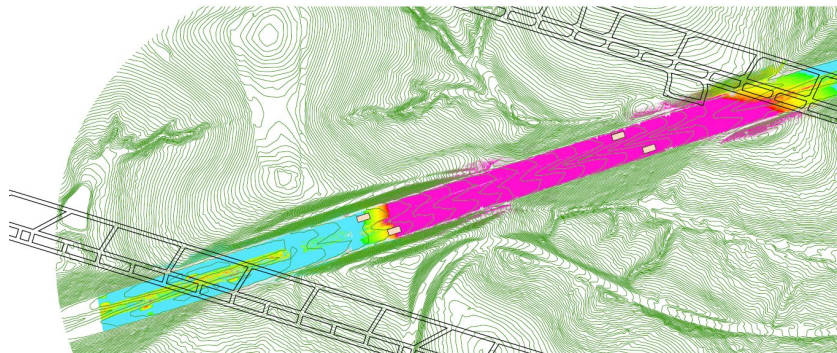
The figure below (Fig. 3.27) indicates the Lidar scans from T3 Global on the vertical subsidence taken along the highway alignments before, during and after mining. From an analysis of this figure, the way the vertical subsidence extended along the highway surface when the mining excavation moved forward can clearly be seen. The location and the amount of this vertical subsidence will be compared with the location and the amount of the vertical subsidence obtained with the numerical analysis that uses the FEM. This will be done in order to check the accuracy of the results obtained by the FEM.



(a)



(b)



(c)

Figure 3.27. Vertical subsidence of the highway embankment from Lidar scans (a) before mining (b) during mining and (c) after mining

4.0 Building up a Three-Dimensional Regression Model of the Ground Subsidence

A three-dimensional regression model of the subsidence profile was constructed using a SDPS model that was calibrated to field measurements. The regression model will be applied to the bottom of the Finite Element model of the embankments to simulate the vertical subsidence that occurred below the embankments as a result of longwall mining. The influence of topography on the resulting regression model was also considered in its development.

4.1 Regression Modeling of the Vertical Subsidence

The subsidence profiles are applied to the bottom the Finite Element models to simulate the behavior of embankments subjected to longwall mining. Only vertical subsidence was considered in this study because the SDPS model of horizontal movements cannot match well with the field data according to the SDPS modeler. The Richard Model [29] [42] was utilized to construct the regression model of the subsidence as

$$\frac{S}{S^*} = \frac{1}{\left[1 + e^{-\left(a_1 + a_2 \frac{x}{H}\right)}\right]^{a_3} \left[1 + e^{-\left(a_4 + a_5 \frac{y}{H}\right)}\right]^{a_6}} \quad (4.1)$$

where S^* is the maximum subsidence, H is overburden, S is the subsidence at point (x,y) , $a_1 a_2 a_3 a_4 a_5 a_6$ are six constant parameters.

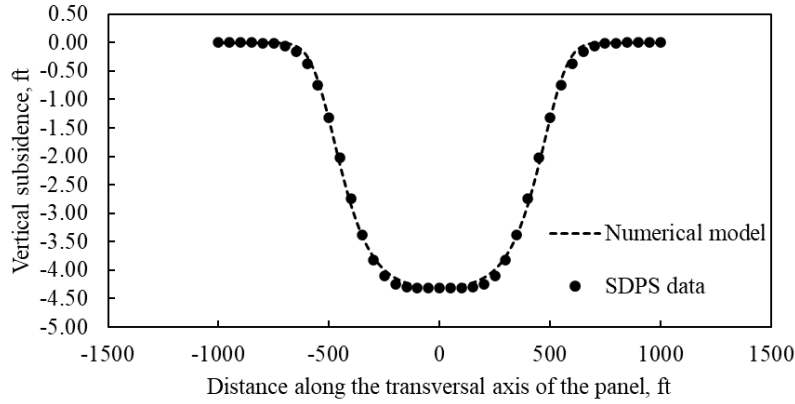
A Genetic Algorithm was applied to find the six unknown parameters in order to fit the regression function to the subsidence. In the process of applying the Genetic Algorithm, a fitness function is defined as the square error between the regression profile and the SDPS model as

$$\text{Fitness function} = \frac{\sum_{i=1}^n [S_i - S(x_i)]^2}{n} \quad (4.2)$$

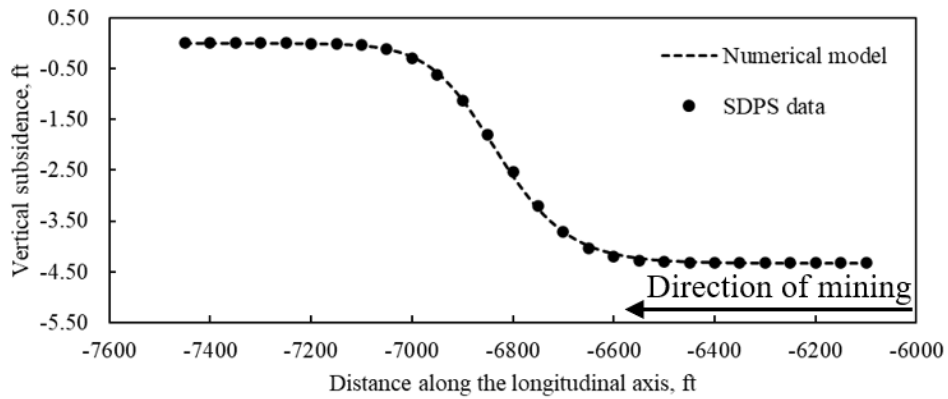
where n is the number of points, S_i is the subsidence from SDPS, $S(x_i)$ is the subsidence from the numerical fitting.

The resulting regression fitting functions were plotted along the transversal and longitudinal axis of the mining panel in two dimensions as well as in three dimensions as shown in Figs. 4.1 (a), (b) and (c) respectively. The figures indicated that the numerical fitting functions accurately simulated the actual formation of the subsidence basin.

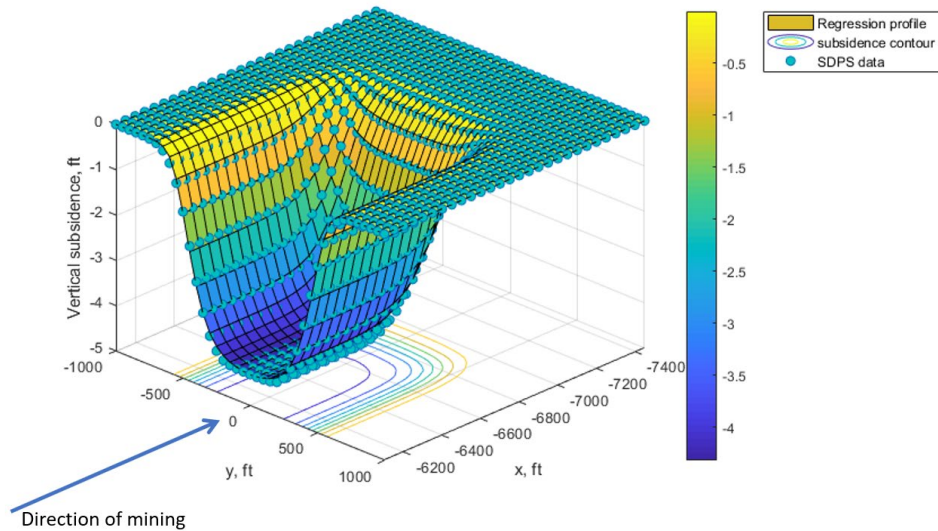
It should be noted that only vertical subsidence showed a good match to the field measurement and only vertical subsidence was considered in this study. This model was constructed based on a flat ground surface. The influence of the topography will be discussed in the following chapter.



(a) Numerical regression model of SDPS data for 2D vertical subsidence along the transversal axis of panel



(b) Numerical regression model of SDPS data for 2D vertical subsidence along the longitudinal axis of panel



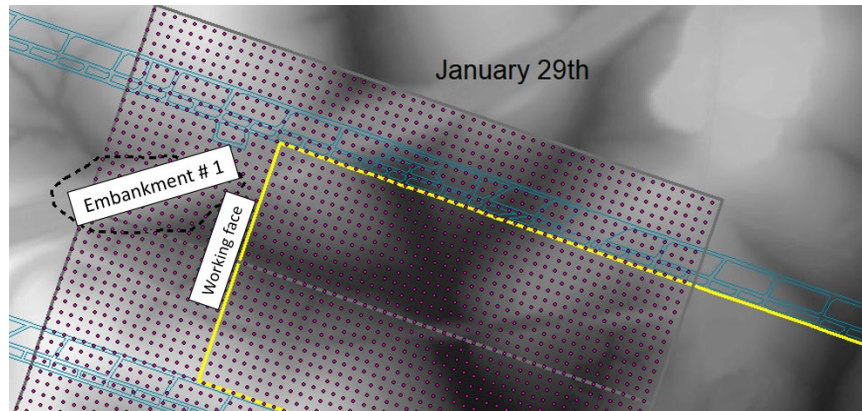
(c) Numerical regression model of SDPS data for 3D vertical subsidence

Figure 4.1. Regression model of the vertical subsidence (a) along the transversal axis; (b) along the longitudinal axis and (c) in three dimensions. (The SDPS data is denoted by the blue solid circles; the numerical regression profile with topography is denoted by colored rectangles)

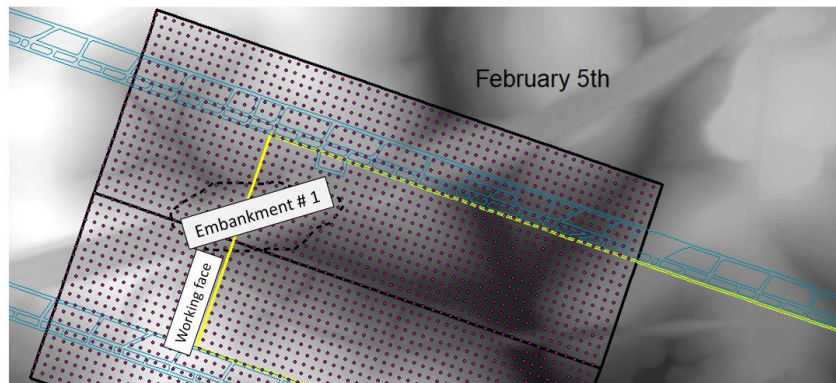
4.2 Influence of Topography on the Profile of Subsidence

The regression model of the subsidence profile constructed is based on the assumption that the ground surface is flat. However, the true ground surface in the study area of the embankments is not a flat one. Three locations of the working faces of Panel 15 were selected to analyze the influence of the changed topography of the ground surface on the resulting subsidence profiles. SDPS models were first utilized to simulate the ground surface considering the topography. Then the comparisons among the regression models of these SDPS models with different conditions of topography were analyzed. The purpose of this study is to determine whether or not the topography should be considered during the process of constructing the subsidence profile and analyzing its influences on the embankments.

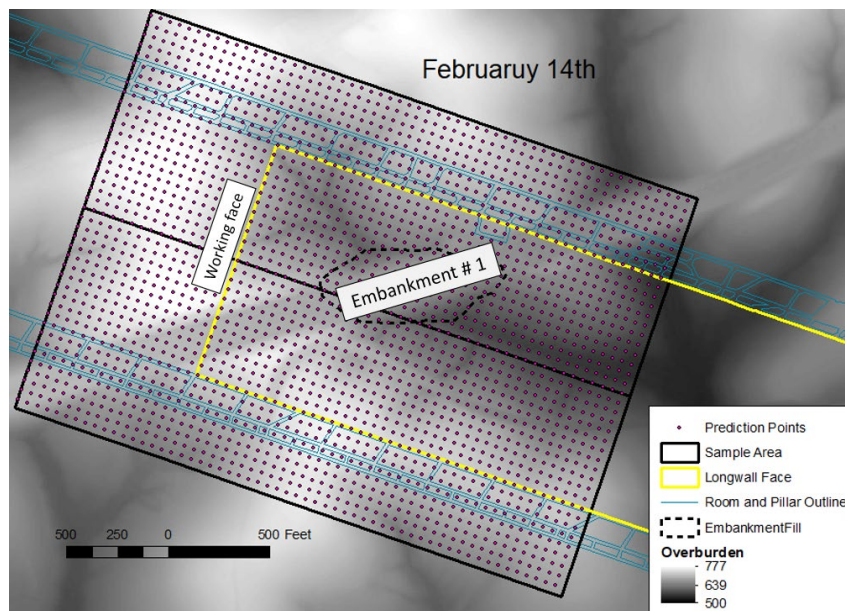
A comprehensive comparison was made between the regression model based on a flat ground surface and three regression models based on the selected ground surfaces over the head of Panel 15 with three corresponding working faces as shown in Fig. 4.2. These three longwall face positions capture the most important deformations applied to the embankment as the panel was extracted. Comparisons based on these three data sets show the difference between the subsidence taking into consideration the ground surface topography and that of assuming a flat ground surface.



(a) longwall face on 29 January 2019



(b) longwall face on 5 February 2019

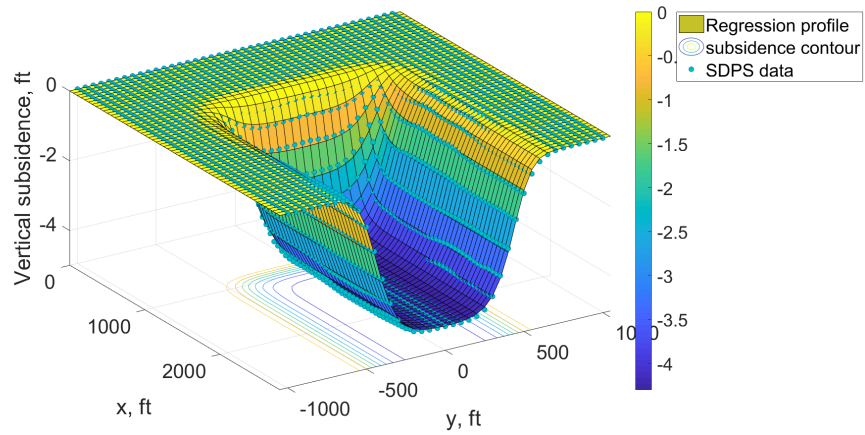


(c) longwall face on 14 February 2019

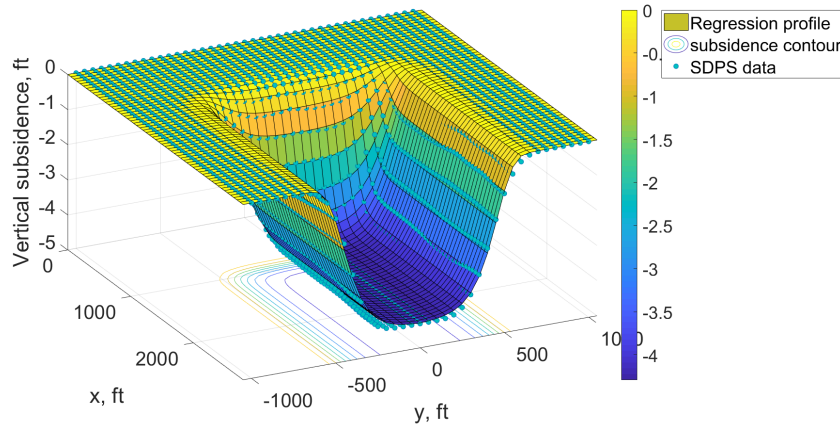
Figure 4.2. Three positions of working faces and the corresponding ground surface data sets

The fitted regression functions of the subsidence profiles on the three selected regions with topography were plotted in Figs. 4.3 (a), (b) and (c) respectively. The SDPS profile with topography is denoted by the blue solid circles and the numerical regression profile with topography is denoted by colored rectangles. The error between the regression and the SDPS data is rather small and most blue balls (SDPS data) lie directly on surface contours (regression), indicating that the regression model accurately represents the SDPS model output.

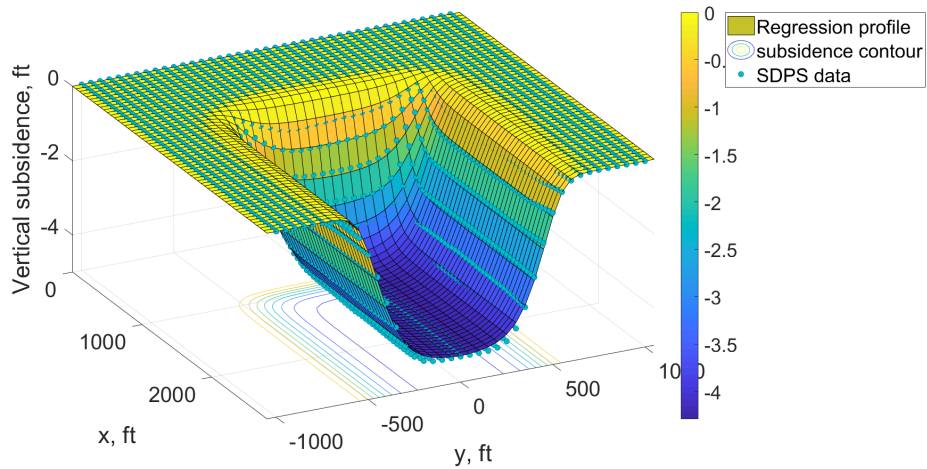
The resulting subsidence regression models at three areas with topography were compared to that assuming a flat ground surface, as shown in Fig. 4.4. The subsidence regression model of the ground surface assumed to be flat and those considering topography are very similar except for the shoulder of the subsidence basin where a small discrepancy can be observed. Overall, the two regressions are very close to each other in most parts of the basin, especially on the front of the subsidence that will touch the bottom of the embankments.



(a) 29 January 2019

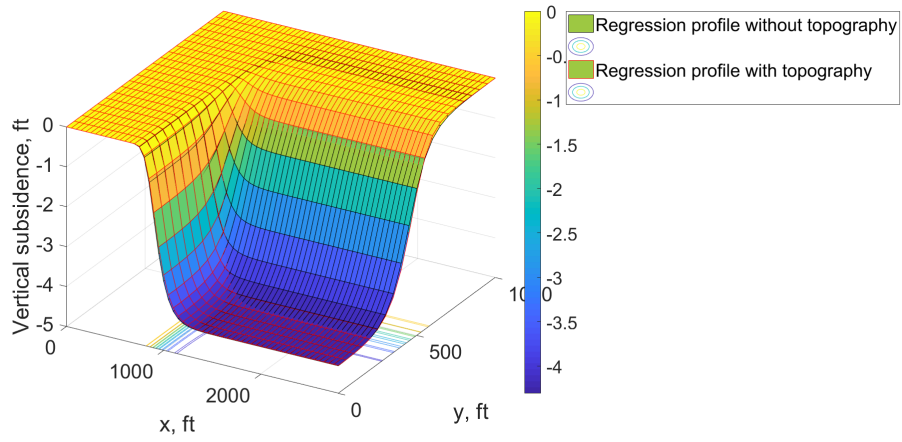


(b) 5 February 2019

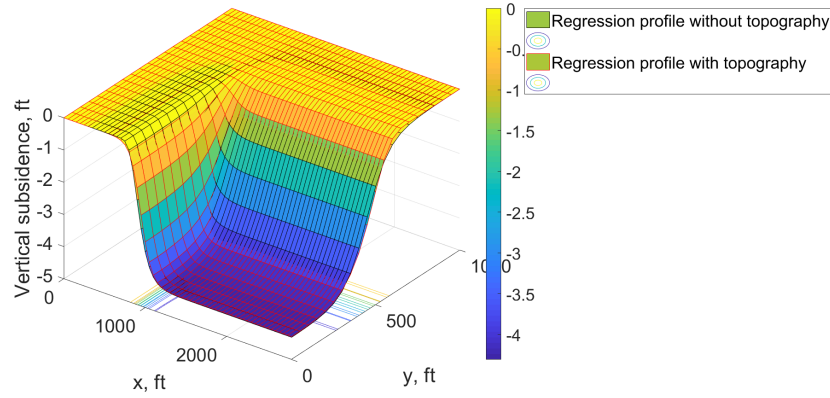


(c) 14 February 2019

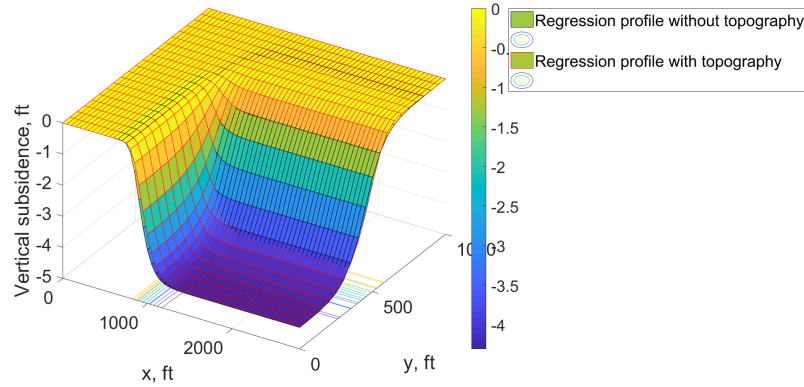
Figure 4.3. Numerical regression results considering the topography at three longwall face positions (a) 29 January 2019; (b) 5 February 2019 and (c) 14 February 2019.



(a) 29 January 2019



(b) 5 February 2019



(c) 14 February 2019

Figure 4.4. The subsidence regression model with topography was compared to that without topography on the following longwall position dates: (a) 29 January 2019; (b) 5 February 2019 and (c) 14 February 2019

The different overburden in these three specific regions may account for the subtle difference on the shoulder. The overburden in the regression model assuming a flat ground surface is a uniform 675ft. However, the overburden in these three ground data sets is summarized in Table 4.1. The overburden of the first two subsidence regressions is less than the regression using a flat ground surface. The lower overburden resulted in a smaller curvature on the shoulder as shown in Figs. 4.4 (a) and (b). When the overburden is the same as on February 14, 2019, the subsidence basin shapes are nearly identical.

Table 4.1. Overburden of areas near the three positions of longwall face

Areas of the SDPS data		Average overburden, ft
Considering Topography	29 January 2019	637
	5 February 2019	638
	14 February 2019	678
Flat ground surface		675

5.0 Developing a Finite Element Model of the Highway Embankment Impacted by Longwall Mining Subsidence

A three-dimensional Finite Element model of Embankment #1 was constructed using a FEM commercial package called ABAQUS. A generalized layered model was constructed using the soil profiles from the test borings. Material properties of the soils forming part of the embankment were obtained from laboratory tests. Modifications were applied to the material properties of the soil matrix on which the materials properties were measured in order to account for the concentration by volume of the dispersed limestone rock fragments present in the soil (Table 3.2).

5.1 Geometry of Embankment #1

The outline of Embankment #1 can be determined from the topography map shown in Fig. 5.1. The contour lines parallel to the highway represents the slope parts of the embankment going down from the crest to the toe. The contour lines changed in direction when reaching the outer limits of the embankment.

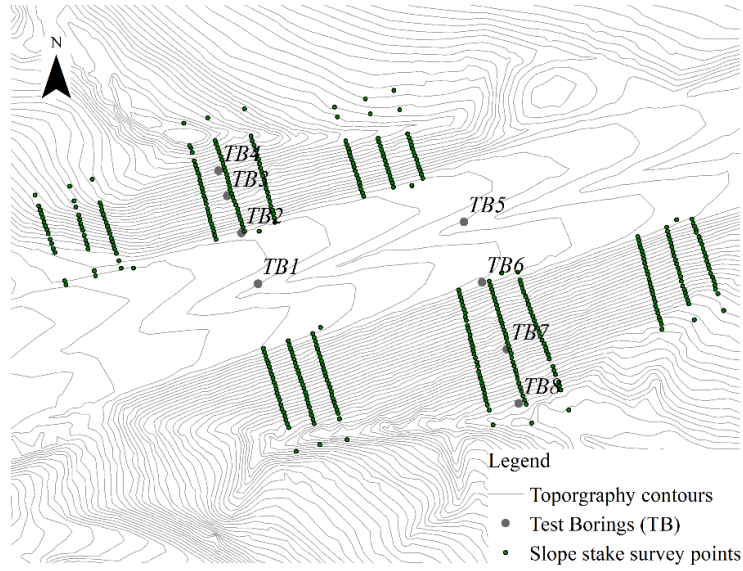


Figure 5.1. Topography map of Embankment #1

The points on the edge of the parallel lines that differentiate the embankment from the other parts of ground were connected to generate an outline of Embankment #1 shown in Fig. 5.2. The elevations of toes of the embankment were 1220-ft and 1190-ft on the north and south respectively. Based on this obtained geometry, twelve control faces were selected to reflect the major geometry of the embankment shown in Fig. 5.2.

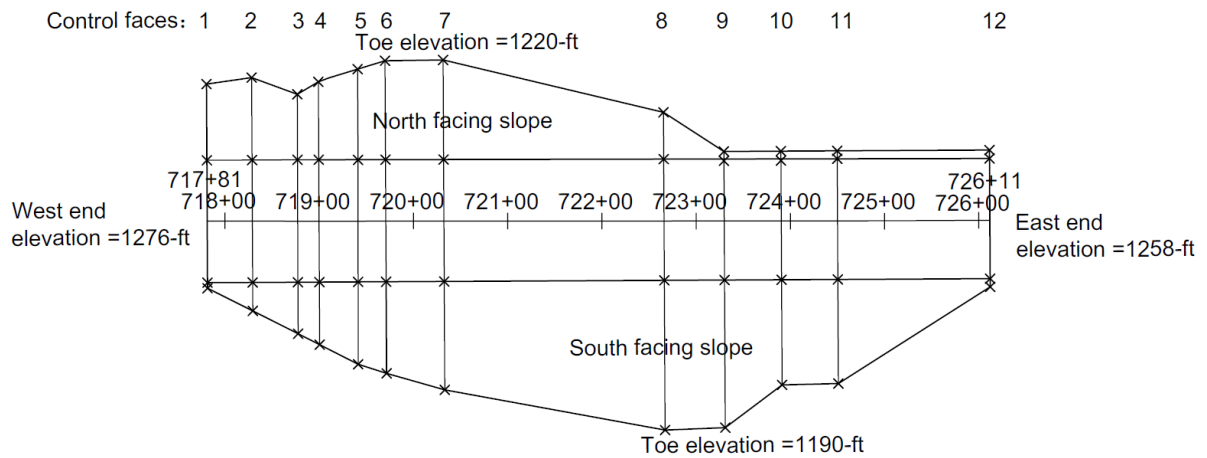


Figure 5.2. Overview geometry of Embankment #1

After determining the horizontal coordinates of each point, vertical coordinates (elevation) were determined. The elevations of the 24 points on the crest of the embankment (edges of highway) were firstly determined considering the slight slope on the highway shown in Fig. 5.3 (a). Then the magnitude of slope of the embankment was utilized to determine the elevation of the points on the bottom (northern and southern respectively). The resulting twelve control faces are shown in Fig. 5.3 (b).

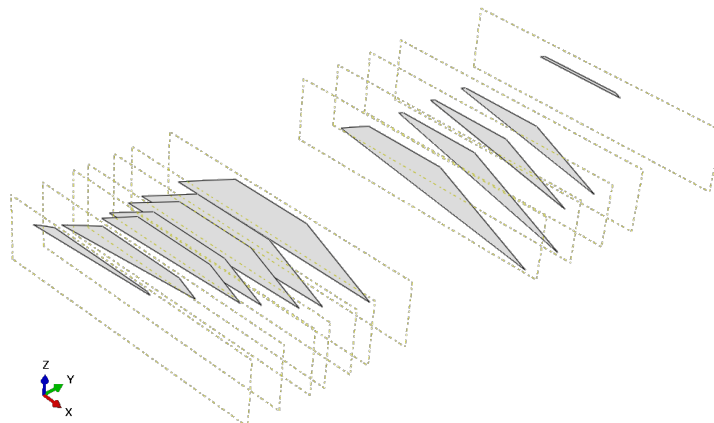
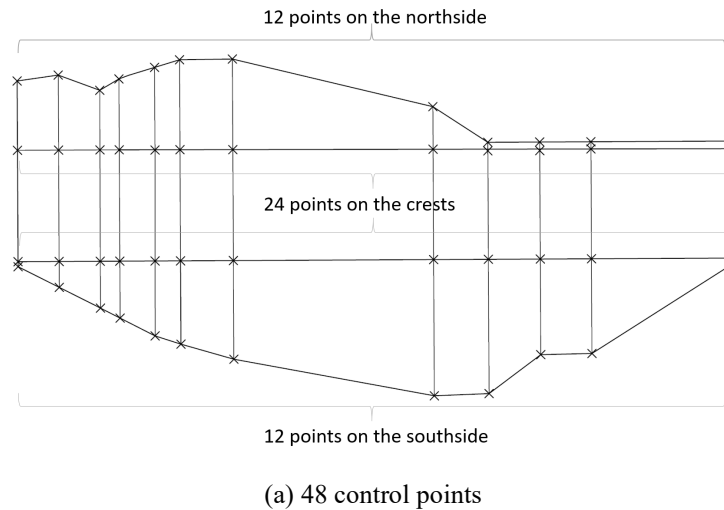


Figure 5.3. Geometry of the uniform 3D model of Embankment #1

Overall, Embankment #1 is 54-ft high on the north-facing slope and 72-ft high on the south-facing slope. It is 234.72-ft wide (perpendicular to the highway) and 830.67-ft long (parallel to the highway). The magnitudes of slope of highway, the north-facing slope and south-facing slope are calculated as

$$\begin{aligned}
 slope_{pavement} &= \frac{\text{change in elevation}}{\text{total length}} = \frac{1276 - 1258}{830.67} = 0.022 \\
 slope_{north\ slope} &= \frac{\text{change in elevation}}{\text{total length}} = \frac{54}{105.21} = 0.513 \\
 slope_{south\ slope} &= \frac{\text{change in elevation}}{\text{total length}} = \frac{72}{158.61} = 0.454
 \end{aligned} \tag{5.1}$$

5.2 Interior Soil Profiles for Different Layers in Embankment #1

According to the laboratory tests of the soil samples taken in the field, the embankment is made up of layers of different types of soil. The researcher started from the two cross sections based on the test borings shown in Fig. 5.4 and 5.5. Also, a simplified layered model is proposed based on the generalization of these two cross sections, making it possible to obtain a good result of mesh grid in this complex three-dimensional FEM model. With the two-layer model, the computational time to obtain the deformations and stability of the embankment will be substantially shortened.

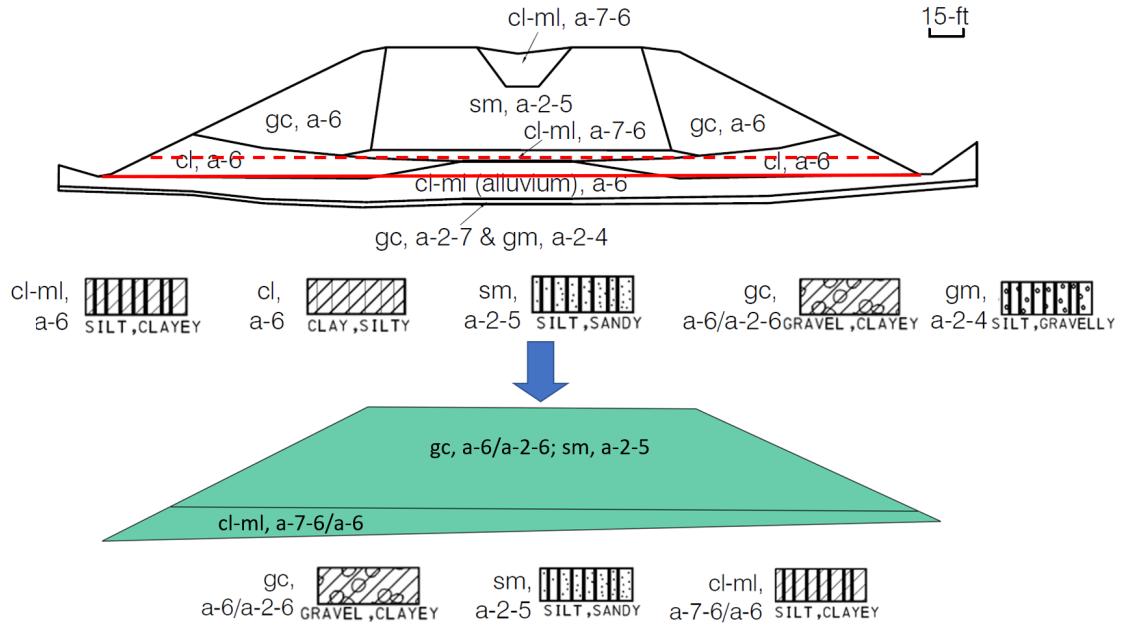


Figure 5.4. Simplified cross section in 3D model obtained from the simplified 2D model at 720+00

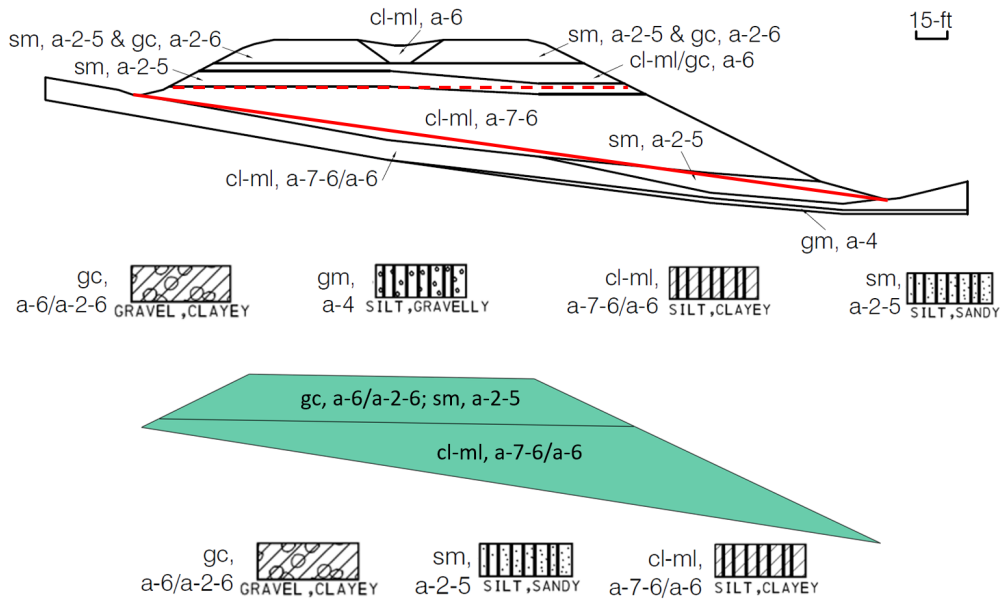


Figure 5.5. Simplified cross section in 3D model obtained from the simplified 2D model at 720+50

The geological conditions in the study area can be obtained analyzing the interior soil profiles at these two cross sections. The embankment was constructed within a valley and on an uneven ground surface. The southern side was lower than the northern side in the cross section at 720+50. The lower part of both cross sections was made up of soil that is similar to an alluvium indicating that the embankment was constructed using the soil from a nearby area. Then the soil with large rock particles was utilized to fill the upper parts of the embankment.

The generalized configuration utilized to construct the other cross sections in Embankment #1 is shown in Fig. 5.6. The elevation of the platform in each cross section was determined by the average measurement from the two known cross sections, that is, 4-ft above the higher toe of each cross section.

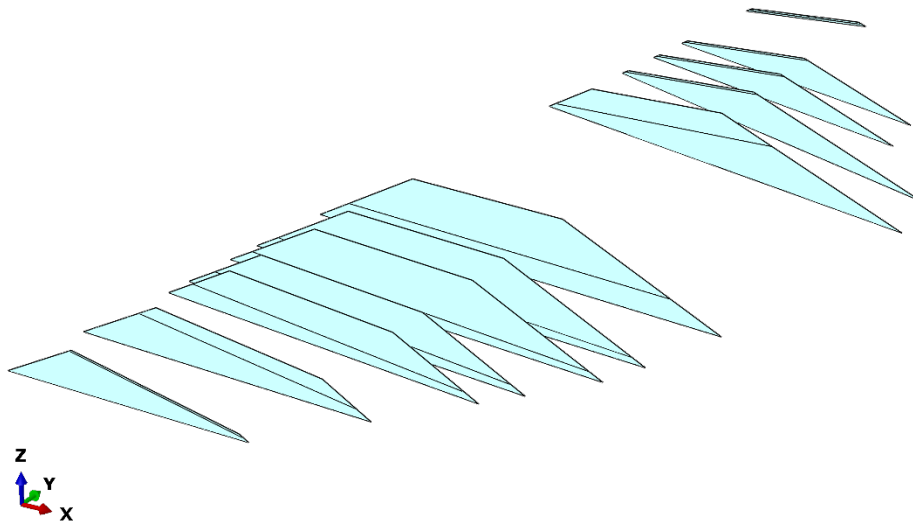
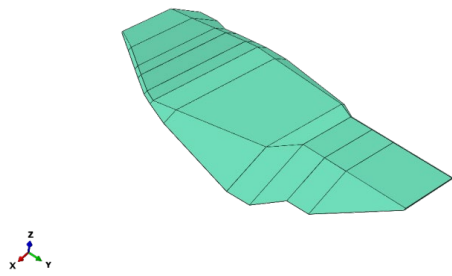


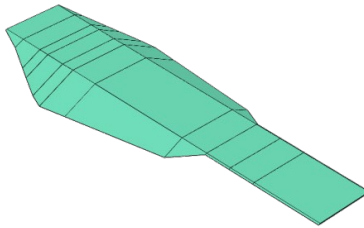
Figure 5.6. All twelve control faces in constructing the three-dimensional layered model

The embankment can be divided into two parts in the perspective of construction procedure. The valley was first filled with soil in the lower part which was similar to alluvium to make the ground surface horizontal along the transversal direction of highway shown in Fig. 5.7 (a). The

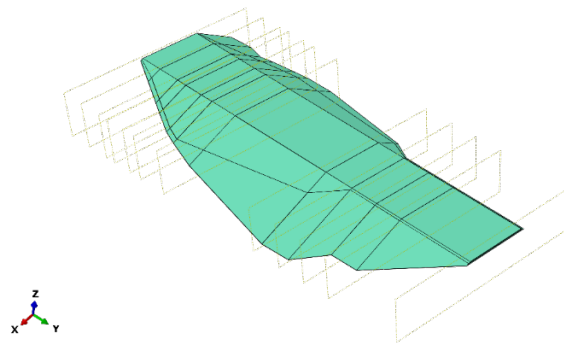
material at the lower part is made up of clayey silt and has an a-7-6 in the AASHTO classification and can be located at both cross sections 720+00 and 720+50. Then a sandy silt (a-2-5) and a laterally-located gravelly silt (a-4) are shown in Fig. 5.7 (b). These soil types were placed on the top of the platform to construct a longitudinally flat surface for the highway alignments as shown in Fig. 5.7 (c).



(a) lower part of Embankment #1, clayey silt



(b) upper part of Embankment #1, combination of clayey gravel and sandy silt



(c) resulted layered three-dimensional Embankment #1

Figure 5.7. Configuration of three-dimensional Embankment #1 with two layers

The general configuration of the cross section of the embankment made it possible for the layered 3D model to be implemented in the FEM model. This model will be helpful for the construction of other embankments. An overview of the final layered embankment is shown in Fig. 5.8.

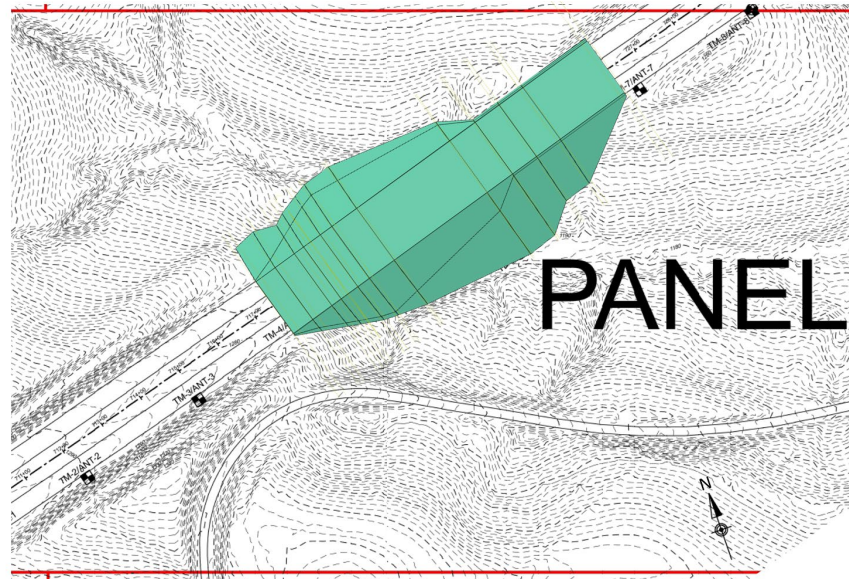


Figure 5.8. Overview of the resulted 3-D FE model of Embankment #1 in the Panel 15

5.3 Material Properties of the Simplified Layered Finite Element Model

Certain adjustments were applied on the initial material properties described in Chapter 3. Previous research provided guidance for the adjustments. Sensitivity tests were conducted to determine the shear strength parameters utilized in the calibrated two-layered FEM model. According to the boring logs analyzed before, clayey gravel (soil with rock segments) is located at the lateral parts of embankment at cross section 720+00 and middle depth at cross section 720+50, indicating that the rock ratio of the upper layer is rather high. However, only soil samples

with a lower rock ratio were tested in the triaxial compression tests. Triaxial compression tests provide the shear strength parameter values (cohesion and friction angle values) needed for the analysis of deformation and stability of the embankment.

From the laboratory tests, the friction angle for sandy clayey gravels increases from 34° to 36° as the gravel concentration by weight ratio rises from 20% to 40% in the lower part of the embankment, which is similar to the results of previous research findings shown in Fig. 5.9. The result of this previous research can be utilized to determine the friction angle of the gravel-soil mixtures that form the embankment. This previous research indicates the effect of the concentration by weight of the gravel in the mixtures on their friction angle values (Fig. 5.9).

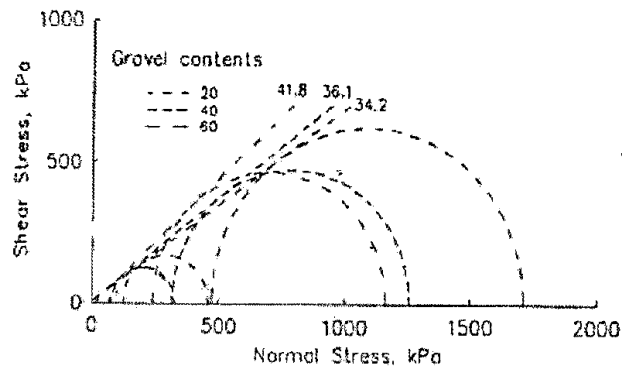


Figure 5.9. Variation of shear strength of sand-clay gravels with changes of rock ratios [39] [40]

The shear parameters of the soil matrix in the soil-rock mixture can be obtained from either the triaxial or the direct shear tests. A Friction angle of 34° for the silty-clay obtained from borehole TB-1 at a depth of 6 to 10-ft can be utilized as a representative friction angle for the soil.

For the clayey gravel in the upper layer, the concentration by weight of the rock fragments is as high as 50%. According to a plot from the previous research (Fig. 5.9) conducted by Iannacchione and Vallejo [39] [40] [41], the friction angle can be increased to 40-42 degrees for

the soil in the upper part of the embankment. For the cohesion, direct shear tests were conducted. According to the direct shear tests on the gravel with a higher rock concentration ratio by weight of 48%, the cohesion is 792-psf, which is identical to those with a lower rock concentration. This indicated that the gravel concentration ratio by weight of 48% will not cause a decrease of the cohesion of the soil. In other words, the clayey gravel in this embankment constructed in 1960s with a rock concentration ratio by weight of 48% has both: high values of friction and cohesion. Direct shear tests provide the accurate cohesion of the clayey gravel with a high value of rock ratio. That is, the influence of gravel on the mobilized cohesion value of a soil-rock mixture during subsidence can be obtained from the direct shear test results. The shear strength of soil subjected to the large deformation is calculated by Johnson [43] as

$$s = c + (\sigma_n - u) \tan \phi + \eta \frac{dv}{dy} \quad (5.2)$$

where s is denoted as the shear strength of soil, c the cohesion of soil, σ_n the normal stress applied on the soil due to gravity, u the pore water pressure, η the viscosity, and $\frac{dv}{dy}$ the change of is effective at large deformations. The influence of the third term in Eq. 5.2 is reflected in the behavior of the embankment during the subsidence process: the embankment during deformation remained stable because of the strain hardening behavior of the soil (Fig. 3.4).

For the case in which rock fragments are dispersed in a soil matrix, the shear strength of the mixture can be obtained from the following relationship according to Vallejo et al. [44] and Vallejo and LoboGuerrero [45],

$$s = [c + (\sigma_n - u) \tan \phi][1 + 2.5C] \quad (5.3)$$

where C is the concentration by volume of the dispersed rock fragments in the soil matrix.

The terms in the first parenthesis In Eq. 5.4 represent the shear strength parameters of the soil matrix. The concentration by volume, C , of the rock fragments in this matrix can be obtained from the concentration by weight, C_w , of the rock fragments using the following equation [46],

$$C = \frac{C_w}{G_s - (G_s - 1)C_w} \quad (5.4)$$

where G_s is the specific gravity of the soil which is usually assumed to be 2.65.

For the clayey silt in the lower layer, during the procedure of subsidence, the embankment experienced consolidation according to the highway alignment monitoring and slope stake surveys conducted by Penn DOT. The dispersed rock fragments in the soil becomes closer to each other and the concentration of the gravel in the soil (C_w) will increase in the process, That is, the concentration by weight of the gravel will be larger than the original 40% in the lower layer, which means that the friction angle for the lower layer will be larger than 38-degree.

The constitutive law of soil in the embankment is elasto-plastic (Fig. 5.10) and elasto-plastic with subtle strain-hardening trend (Fig. 3.4). Duncan-Chang's model has been widely utilized to accurately simulate the non-linear elastic response of soil mass and rockfill [47][48][49][50][51][52][53]. A two-constant hyperbolic law was firstly utilized by Kondner [54] to fit the stress-strain relationship from a triaxial compression test on soil as

$$\sigma_1 - \sigma_3 = \frac{\varepsilon_1}{a + b\varepsilon_1} \quad (5.5)$$

where σ_1 is the major principal stress, σ_3 the minor principal stress, and ε_1 the axial strain (major principal strain). According to Kondner and ZelasKo [55], a and b are expressed as

$$a = \frac{1}{E_i} \quad (5.6)$$

$$b = \frac{1}{(\sigma_1 - \sigma_3)_{ult}}$$

where E_i denotes the initial tangent modulus, $(\sigma_1 - \sigma_3)_{ult}$ the ultimate deviator stress (normal stress difference) which represents the asymptotic value of the hyperbolic curve. The ultimate deviator stress is greater than the strength of soil $(\sigma_1 - \sigma_3)_f$ (deviator stress at failure) that is governed by the Mohr-Coulomb criteria as

$$(\sigma_1 - \sigma_3)_f = \frac{2c \cos \phi + 2\sigma_3 \sin \phi}{1 - \sin \phi} \quad (5.7)$$

where c is the cohesion, and ϕ is the friction angle of soil. A parameter called failure ratio, R_f is utilized to relate the $(\sigma_1 - \sigma_3)_f$ with $(\sigma_1 - \sigma_3)_{ult}$ as

$$(\sigma_1 - \sigma_3)_f = R_f (\sigma_1 - \sigma_3)_{ult} \quad (5.8)$$

For the reason that $(\sigma_1 - \sigma_3)_f$ is less than $(\sigma_1 - \sigma_3)_{ult}$, R_f is less than 1 and found to be in the range of 0.75 to 1 according to Duncan and Chang [47].

The initial tangent modulus E_i was related to the confining pressure, σ_3 by Janbu [56] as

$$E_i = K p_a \left(\frac{\sigma_3}{P_a} \right)^n \quad (5.9)$$

where p_a is the atmospheric pressure, K and n are modulus number and modulus exponent, respectively. The material parameters K and n are determined by plotting the E_i/P_a versus σ_3/P_a from the series of triaxial tests on a log-log scale. A fitting straight line can be obtained taking $\log(E_i/P_a)$ as y and $\log(\sigma_3/P_a)$ as x . K is found to be equal to the intercept of the straight line on the y -axis and n is the slope of the line.

The tangent modulus E_t is obtained by Duncan and Chang [47] as

$$E_t = (1 - R_f S)^2 E_i \quad (5.10)$$

where S denotes the stress level as is calculated as

$$S = \frac{\sigma_1 - \sigma_3}{(\sigma_1 - \sigma_3)_f} \quad (5.11)$$

Then the tangent modulus E_t at a given stress state can be obtained by substituting Eq. 5.7, 5.9 and 5.11 into Eq. 5.10 as

$$E_t = \left(1 - \frac{R_f(1 - \sin \phi)(\sigma_1 - \sigma_3)}{2 c \cos \phi + 2 \sigma_3 \sin \phi}\right)^2 K P_a \left(\frac{\sigma_3}{P_a}\right)^n \quad (5.12)$$

When the deviator stress $(\sigma_1 - \sigma_3)$ is less than its maximum value in history, the unload-reload modulus is adopted and defined as

$$E_{ur} = K_{ur} P_a (\sigma_3 / P_a)^{n_{ur}} \quad (5.13)$$

where K_{ur} is the unload-reload modulus number which is normally greater than the modulus number K (usually taken as 1.5~3.0 K [57]) and n_{ur} is the unload-reload modulus exponent which is usually equal to the modulus exponent n .

In the E-v model proposed by Kulhawy and Duncan [48], the tangent Poisson's ratio v_t is given as

$$v_t = \frac{G - F \lg(\sigma_3 / P_a)}{(1 - A)^2} \quad (5.14)$$

where A is expressed as

$$A = \frac{D(\sigma_1 - \sigma_3)}{K P_a (\sigma_3 / P_a)^n (1 - R_f S)} \quad (5.15)$$

and G , F , and D are the material parameters.

The detailed algorithm for the UMAT subroutine in ABAQUS is shown in Appendix A. The confining pressure and the final deviator stress are defined using the values from the laboratory test. The resulted deviator stress versus strain curve obtained by the E - ν model from the simulated triaxial compression test was shown in Fig. 5.11, presenting good agreement with the laboratory test. The parameters that gave the good consistence with the laboratory results are shown in Table 5.1.

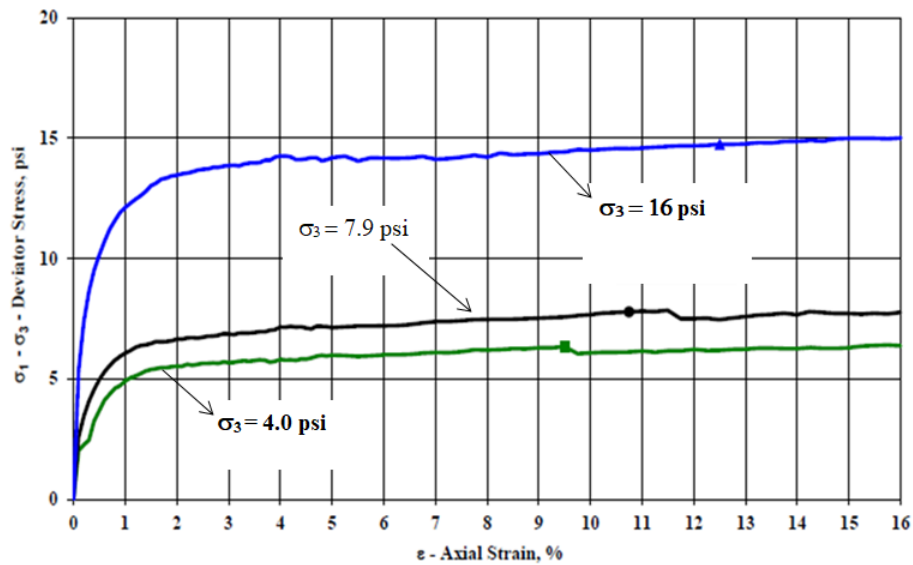


Figure 5.10. Stress-strain relationship for soil forming part of Embankment #1

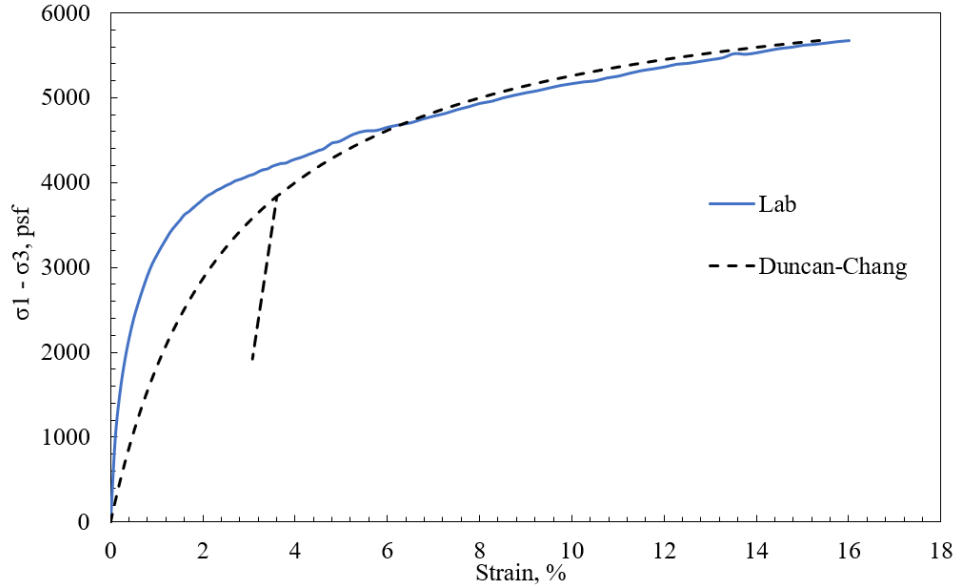


Figure 5.11. Comparison between the laboratory test and the Duncan-Chang model in the stress -strain curve

Table 5.1. Parameters utilized in the Duncan-Chang E-v model

K	n	Rf	Φ (°)	G	K_{ur}	D	F
110	0.1	0.9	40	0.3	160	0	0

In the Duncan-Chang model, the Jacobian matrix is updated in each increment based on the variation of strain. When the embankment is subjected to subsidence, large deformation happens, making Duncan-Chang’s model too expensive in computational time. Previous research has utilized elasto-plastic model to simulate the embankment fill by Stilger [33] and Liu et al. [34]. An elasto-plastic model is adopted in this study for Embankment #1 subjected to subsidence in order to simulate its behavior accurately and efficiently. The plastic behavior is governed by Mohr-Coulomb criterion. It is true that Mohr Coulomb criterion has its shortcomings, for instance, it cannot simulate the consolidation procedure nor the crack behavior in the embankment. Sensitivity tests were conducted to determine the shear parameters utilized in the elasto-plastic model,

comparing the simulated settlement to the field measurement from the slope stake survey. The material properties that gave the good results are summarized in Table 5.2.

Table 5.2. Material properties of the two-layered Finite Element model of Embankment #1

Layer name	Soil name	c (psf)	ϕ
Upper	Sandy silt/ Clayey Silt/ Clayey Gravel	775	42°
Lower	Clayey silt/Gravelly Clay	785	40°

6.0 Results of Finite Element Analysis of Embankment #1 Subjected to the Successive Subsidence due to Longwall Mining

The Finite Element model was obtained from a regression model of the vertical subsidence obtained from the SDPS model as indicated in Chapter 4 in order to simulate the behavior of the embankment under dynamic subsidence due to longwall mining. Vertical and horizontal deformation were analyzed in the stress-strain field analysis. Shear Strength Reduction Method (SRM) was utilized to find the critical sections with respect to deformations and stability in the embankment. Using these critical sections, the factor of safety was determined using SRM.

6.1 Deformation Analysis

The regression model was constructed using the Richard's model and fitted to the subsidence basin shown in Fig. 6.1. The successive numerical subsidence basin was then applied on the bottom of the FE model of Embankment #1 to simulate the deformation on the embankment influenced by the subsidence.

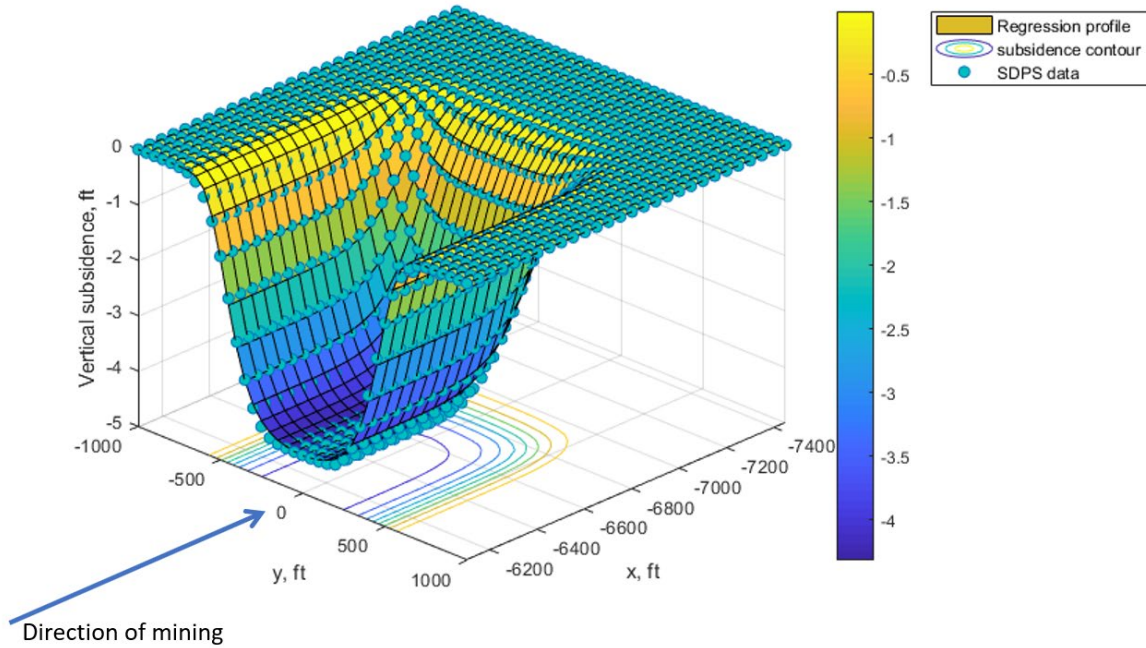


Figure 6.1. Numerical regression of a 3D subsidence basin

The coordinate system for the regression model was transferred to that of the embankment using the transformation equations. The subsidence basin was moved forward to simulate the vertical deformation of the embankment when the working faces was at different locations shown in Fig. 6.2.

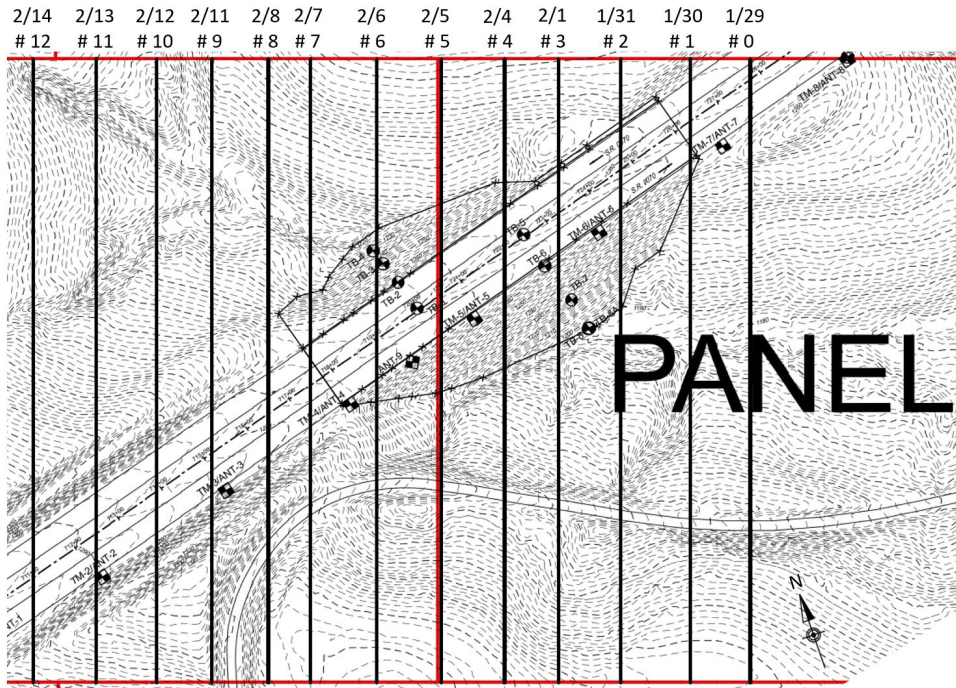


Figure 6.2. Locations of the working face on different dates

Figs. 6.3 (a) – (f) indicate the vertical displacement on the surface of the Embankment #1 subjected to subsidence at selected dates. The whole process of vertical displacement on the embankment is shown in Appendix B. The maximum vertical subsidence after mining will happen on the east bound lane in the middle of the highway segment shown in Fig. 6.3 (f).

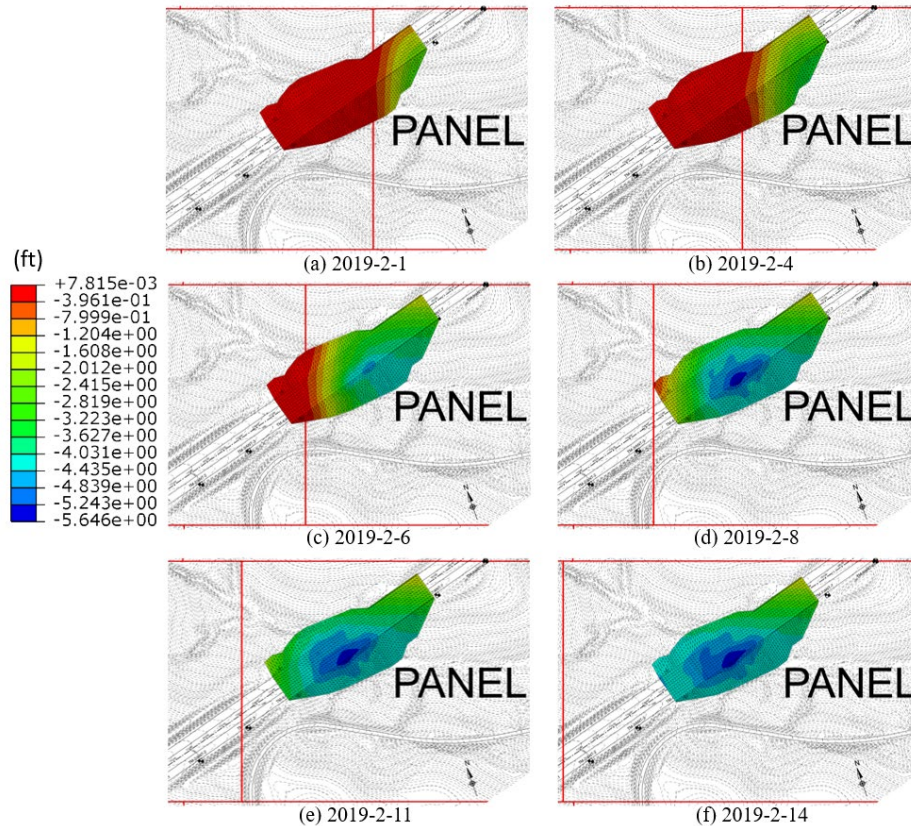
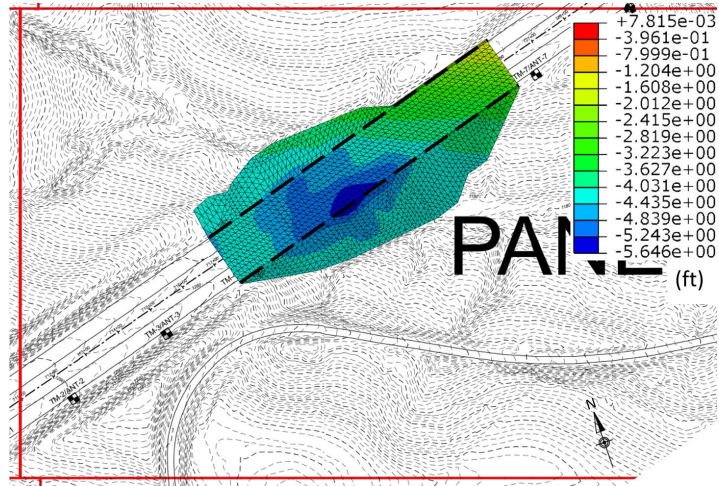


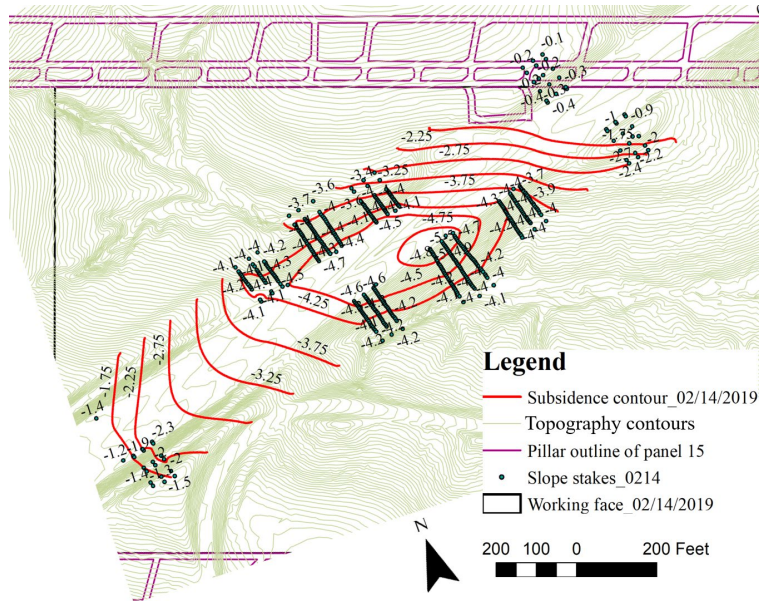
Figure 6.3. Subsidence on Embankment #1 subjected to successive subsidence on selected dates

Then the vertical displacement at the final stage of subsidence from the FEM model was compared to the field measurement shown in Figs. 6.4 (a) and (b), respectively. The vertical component of the displacement in the field was measured from the slope stake survey and was plotted using ArcGIS. In addition, the simulated and measured vertical displacement along the crests of the embankment were compared in Fig. 6.10 (c).

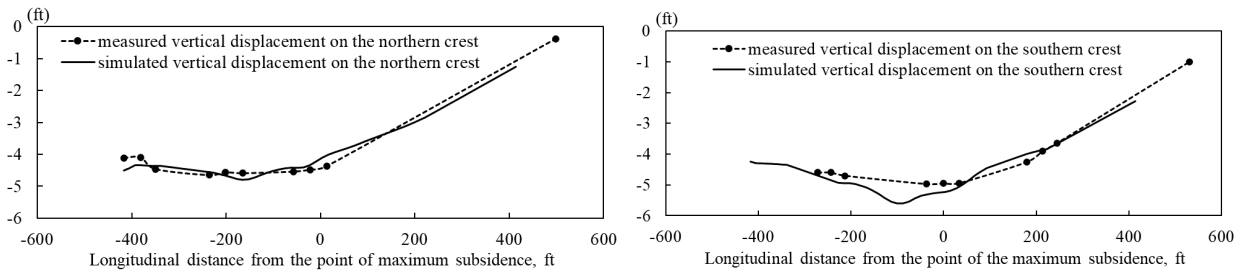
The FEM analysis indicates the region with the maximum displacement was located in the center of the highway segment on the east bound lane, showing good agreement with what was found in the field. The magnitude of the maximum displacement from the FE model was 5.6-ft, which was close to the field measurement of 5-ft. Thus, the FEM model predicts very well what is happening in the field.



(a)



(b)



(c)

Figure 6.4. Subsidence on the highway Embankment #1 due to longwall mining from (a) Finite Element model (b) field measurement and (c) Comparison between the two on the crests

In addition, the simulated vertical displacement was compared to the measured settlement at a selected slope stake survey point on different dates shown in Fig. 6.5. The selected survey point is located at the crest of the south-facing slope. It shows that the vertical displacement from the FE model fits well with the field measurement at the critical crest of the highway embankment subjected to a successive subsidence.

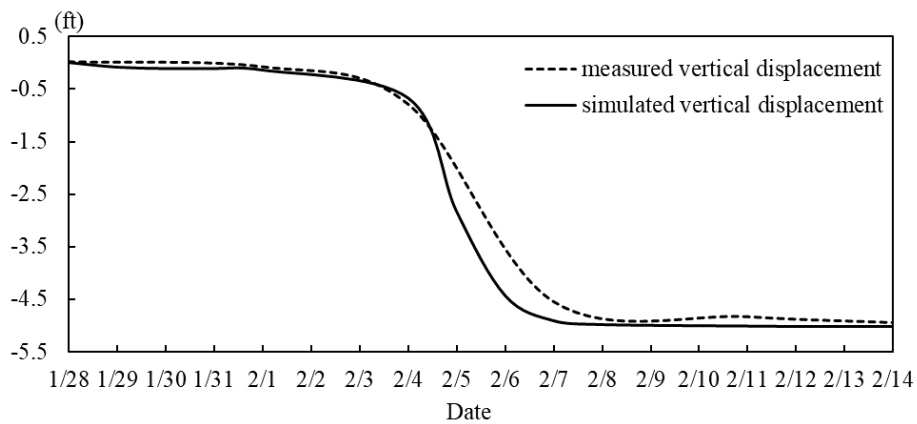


Figure 6.5. Comparison between the measured and simulated vertical displacement at the crest of a highway embankment on different dates

Furthermore, the deformation inside the embankment is plotted at the critical transversal cross section where the maximum subsidence happens (Fig. 6.6) and longitudinal cross section along the southern edge of highway (Fig. 6.7). The displacement on the top of the embankment is larger than that in the bottom. Besides, the settlement on the southern crest is larger than that on the northern crest, which is consistent with the field measurement.

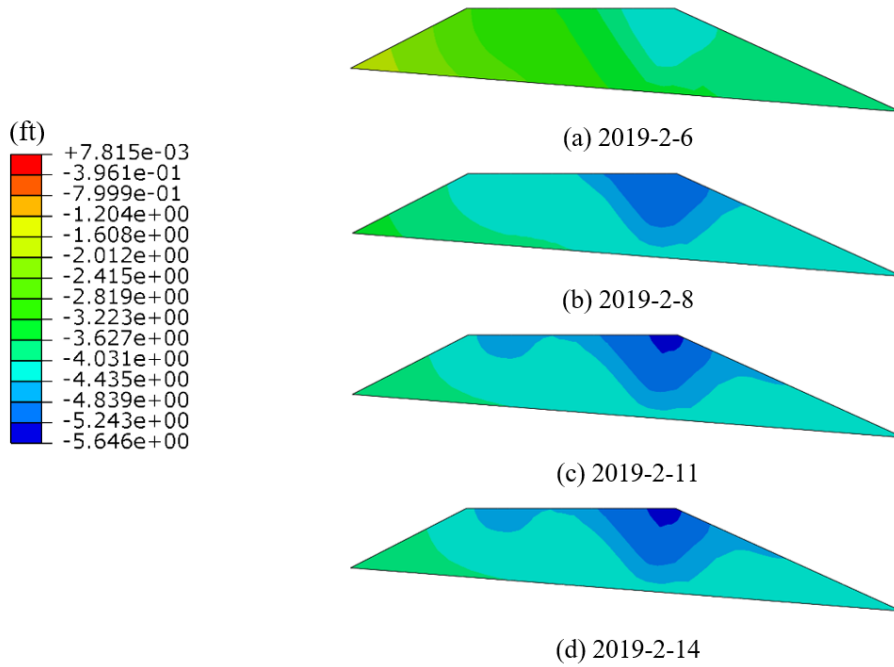


Figure 6.6. Simulated vertical displacement of a highway embankment at the critical transversal cross section with maximum subsidence on different stages of subsidence

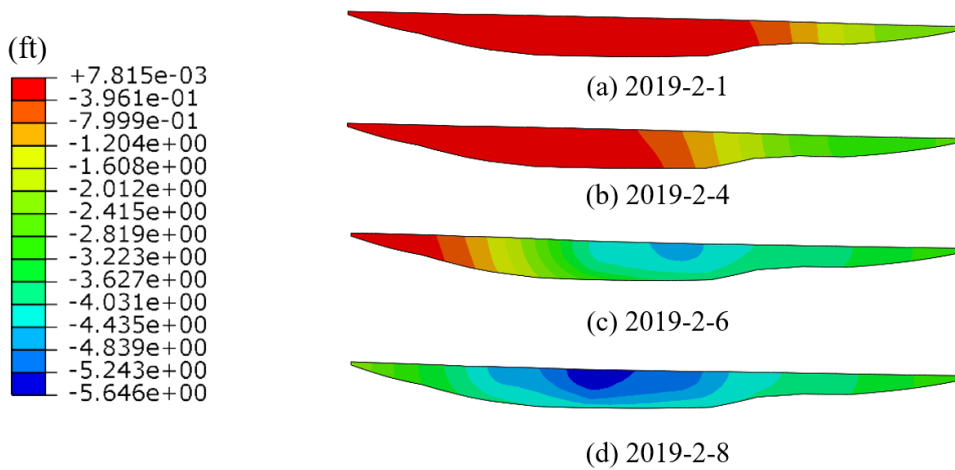


Figure 6.7. Simulated vertical displacement of a highway embankment at the longitudinal cross section along the southern edge of highway on different stages of subsidence

6.2 Stress and Strain Field in Embankment #1 due to Subsidence

During the subsidence occurring underneath the interstate highway I-70, the simulated stress and strain field changes on different stages of subsidence. The mechanism of the deformation of the embankment due to subsidence was investigated using the stress and strain contour inside the embankment. The cross section where the maximum settlement happened was selected to analyze the interior stress and strain field.

The vertical stress significantly contributes to the deformation of the embankment during subsidence. The vertical stress field inside the embankment on selected dates are shown in Fig. 6.8. Before subsidence influences the embankment (2019-1-29), the vertical stress increased at deeper regions of the embankment and the variation is uniform. When the embankment is subjected to subsidence, the magnitude of compression (negative) increased at the bottom of the embankment. Besides, the tension (positive) concentrated in the upper layer below the crest where the maximum displacement happens. The compression and tension stress decrease after the embankment settles down. However, some changes still exist compared to the case under gravity (2019-1-29). This indicates that plasticity happens due to subsidence inside the embankment.

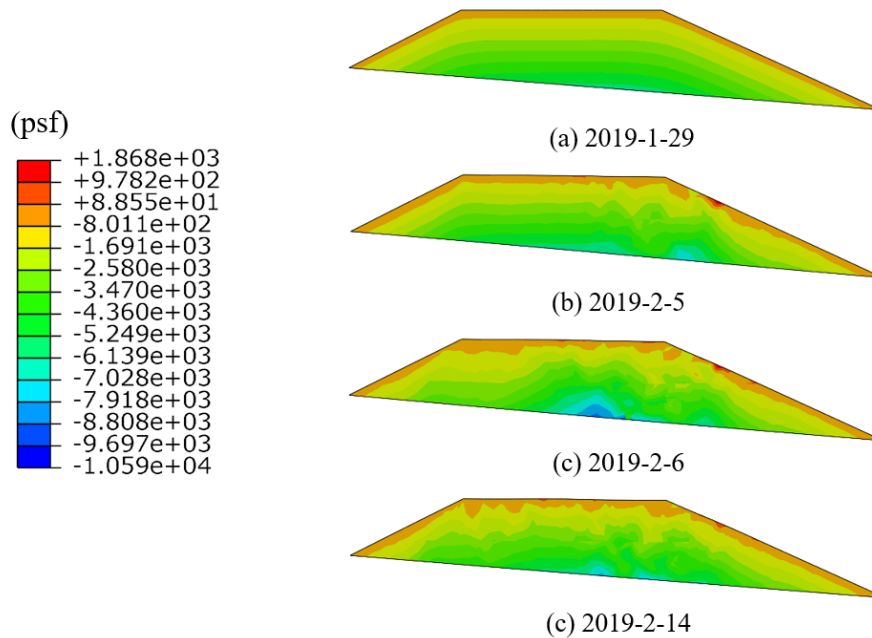


Figure 6.8. Vertical stress inside Embankment #1 at the critical transversal cross section on different stages of subsidence

The principal tensile strain induced during the subsidence influences the interior deformation and evokes the observed settlement on the surface. The mechanism of the settlement can be explored by analyzing the tensile strain that develops inside the embankment. Fig. 6.9 indicates that the principal tensile strain initiates from the bottom of the embankment and penetrates upwards in two branches. One branch propagates to the surface, the other extends toward the south-facing slope. The part of soil on the top of the embankment moves downward between these two tensile strain branches under gravity.

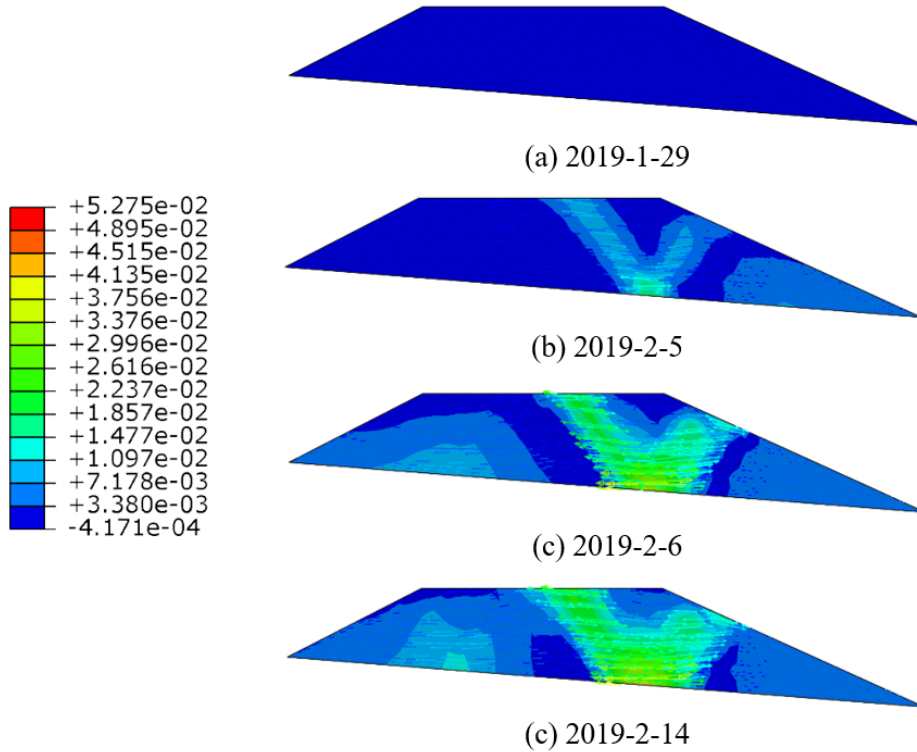


Figure 6.9. Principal tensile strain at the critical transversal cross section of Embankment #1 at different stages of dynamic subsidence

6.3 Slope Stability Analysis

Shear strength reduction method (SRM) was utilized to find the potential critical part in the embankment as well as the factor of safety of the embankment (see Eq. 2.5 and Eq. 2.6). Strength reduction method (SRM) is widely utilized in the slope stability analysis [19][20][21][22][23]. In the SRM, in order to obtain the factor of safety (FS) equivalent to Limit Equilibrium Method (LEM), a strength reduction factor (SRF) was utilized. The factor was employed to reduce the cohesion c and $\tan\phi$ until the slope failed. The original shear strength

parameters are divided with this factor to obtain the reduced shear strength parameters c' and ϕ' as previously described in Chapter 2 in Eq. 2.5 and Eq. 2.6. When applying the SRM in FE analysis, the increasing SRFs are applied successively on the model to reduce the shear strength of the model until the solution runs out of convergence. In ABAQUS, the method is implemented by creating a field value to represent SRF applied on the FEM approach. The field value is set less than one before the SMR step in order to make the slope stable in the gravity and deformation steps. Then in the SMR step, the value increases until the solution goes out of convergence. Previous research found that the shear strength reduction ratio (SRF) when the slope fails is approximately consistent with the factor of safety using LEM. The failure pattern can be traced from the shear strain development.

6.3.1 Potential Critical Cross Section in Embankment #1

Centrifuge tests have indicated that the plastic shear strain zone in unstable slopes coincided with the rupture surface according to Roscoe [58]. We can utilize SRM to make the embankment collapse and identify the critical area with the higher plastic strain. The critical area was utilized to conduct the factor of safety analysis in the next section. The magnitude of the plastic strain in the embankment at the final point of SRM when a complete sliding failure happened is plotted in Fig. 6.10. The contours resulted from four steps of successive subsidence. The critical cross section was located on the south facing slope in the middle of the longitudinal length of the embankment staying at the same location during the successive subsidence.

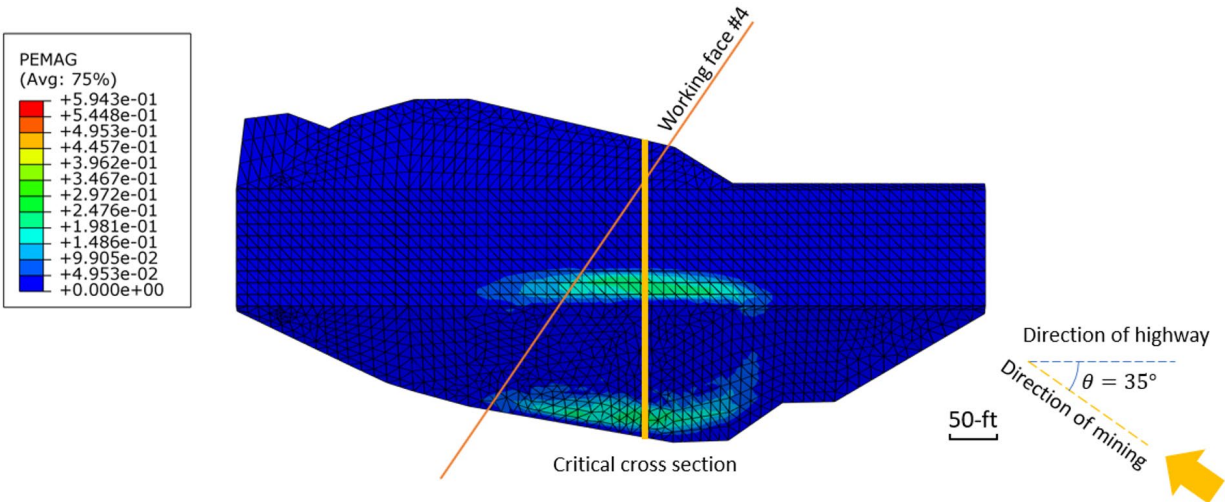


Figure 6.10. Critical cross section for the factor of safety analysis

6.3.2 Factor of Safety of Embankment #1 Impacted by a Successive Subsidence

As discussed above, the FS is obtained using SRM which utilizes the SRF to reduce the cohesion and $\tan\phi$ until the embankment failed. Total displacement is plotted against the SRF to estimate the FS. The knee point, which represents failure of the slope, is found to be equivalent to the FS when using the LEM [23].

Fig. 6.11 shows the process of the determination of the FS of the embankment without subsidence. The plastic strain inside the embankment at the critical cross section with SRF equals to 3.4 is shown in Fig. 6.12. The shear band reaches the top of the embankment and a complete rupture surface is formed when SRF reaches the knee point.

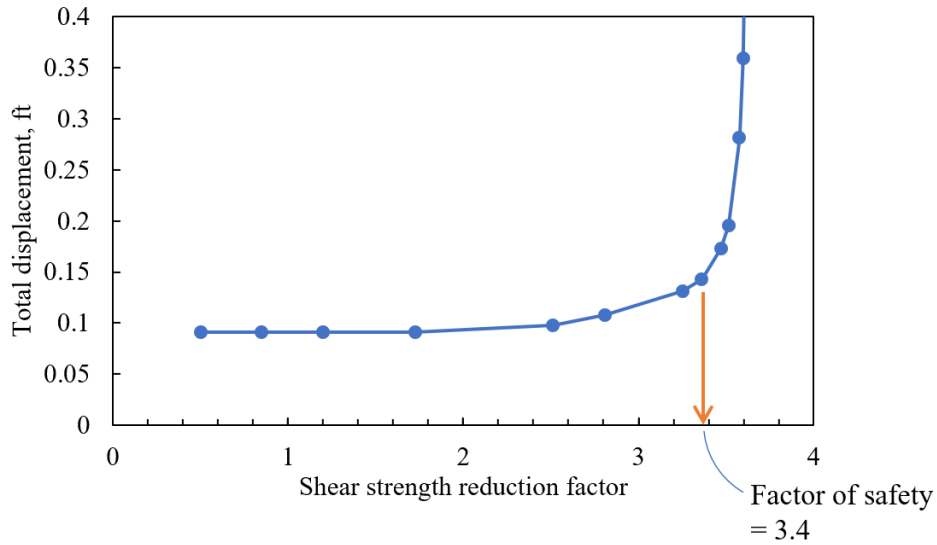


Figure 6.11. Total displacement at the crest of the critical cross section versus the shear strength reduction factor for the case without subsidence

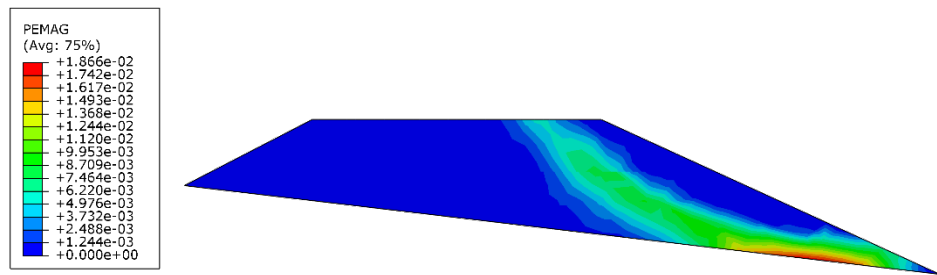


Figure 6.12. Shear band at the critical cross section from SRM

The SRM is validated by comparing the resulted shear band and the factor of safety obtained using SRM to those in SLIDE that utilizes the LEM. In LEM, failure surface is assumed to be a part of circle shown in Fig. 6.13. The shear band in LEM has a very small thickness and will develop as soon as the equilibrium is compromised, which means that failure will occur under small deformations. The factor of safety from SRM is 3.4 that is equivalent to that from LEM. Besides, the location of the shear band in LEM shows good agreement with the center line of the shear band obtained using SRM.

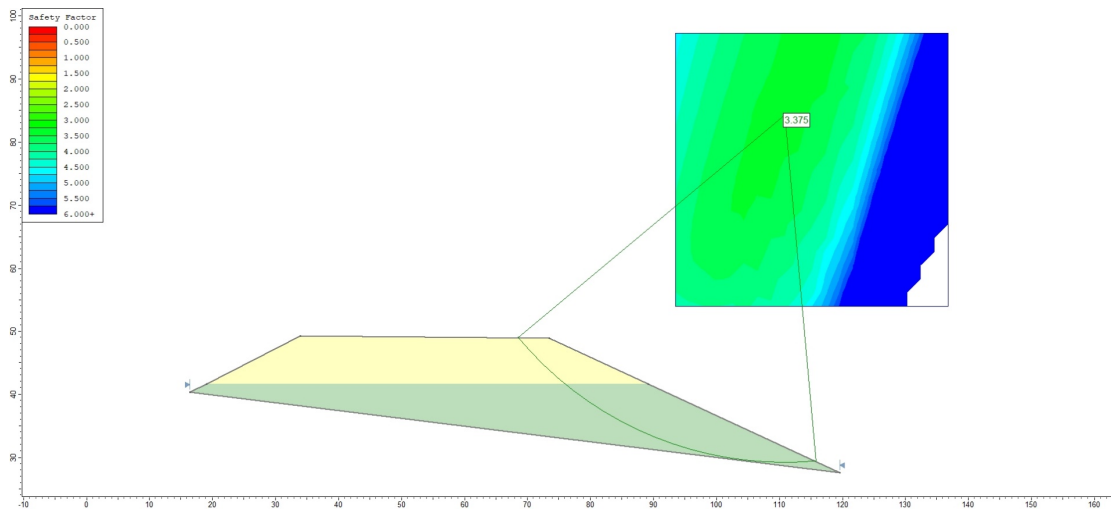


Figure 6.13. Failure surface and the factor of safety calculated by LEM in SLIDE using the same material properties (FS=3.4 in SLIDE)

Then the embankment is subjected to the subsidence and more deformation is observed before the knee point. In this study, a lower and upper bound of the FS is used to better characterize the slope stability of a high embankment during subsidence due to longwall mining. The case when the embankment #1 was subjected to subsidence with the working face position shown in Fig. 6.14 was chosen as an example to explain how the factor of safety is determined.

As shown in Fig. 6.15, before the displacement started to increase exponentially, more deformation is observed compared to the case without subsidence (Fig. 6.11). The single point of the factor of safety does not take the initial deformation into consideration. Such initial sliding-formed deformations will change the geometry of the embankment especially on the top and is crucial for its use as an interstate highway. In the field, the embankment is stable but shows noticeable deformations according to the field measurement. In this study, the lower bound and the upper bound of the factor of safety are introduced to better describe the stability of a highway embankment during undermining. The lower bond of the factor of safety is located at the point of

the FS plot where the embankment begins to move. It can be utilized to identify if the embankment will show noticeable deformations on the top. The higher bond, which is the traditional factor of safety, helps determine if the embankment is stable.

The lower bound of the factor of safety was found to be 1.1. Before this point, the displacement increased at a rather low rate and the plot is almost horizontal. After this point, the embankment begins to noticeably deform. And the lower bond factor of safety is a little bit larger than one, which means that the sliding formed displacement will happen in the embankment, which is consistent with the field measurement from the slope stake surveys and inclinometers. The upper bond factor of safety is found to be located at 3.4, where the total displacement starts to increase exponentially on the crest and the shear band develops. In this way, the factor of safety together with the lower bound factor of safety better described the stability and behavior of the highway embankment when subjected to subsidence.

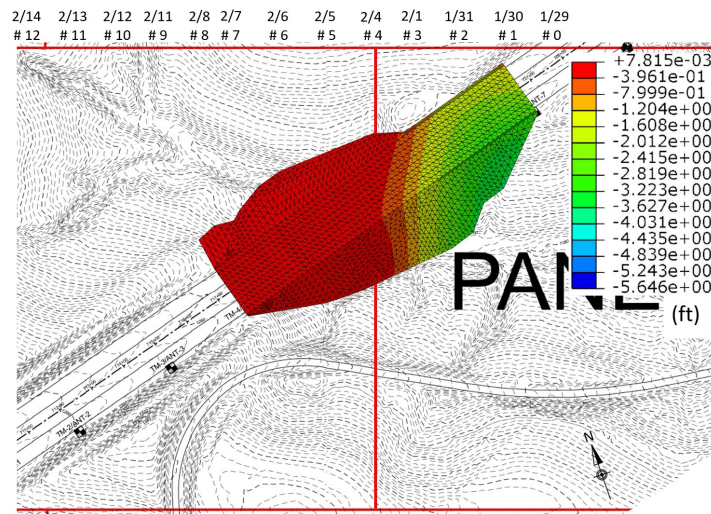


Figure 6.14. Embankment #1 subjected to subsidence #4

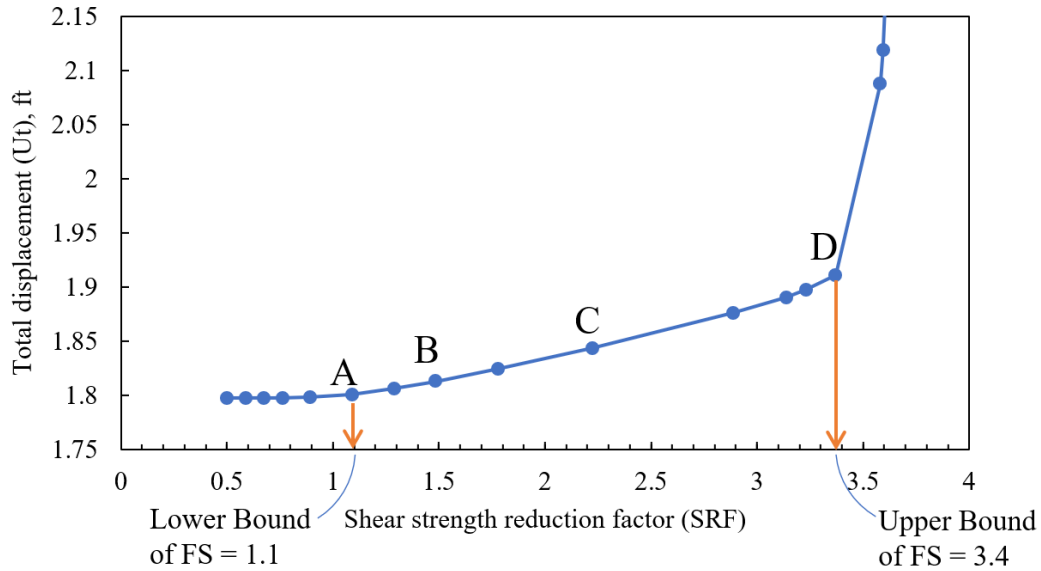


Figure 6.15. Total displacement at the crest of the critical cross section versus the shear strength reduction factor for the case of working face position #4

The plastic strain as well as the horizontal displacement at four points of shear strength reduction factor (SRF) are plotted in Fig. 6.16 and 6.17, respectively. At the lower bound of the factor safety, where the plastic strain initiates, small deformation occurs on the crest. The plastic strain starts to initiate but the shear band is not formed yet. Point D is the upper bound of the factor of safety when the shear band completely develops and the slope becomes unstable.

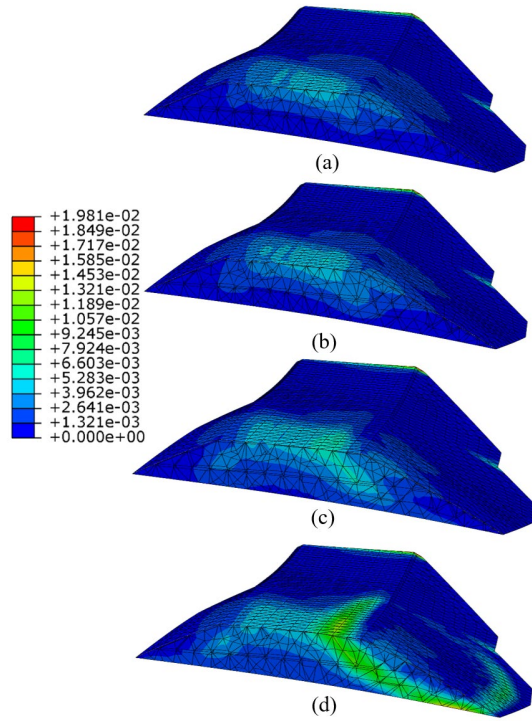


Figure 6.16. Plastic strain at the critical cross section with SRF equals to (a)1.1 ;(b)1.5 ;(c)2.2 and (d)3.4

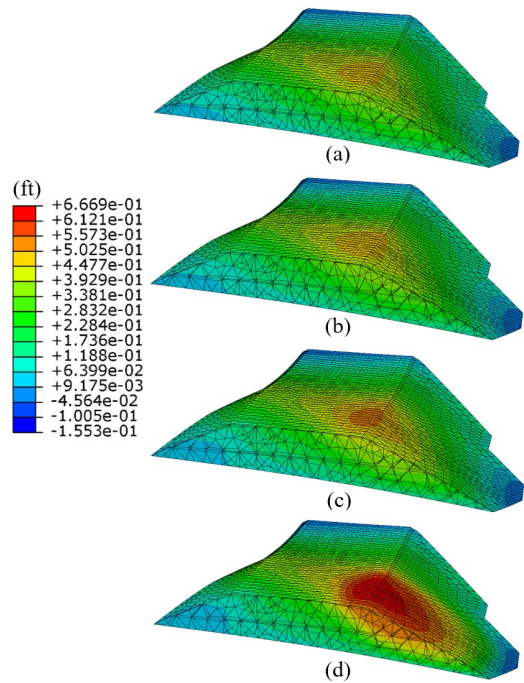


Figure 6.17. Horizontal displacement perpendicular to the highway direction at the critical cross section with SRF equals to (a)1.1 ;(b)1.5 ;(c)2.2 and (d)3.4

The lower bound of the factor of safety is close to the true factor of safety when there is no subsidence. However, when the embankment is subjected to subsidence and displacements, it is far away from the true factor of safety. In other words, the embankment is still safe even though there are already some limited plastic strains in the slope. Generally, the factor of safety for small displacements in a slope is calculated using Eq. 6.1.

$$FS = \frac{c + (\sigma_n - u)\tan\phi}{\tau} \quad (6.1)$$

where c is the cohesion, ϕ is the friction angle, σ_n is the normal stress generated by gravity, u is the water pressure generated by the ground water table and τ is the shear stress induced by gravity.

For the case when the embankment is experiencing large subsidence-induced deformations, the relevant factor of safety is different than that given by Eq. 6.1. According to Johnson [43], the factor of safety of a slope experiencing large deformations (usually concentrated in a shear band) is given in Eq. 6.2.

$$FS = \frac{c + (\sigma_n - u)\tan\phi + \eta\left(\frac{dv}{dy}\right)}{\tau} \quad (6.2)$$

where η is the viscosity of soil, $\frac{dv}{dy}$ is the change of velocity with depth in the shear band and τ is the shear stress induced by gravity. From the equation, the factor of safety increases in value when the third term in the numerator of the equation is mobilized at large deformations. That is why the embankment did not fail when large deformations were in effect. The shear strength of soil will increase once the embankment shows deformations. For an embankment subjected to subsidence, the moving ground causes displacements in the embankment. During these displacements, the shear strength mobilized in the embankment soil is given by the numerator of Eq. 6.2. Thus, the shear strength of the soil is increased by the mobilization of the viscosity of the

soil. Consequently, with displacement the embankment becomes stronger and safer with respect to any slope instability. Field behavior of the embankment proved this to be the case. As analyzed above, the initial shear displacement started at the crest and propagated toward the toe of the slope (Fig. 6.17). This is reflected in the factor of safety plot shown in Fig. 6.15. The lower bound of the FS was small and applied when the plastic strains in the slope were small Fig 6.16 (a). The upper bound of the FS was larger when the plastic strains covered the whole slope Fig. 6.16 (d). The shear strains formed a thick shear band in which the cohesion, friction and viscosity were mobilized Eq. 6.2.

Another way to approach the stability analysis of Embankment #1 is considering the influence of the rock fragments in the shear strength of the soil forming part of the embankment. This influence will also affect the FS. According to Vallejo et al. [44] and Vallejo and Lobo-Guerrero [45], the FS for a slope made of soil-rock mixtures can be obtained from the following equation,

$$FS = \frac{[c + (\sigma_n - u) \tan \phi][1 + 2.5 C]}{\tau} \quad (6.3)$$

The percentage of rock fragments by volume, C , varies in the soil forming part of Embankment #1 from 2% to 23% (Table 3.2). For the stability analysis an average value of C equal to 12% was chosen. With this value of C , the shear strength of the soil matrix (given by the parameters in the first parenthesis of Eq. 6.3 will be increased by a factor equal 1.3. The stability analysis of Embankment #1 was carried out using this increment value. Using the approach depicted by Eq. 6.2 is not easy to calculate the FS because the determination of the viscosity of the solid mass of soil forming part of the numerator of Eq. 6.2 is very difficult to obtain.

The same procedure was conducted to determine the factor safety range of Embankment #1 when subjected to subsidence with the working face at different locations. The variation of the

factor of safety with different positions of working face was shown in Fig. 6.18. For the critical section shown as working face position #6 in Fig. 6.18, when the orientation is 35-degree, overburden is 675-ft, the critical FS range has a lower bound equal to 1.1, and an upper bound equal to 3.2.

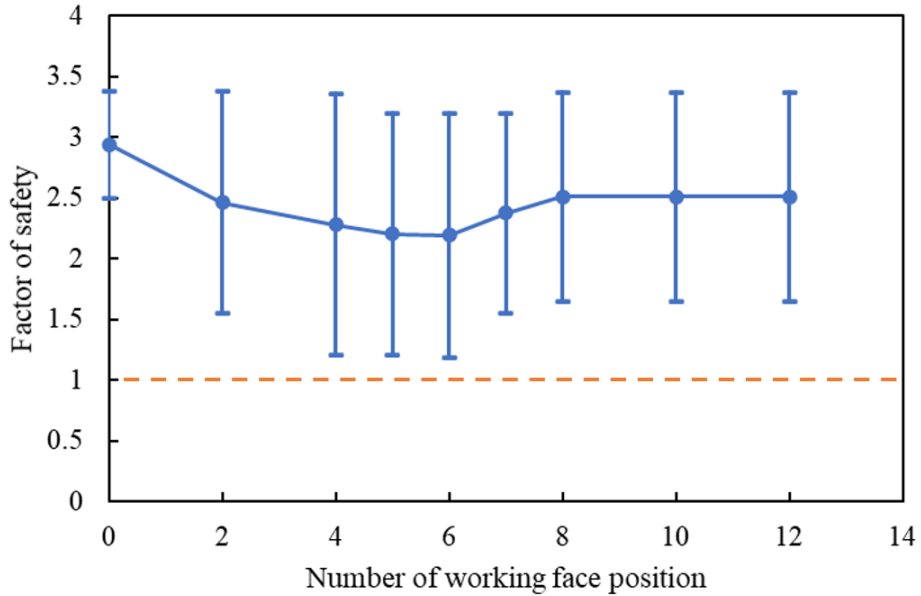


Figure 6.18. Plot of factor of safety versus the number of working face position when the orientation of highway is 35-degree with respect to the direction of mining and the overburden is 675-ft

6.4 Sensitivity Tests on the Shear Strength Parameters of Soil and Ground Water Table that Influence the Maximum Subsidence of Embankment #1

Triaxial compression tests were conducted on the soil samples located in the upper layer of the embankment with a lower rock ratio. For the soil in the upper layer with a higher rock ratio, the friction angle was determined from previous research on the shear strength of sand-clayey gravels. The cohesion is increased in the upper layer considering the viscosity during the subsidence. The sensitivity tests on the shear parameters of soil were analyzed in this chapter to calibrate the model to the field measurement. Five cases were analyzed with different values of shear parameters. Furthermore, the effect of ground water was analyzed in the two critical cross sections showing that the variation of ground water table has limit influence on the behavior of the embankment during the subsidence.

6.4.1 Sensitivity Tests on the Shear Parameters

Sensitivity tests with respect to the shear parameters including the friction angle and the cohesion were analyzed in this section. The Finite Element model was used in this process. The basic criterion for the validation of the FE analysis includes the calculation of the value of maximum subsidence and its location and their comparison with the same values measured in the field. The factor of safety was also calculated in these numerical models. Five cases were selected with different combinations of friction angle and cohesion for the FEM. The shear parameters of these five cases are summarized in Table 6.1 as well as the resulted maximum subsidence.

Table 6.1. Shear Parameters in Five cases with resulted maximum subsidence

Case #	Upper Layer		Lower Layer		Maximum Subsidence, ft
	friction angle	c,psf	friction angle	c,psf	
0	41°	770	40°	780	5.9
1	41°	775	40°	785	5.8
2	42°	775	40°	785	5.6
3	42°	780	41	785	5.5
4	42°	775	42°	785	5.5

The friction angle was set to be 41-42 degree for the upper layer due to a rock concentration ratio by weight equal to 50% obtained from the laboratory tests. Three friction angles, 40, 41, and 42-degree were tested for the lower layer considering the increase of the rock concentration ratio during the consolidation due to subsidence observed from the field measurement. The cohesion was selected by considering the direct shear test. The cohesion is increased considering the viscosity effects during the subsidence.

The field measurement of the vertical subsidence shown in Fig. 6.19. The final vertical subsidence contour in these four cases are shown in Fig. 6.21. The selected Case #2 was shown in Fig. 6.20. It is indicated that Case #2 provides the accurate maximum subsidence and its location. The value of these parameters given by the FEM is very close to the ones given by the field measurements. Besides, the shape of the secondary maximum subsidence shows good agreement with the field's subsidence contour (Figs. 6.19 and 6.20).

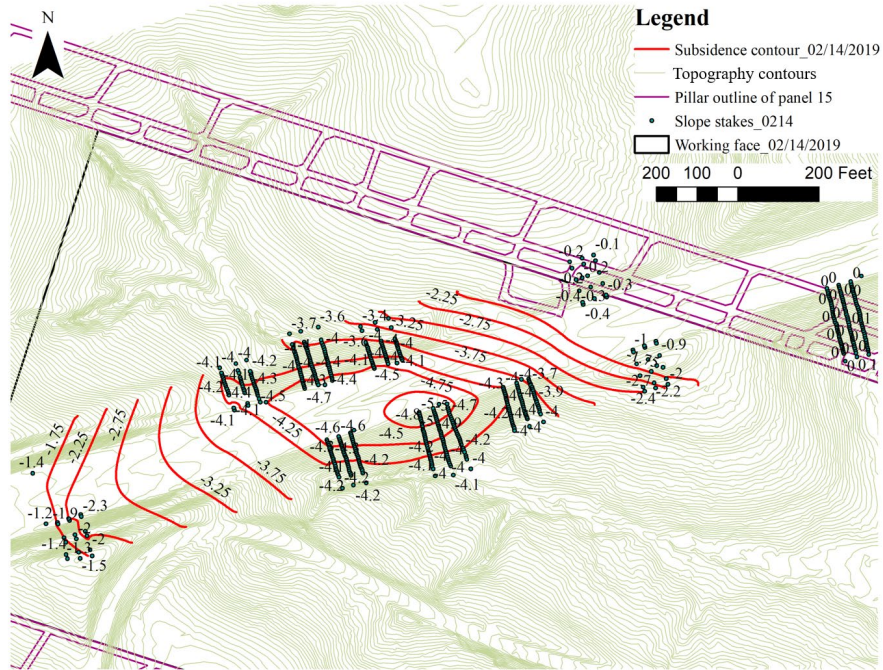


Figure 6.19. Subsidence contour of Embankment #1 generated using the field measurement from the slope stake surveys

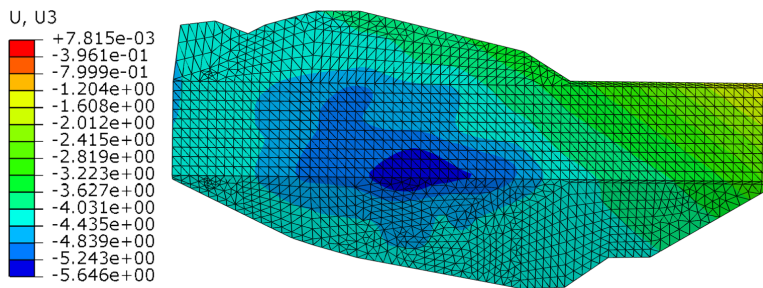
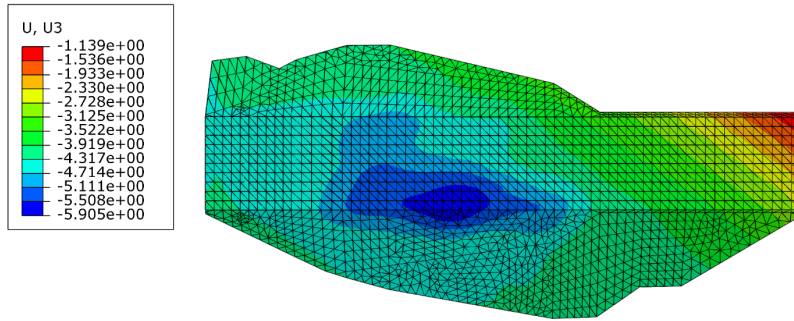
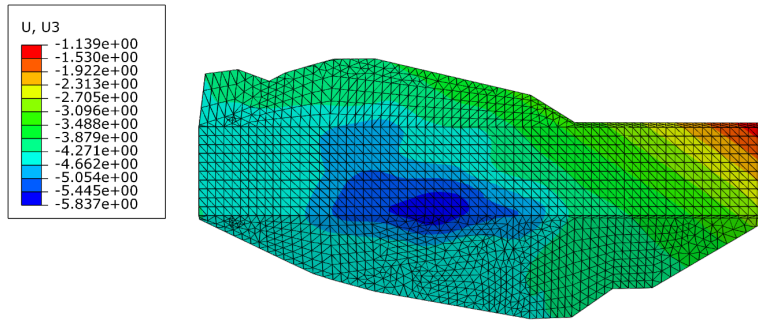


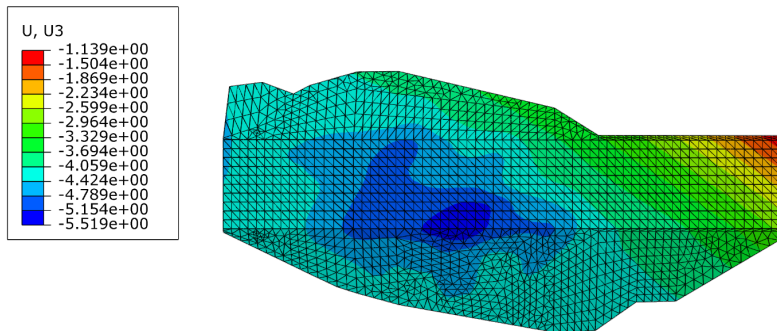
Figure 6.20. Final simulated vertical subsidence contours on Embankment #1 in Case #2 (units:ft)



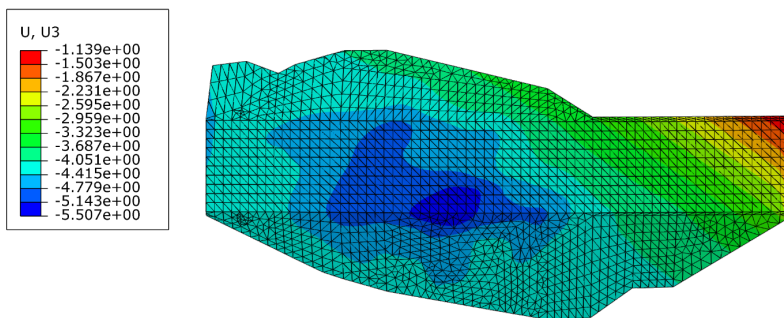
(a)



(b)



(c)



(d)

Figure 6.21. Final simulated vertical subsidence contours on Embankment #1 in Case # (a) 0;(b) 1;(c) 3;(d) 4 (units:ft)

6.4.2 Effects of the Ground Water Table on the Behaviors of the Embankment at the Critical Cross Section

The water pressure in the soil is an important factor that might have a significant influence on the stability of the embankment. As the ground water table rises in the embankment, the increasing water content will definitely increase the density of the saturated soil resulting in an increase of gravity force which is the main driven force causing sliding. Besides, the pore water pressure will become positive below the phreatic surface, which will produce an effective normal stress and a decrease in shear strength of the soil. Piezometer measurement introduced in the previous chapters has indicated the variation of the ground water table in the embankment, which directly influences the water content and water pressure in the soil and consequently affect the slope stability of the embankment. The piezometers are only located in two cross sections. At cross section 720+00, the water table is below the embankment according to the piezometer. The cross section 720+50 with a lower altitude and an inclined bottom line is analyzed to investigate the influence of the variation of the ground water table on the slope stability of the embankment under gravity.

The water table at this cross section varied from 1192.4-ft to 1197.3-ft. The elevation of the lower toe is 1190-ft. Besides, looking through the previous readings of the piezometer data at TB-7, the highest record was 1204-ft on the date of 02/09/2017. From the boring log provided from PennDOT, the water level was 1208-ft at TB-7 which was recorded 17 hours after the installation of the boring hole was finished.

The resulted phreatic surface was shown in Fig. 6.22. The elevation of the phreatic surface in the location of TB-7 at cross section 720+50 in Embankment #1 was 1204-ft (from piezometer data in Feb, 2017) and 1208-ft (from piezometer data recorded after installation of the boring hole).

Below the phreatic surface, the soil is saturated and the pore water pressure turns out to be positive. From the contour, the phreatic surface did not go straight to the toe forming a discharge zone, which corresponded to the field observation that the water came out of the slope.

However, this resulted discharge zone is much smaller than that observed in field. According to the field observation on December 17, 2018, the distance from the top of the saturated zone to the lower toe is around 50-ft with a vertical distance of 18-ft. Hence, another model was constructed by defining the saturated zone on the slope corresponding to the field observation. Based on this boundary condition, FEM calculated the resulted water level at TB-7 as 1206.3-ft shown in Fig. 6.23, which is in the range of the piezometer data at the installation of the boring hole.

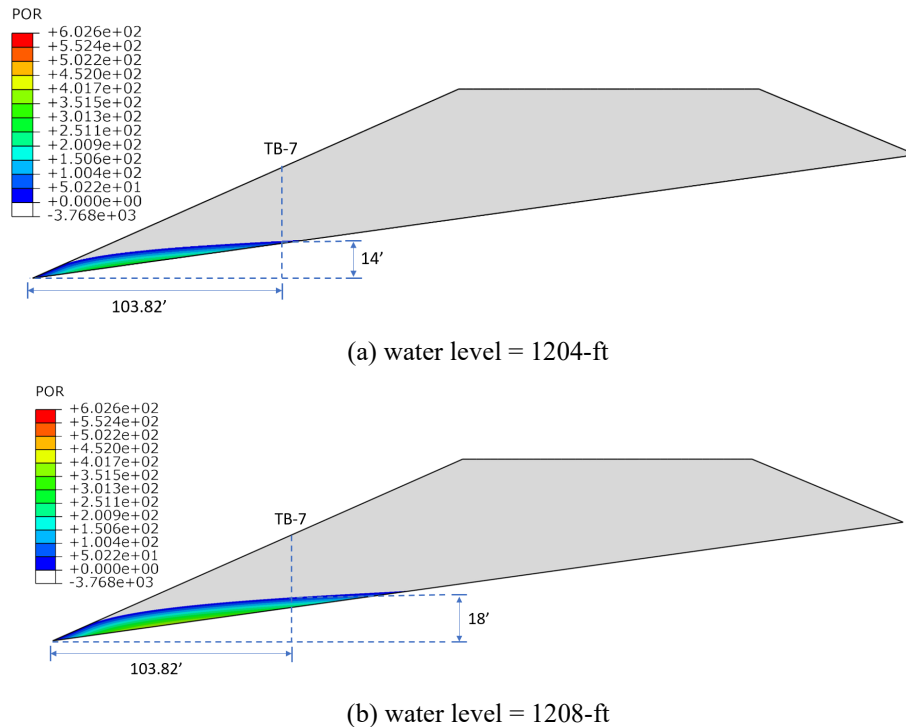


Figure 6.22. Two elevations of the phreatic surface at TB-7 indicated by pore water pressures (units:psf)

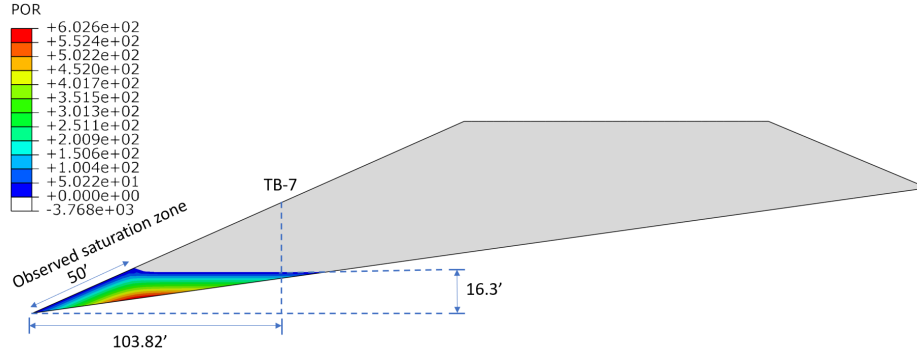
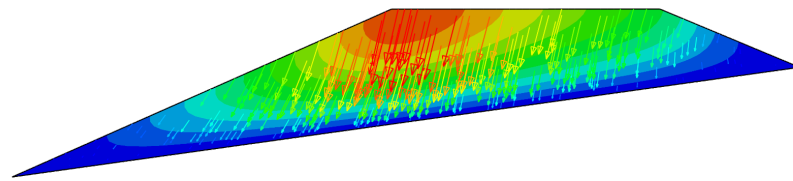
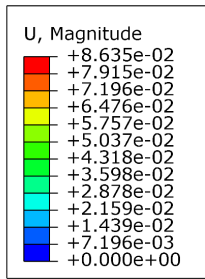
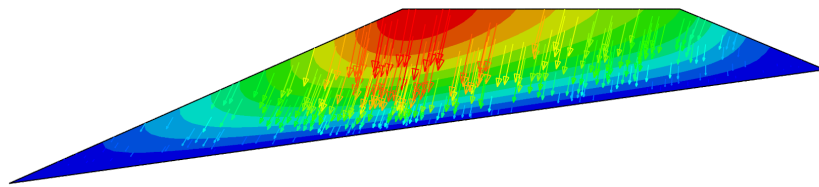
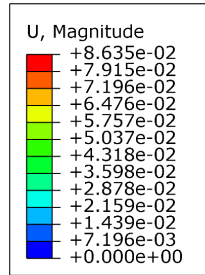


Figure 6.23. The elevation of the phreatic surface indicated by the positive pore water pressure resulted from the observed saturation zone (units: psf)

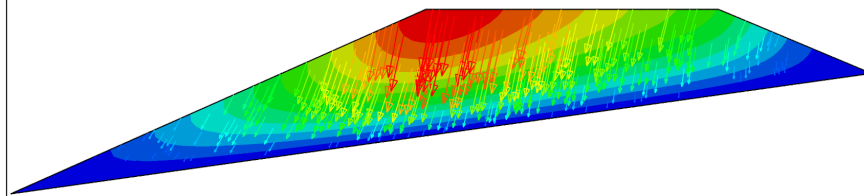
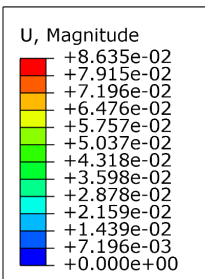
Fig. 6.24 indicated the total displacement at cross section 720+50 with different elevations of the water table. The magnitudes of the total displacement under these four conditions were plotted against the vertical distance between the phreatic surface and the lower toe of the slope in Fig. 6.25. The slope with water presented a 7.6% higher displacement at the crest than that without water.



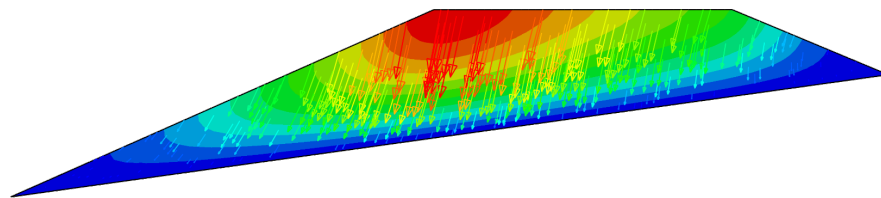
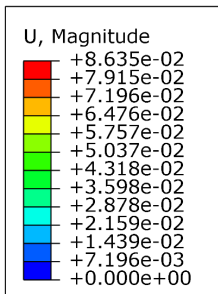
(a) no water



(b) 1204-ft



(c) 1208-ft



(d) 1206-ft resulted from field saturated zone

Figure 6.24. Total displacement in the Embankment #1 at cross section 720+50 with (a) no water and with phreatic surface at an elevation of (b) 1204-ft; (c) 1208-ft and (d) 1206-ft with field saturated zone (units: ft)

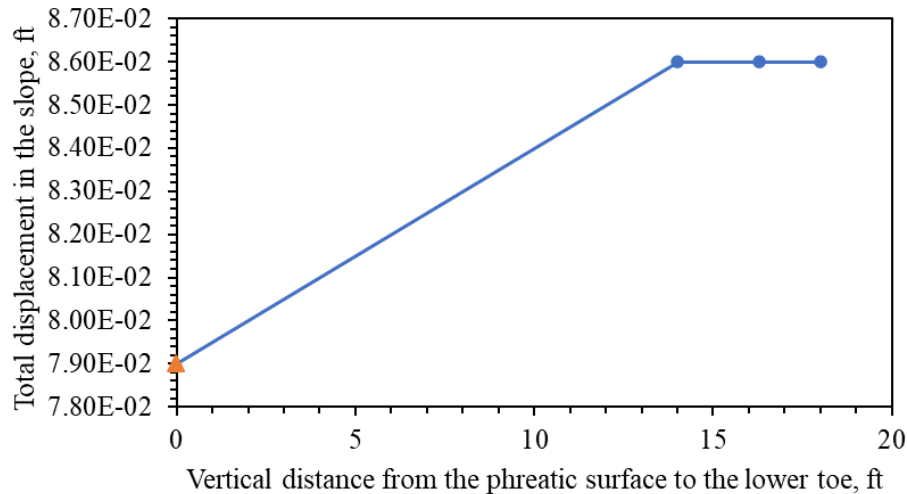


Figure 6.25. Total displacement versus the vertical distance between the phreatic surface and the lower toe

The determination of the factor of safety in four different conditions of water content was summarized in Fig. 6.26. The total displacement was plotted against the strength reduction factor in this process. The field value at the inflection point represented the factor of safety. The resulted factor of safety was plotted versus the vertical distance between the phreatic surface and the lower toe in Fig. 6.27. The factor of safety was the lower when there was water compared to the dry conditions, but still above one, indicating that the embankment was safe. However, the increase of the water level contributed to the decrease of the factor of safety. When the water level increased from 1204-ft to 1208-ft, factor of safety decreased a little bit from 2.3 to 2.16.

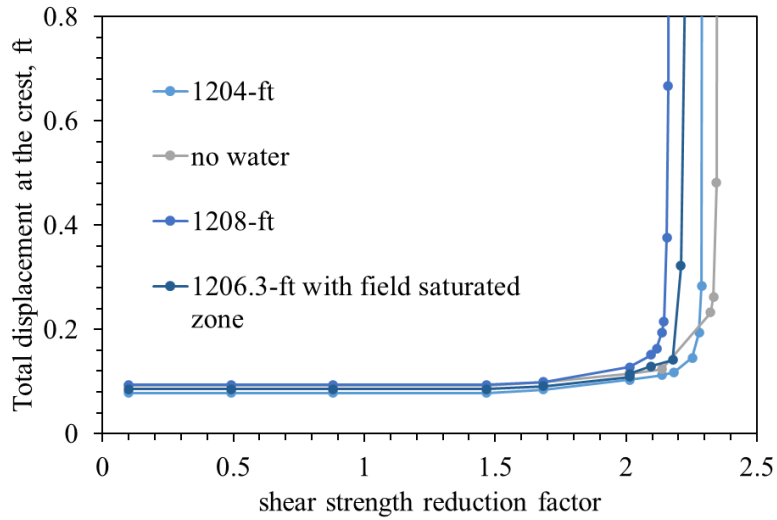


Figure 6.26. Determination of the factor of safety by plotting the total displacement at the crest versus the shear strength reduction factor

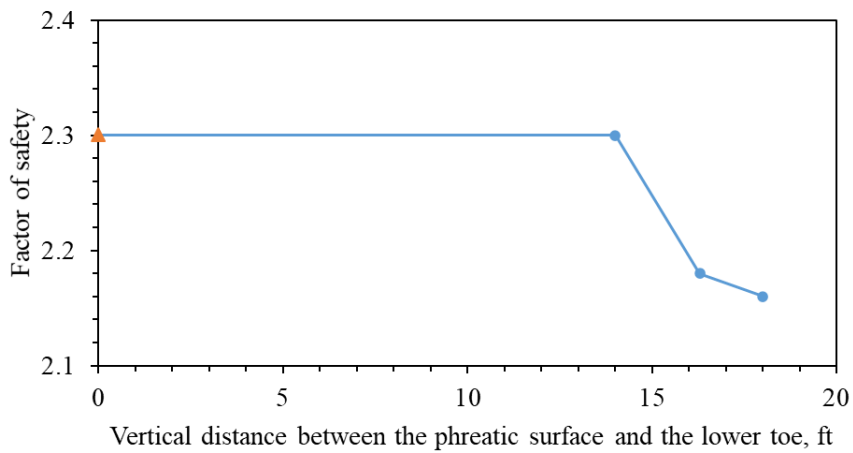


Figure 6.27. Factor of safety of Embankment #1 at cross section 720+50 with different ground water tables before subsidence

7.0 Parametric Study

Analysis of the changes in deformation and stability of Embankment #1 in function of the direction of longwall mining and level of overburden was conducted using a numerical analysis that uses the FEM. Deformation and the stability of Embankment #1 was analyzed using three different angles between the long axis of the embankment (same as direction of highway I-70) and the direction of longwall mining. These angles were equal to, 0, 35, and 90-degree. For the 35-degree and 90-degree cases, four overburdens, 400-ft, 500-ft, 600-ft, and 675-ft were used in order to investigate the influence of the overburden on the deformations and stability of the embankment. For the complete analysis, a total of 12 cases with different orientations and overburdens were used. It was determined that the embankment remained safe when subjected to a longwall mining subsidence. However, significant deformations will occur in the embankment at certain cases of longwall mining orientations and levels of overburden. These significant embankment deformations can affect highway structures on the embankment (i.e. pavement).

7.1 Three-Dimensional Analysis of Embankment #1 with respect to the Longwall Mining Orientation

The highway Embankment #1 was assumed to be subjected to the longwall mining subsidence at three angles, 0, 35, and 90-degree shown in Figure 3.1 to analyze the influence of orientation of highway on the behavior of embankment. The deformation and the slope stability of the Embankment #1 were analyzed for these three cases. It should be noticed that the overburden

for this analysis is set to be constant with a value of 675-ft. The factor of safety for other cases are summarized later in this study.

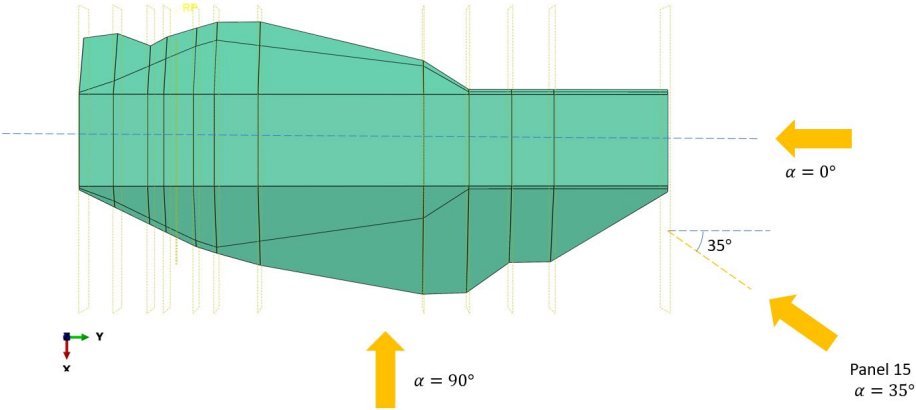


Figure 7.1. Three angles between the direction of highway and the direction of mining

7.1.1 Deformation analysis

This section will compare the maximum vertical subsidence in the embankment when the angles between the highway and the mining are 0-degree and 35-degree with a constant overburden of 675-ft. The vertical displacement contour from the FEM is shown in Fig. 7.2. When the orientation increases from 0-degree to 35-degree, the maximum subsidence increases a little bit from 5.31-ft to 5.34-ft. The deformation analysis for 90-degree is not compared here for the reason that the embankment failed in the case of 90-degree and the analysis aborted. SRM was utilized to generate the deformation for the case of 90-degree to show the deformation in the embankment when the direction of mining is perpendicular to the highway.

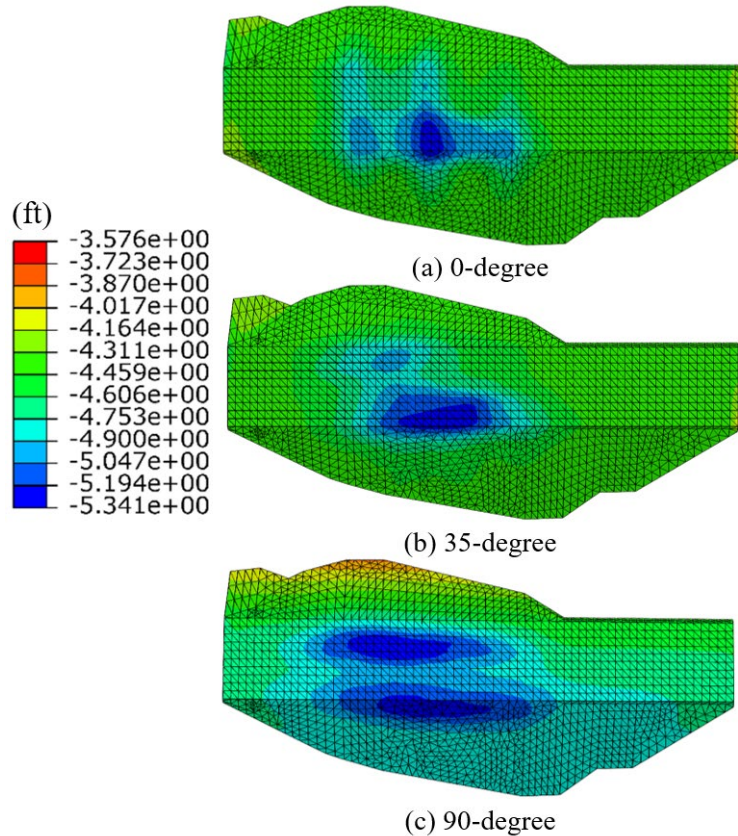


Figure 7.2. The vertical subsidence on Embankment #1 when the angle between the orientation of highway and mining is (a) 0-degree; (b) 35-degree and (c) 90-degree (units:ft)

7.1.2 Slope stability analysis

Plastic strain which represents the failure was plotted at each case of the orientations at the critical cross sections in Embankment #1 shown in Fig. 7.3. The shear strength reduction factors were set to be equal to one. Higher plastic strains develop on the top of the embankment when the direction of the longwall mining is at 0-degrees with respect to the long axis of the embankment (direction of the highway). When the direction of mining is inclined at 35-degrees with respect to the long axis of the embankment, large plastic strains exist on the bottom of the embankment. For

the case of 90-degree direction, larger plastic strain developed inside the embankment, which contributes to the local deformations and failure in the embankment. These large strains developed in the FEM stability of the embankment causes the model to stop its calculations. The analysis cannot be kept running in the normal way unless the SRM is applied.

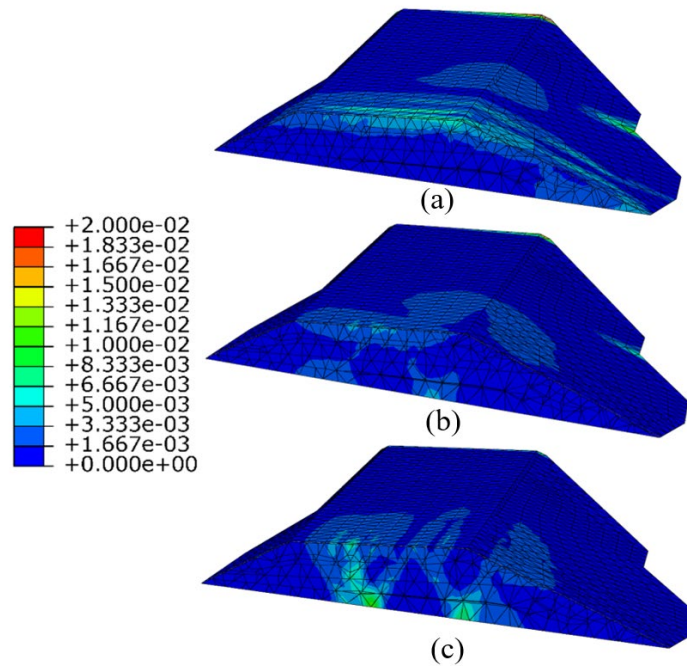


Figure 7.3. Plastic strain at the critical cross section of Embankment #1 when the angle between the orientation of highway and mining is (a) 0-degree; (b) 35-degree; and (c) 90-degree with SRF equals to one

Factor of safety in each case of orientation was obtained using shear strength reduction method (SRM) as illustrated in the previous sections. The ranges of the final factor of safety with respect to different orientations of longwall are shown in Fig. 7.4. The factor of safety decreases in value as the direction of mining with respect to the embankment increases in value. For 90-degree case, the lower bound of the factor of safety was less than one, which is consistent with

the large amount of plastic strain inside the embankment. The embankment will experience large deformation in this case.

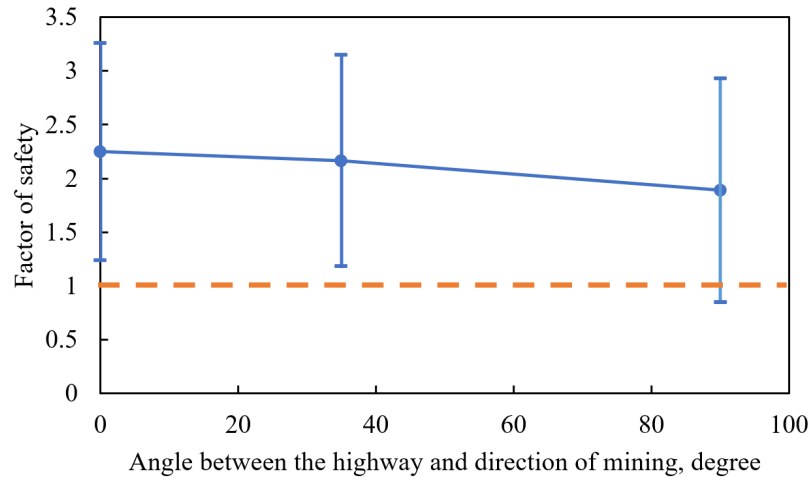


Figure 7.4. Factor of safety for Embankment #1 at different angles with respect to the mining direction

The failure mechanism for the 90-degrees case is shown in Fig. 7.5. Shear band did not form at the SRF of equal to 1 and the embankment did not experience large deformations. However, local parts of the embankment are creeping in the center of two large zones of plastic strain, which will induced settlement of the highway embankment. Some lateral spreading was also observed on the side of the red arrows, forming a bulge on the adjacent slope.

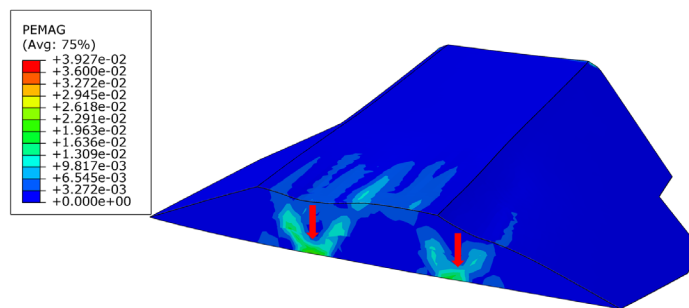


Figure 7.5. Plastic strain and deformations inside Embankment #1 when subjected to longwall mining at an angle of 90-degree

7.2 Three-Dimensional Analysis of Embankment #1 with Different Overburden Thickness

Embankment #1 was subjected to longwall mining subsidence with different overburden values that included 400-ft, 500-ft, 600-ft and 675-ft. The vertical subsidence on the embankment changed depending on the overburden values. Also, the slope stability analysis was conducted and the factor of safety was calculated using SRM for each case of the overburden values.

7.2.1 Deformation Analysis

Deformation analysis was conducted based on the longwall mining orientation of 35-degrees. The vertical subsidence on the embankment is plotted in Fig. 7.6 considering different overburden values. This figure shows that the magnitude of the maximum vertical subsidence decreases as the overburden value increases.

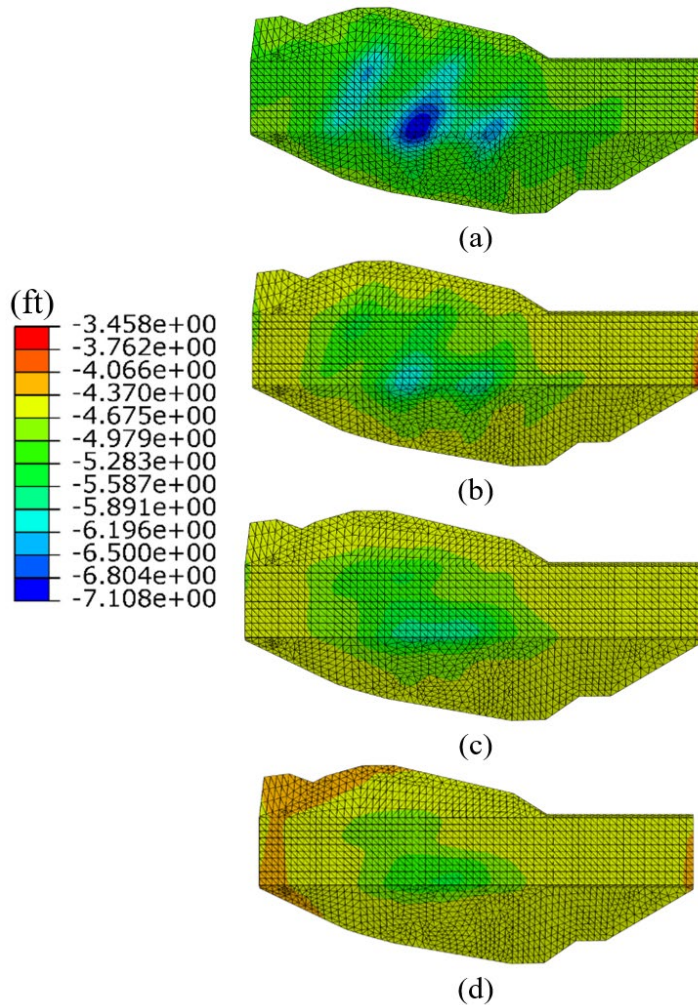


Figure 7.6. Final vertical subsidence on Embankment #1 subjected to longwall mining with different overburdens (units: ft)

The movement on the ground below the embankment was different for different overburden values as shown in Fig. 7.7. The maximum subsidence increases as the overburden decreases in value. Also, the slope of the subsidence contour increases as the overburden decreases in value. The ground movement, the total subsidence on the embankment, and the settlement of the embankment are summarized in Table 7.1. The subsidence of the embankment itself was calculated by subtracting the ground subsidence from the total subsidence. The embankment subsidence, that is, the settlement in the embankment was plotted against the overburden values.

This plot is shown in Fig. 7.8. It was determined that the settlement of the embankment decreases as the overburden increases.

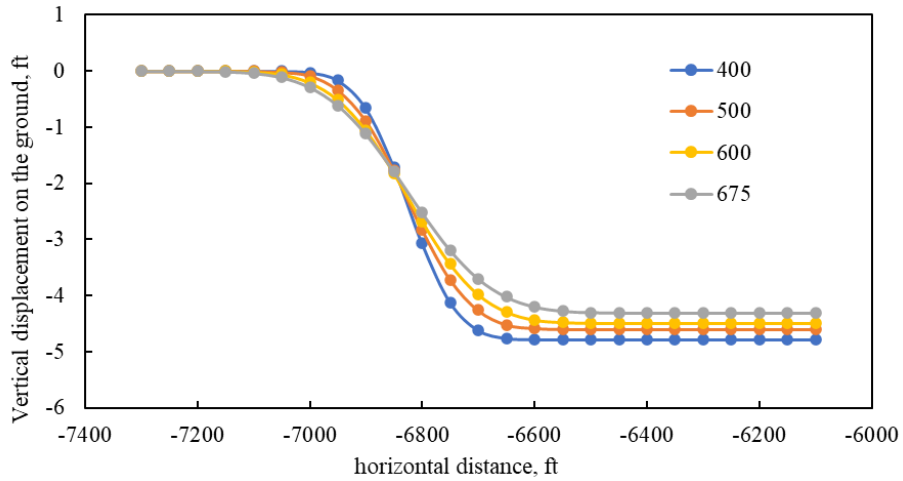


Figure 7.7. Influence of overburden on the subsidence on the ground

Table 7.1. Calculation of the settlements in the embankment with different overburdens

Overburden, ft	ground subsidence, ft	Total subsidence, ft	Settlement, ft
675.00	4.31	5.34	1.03
600.00	4.50	5.81	1.31
500.00	4.60	6.09	1.49
400.00	4.79	7.11	2.32

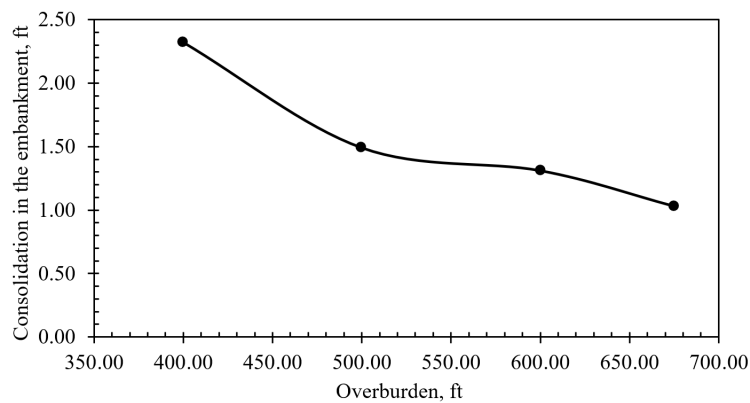


Figure 7.8. Variation of the settlement in the embankment with different overburdens

7.2.2 Slope Stability Analysis

Four overburden levels were considered to explore their influence on the slope stability of a highway embankment. The analysis was conducted when the longwall mining is at an angle of 35-degree and 90-degree with respect to Highway I-70 (or long axis of the embankment). A detailed analysis of the 0 degrees case was not carried out. The reason being, that this orientation was considered to be non-critical for the stability of the embankment.

7.2.2.1 Embankment #1 Subjected to Longwall Mining at an Orientation of 35-Degree with respect to the Highway

The slope stability analysis was conducted on Embankment #1 when it is subjected to longwall mining at an angle of 35-degrees. Plastic strains inside the embankment for different overburden levels and an SRF equal to one are shown in Fig. 7.9. This figure shows that a larger overburden generates lower plastic strain inside the embankment. Also, for the case of a 400-ft of overburden, the plastic strain develops from the bottom of the embankment and continues toward its top. As a result, the parts of the embankment that develop these plastic strain zones will experience settlement as shown in the deformation analysis.

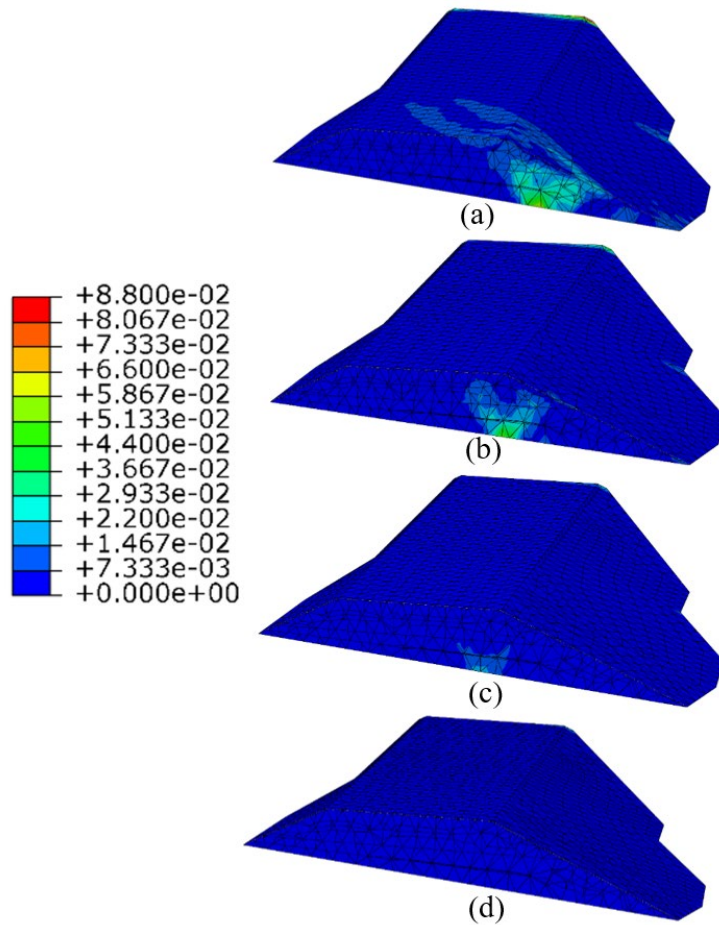


Figure 7.9. Plastic strain inside Embankment #1 due to longwall mining with different overburdens of (a) 400-ft; (b)500-ft; (c)600-ft; (d)675-ft at an angle of 35-degree with respect to the highway

The resulted factor of safety range for these four cases of overburdens were plotted in Fig. 7.10. The factor of safety increases as the overburden increases in this case of 35-degree. For case of 500-ft and 400-ft, the lower bond of the factor of safety is above and below one, respectively. The plastic strain in the embankment for the case of 400-ft almost penetrates the embankment. While for the case of 500-ft, the plastic strain only exists on the bottom. The difference in the distribution of the plastic strain is consistent with the difference in the factor of safety.

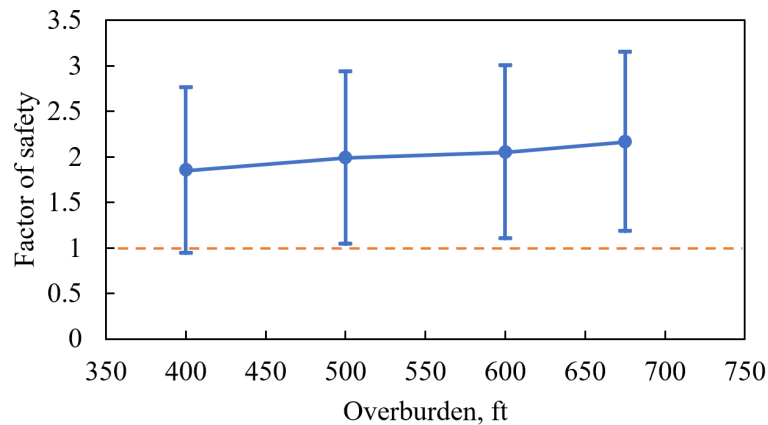
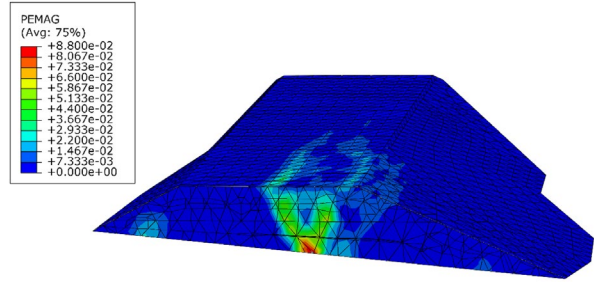


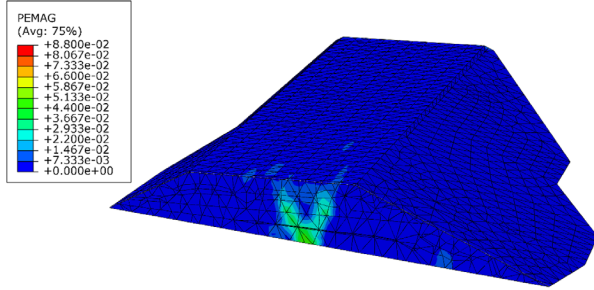
Figure 7.10. Influence of overburdens on the factor of safety of Embankment #1 at the orientation of 35-degree with respect to the longwall mining

7.2.2.2 Embankment #1 Subjected to Longwall Mining at an Orientation of 90-Degree with respect to the Highway

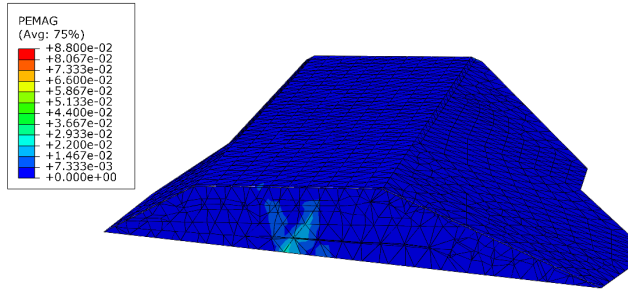
The slope stability analysis was conducted on Embankment #1 when it is subjected to a longwall mining at an angle of 90-degree. Plastic strain inside the embankment was plotted with different overburdens in Fig. 7.11. A larger overburden generates lower plastic strain inside the embankment. All cases present plastic strain inside the embankment. The plastic strain in the case of 675-ft is not clear due to the identical legend for comparison. It actually penetrated to the top and the corresponding part will creep until the embankment failed.



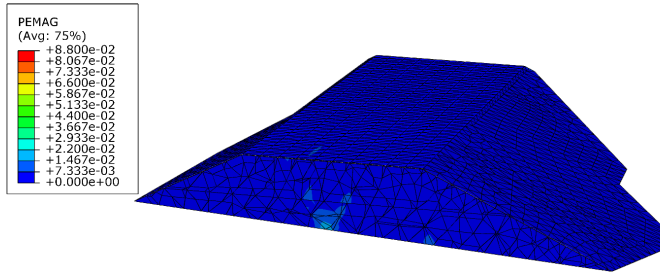
(a)



(b)



(c)



(d)

Figure 7.11. Plastic strain inside Embankment #1 due to longwall mining with different overburdens of (a) 400-ft; (b)500-ft; (c)600-ft; (d)675-ft at an angle of 90-degree with respect to the highway

The resulting factor of safety for these four cases of overburden levels are plotted in Fig. 7.10. This figure shows that the factor of safety increases as the overburden increases. For cases

of 500-ft and 400-ft of overburden, the lower bound of the factor of safety is much lower than one. For cases of 600-ft and 675-ft of overburden, the lower bound of the factor of safety is a little bit lower than one. The plastic strain in the embankment for the cases of 400-ft and 500-ft of overburden almost completely covers the whole embankment. While for the cases of 600-ft and 675-ft, of overburden the plastic strain only develops at the bottom (Fig. 7.9). The differences in the distribution of the plastic strain is consistent with the differences in the factor of safety.

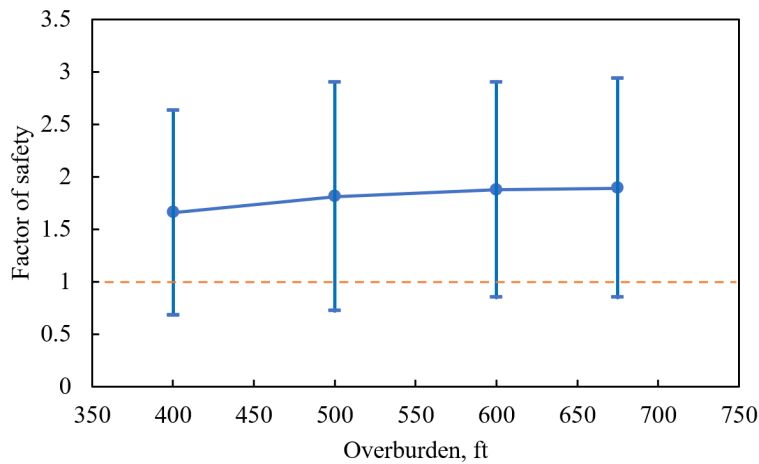


Figure 7.12. Influence of overburdens on the factor of safety of Embankment #1 at the orientation of 90-degree with respect to the longwall mining

7.3 Chart for the Analysis of the Behavior of Embankment #1 Considering Factors of Safety, Directions of Mining and Overburden Levels

Two parameters, direction of mining and overburden levels were considered when constructing a chart that shows their influence on the FS for the case of Embankment #1. For developing this chart, three directions of longwall mining were considered. Also, four overburden

levels were considered for each case of the direction of mining. Thus, to develop these charts, a total of twelve cases were analyzed. For the mining at an orientation of 0-degree, the factor of safety results considering the four overburdens is shown in Appendix C, which is similar to the case of 35-degree discussed in the last section.

As illustrated in this study, the embankment will experience initial, limited deformations at the lower bound of the FS. At large deformation levels in the embankment, when a shear band completely develops, the upper bound FS is in effect. This FS was equal to the traditional factor of safety obtained using the SRM. The upper bound of the factor of safety indicates if the embankment will develop large deformations. All the upper bounds of the factor of safety are much higher than lower bounds of the factor of safety. The lower bounds FS indicated that plastic strains were small and of limited extent inside the embankment. However, it does not mean the embankment is stable. Some limited deformations were observed in the embankment when using the FEM and which were validated by field observations. In addition, the embankment experienced settlement at the regions experiencing high but limited plastic strain. Consequently, to be conservative, the lower bound factor of safety was utilized to identify whether the embankment is stable. The lower bound FS was used when developing the chart used to analyze embankment behavior under longwall mining-induced subsidence.

The lower bound (conservative) factor of safety for each of the twelve cases analyzed are depicted in Table 7.2. The full plot relating the factor of safety versus overburden levels and directions of longwall mining is shown in Fig. 7.13. This chart shows the boundaries for the case of small, medium and large deformations in function of the lower bound FS, the direction of mining, and the overburden level. The factor of safety can be calculated using this figure if the orientation and the overburden are known. It should be noticed that this model assumes that the embankment

is in the center of the panel. Also, the shear parameters of the soil forming the embankment is enhanced by a factor of 1.3 considering the influence of gravel on the shear strength of the soil forming the embankment, as well as the viscosity mobilized in the embankment during subsidence. In addition, the original slope of the embankment was assumed to be equal to 1(rise):2(run).

Table 7.2. Critical Factor of Safety of Embankment #1 subjected to longwall mining with different overburdens and orientations

Orientation Overburden	0°	35°	90°
400-ft	0.98	0.94	0.68
500-ft	1.06	1.04	0.72
600-ft	1.16	1.12	0.85
675-ft	1.24	1.18	0.85

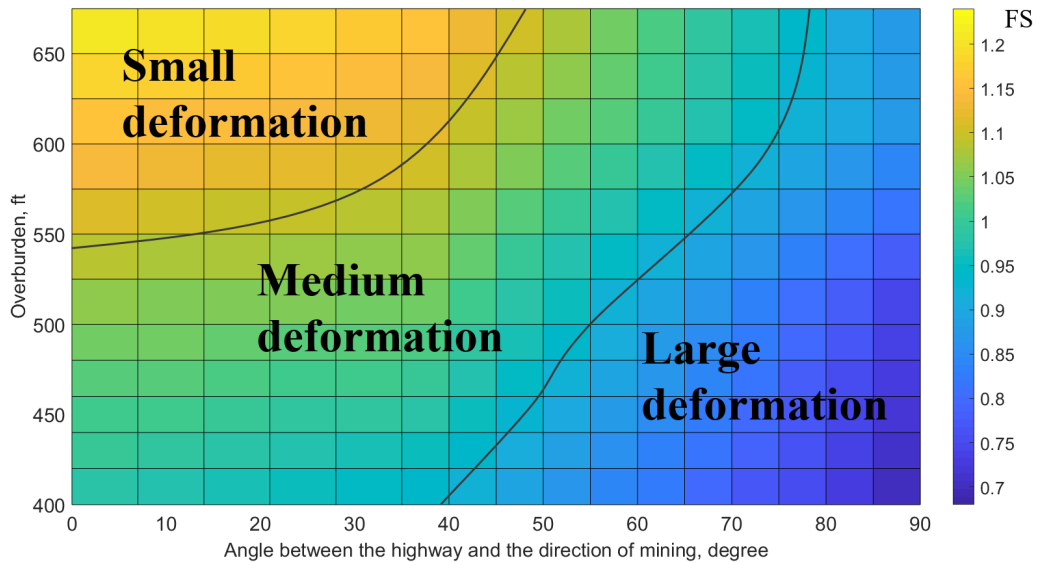


Figure 7.13. Model for the behavior the embankment located in the center of the panel using lower bound FS values, overburden and direction of mining levels

8.0 Finite Element Analysis of Embankment #5

Embankment #5 is in the extended study area of the interstate I-70 that will be undermined in the future. The embankment is in the center of the panel shown in Fig. 8.1. The overburden in this area is around 500-ft. The orientation between the highway and the direction of future mining is 79 degrees. Because of the lower level of overburden, this embankment is expected to be more critical than Embankment #1 which is in the middle of Panel 15 with an has overburden of 675-ft and a direction of longwall mining equal to 35-degree.

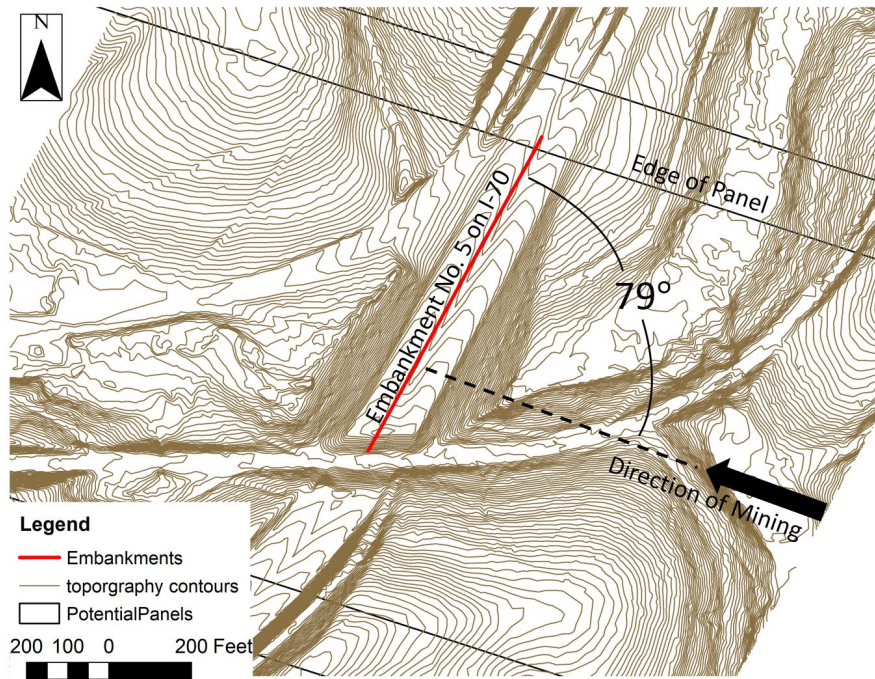


Figure 8.1. Topography of Embankment #5

Deformation and slope stability analysis of Embankment #5 were conducted using FEM. Geometry of Embankment #5 was determined based on the topography. The slope on the north is

1:1.96 and the slope on the south is 1:2.17, which is exactly same to the north and south facing slope of Embankment #1. Besides, Embankment #5 is 70-ft high, 428-ft wide, and 770-ft long. For the reason that the laboratory tests were partially accomplished, material properties for Embankment #5 were assumed same as those utilized in Embankment #1.

A Regression model of the vertical subsidence basin (denoted by rectangles) fitting a SDPS model (denoted by blue dots) with an overburden of 500-ft was constructed using the Richard's model shown in Fig. 8.4. It was implemented into the Finite Element model of Embankment #5 in ABAQUS through the user defined displacement. The maximum subsidence of the ground surface is 4.6-ft which is higher than 4.3-ft of Panel 15 at Embankment #1.

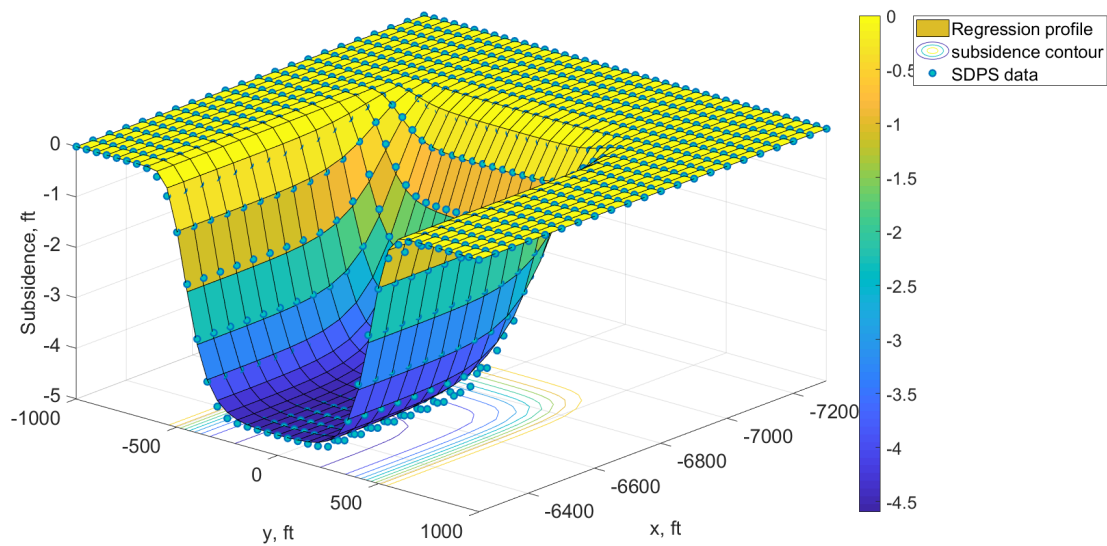


Figure 8.2. Regression model of the subsidence basin with an overburden of 500-ft

8.1 Deformation Analysis of Embankment #5

The deformation analysis of Embankment #5 was conducted using the working face positions summarized in Fig. 8.3. The regression model of subsidence was applied on the bottom of the embankment in the form of displacement. The coordinate system of the embankment in the FEM and the subsidence in the regression function are correlated using the transformation equations.

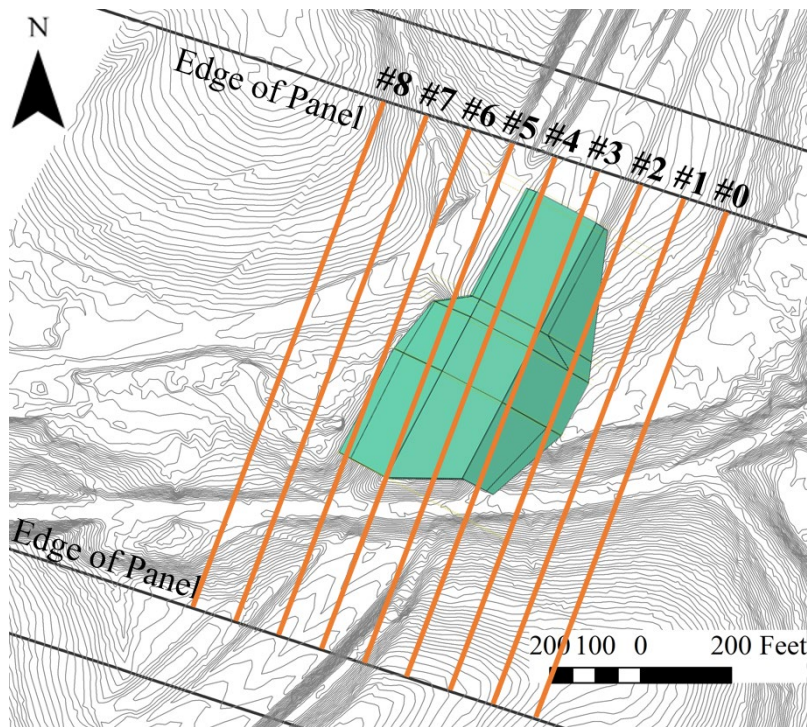


Figure 8.3. Working face positions for Embankment #5

The vertical displacement contours were plotted on Embankment #5 with selected working face positions shown in Fig. 8.4. The displacement is quite small when subjected to gravity only. When the working face is at the middle of the embankment, the soil at the crest of the south slope moves apart perpendicular to the highway direction. The local depression in the form of a sinking

region is shown in a light blue color. This region is located in the center of the edge of the east bound lane along the highway. When the working face passes the embankment, the top of the embankment experience a settlement of about 7.8-ft at two different regions [Fig. 8.4(d)]. Such deformations can be considered very large and can produce damage to the embankment structure.

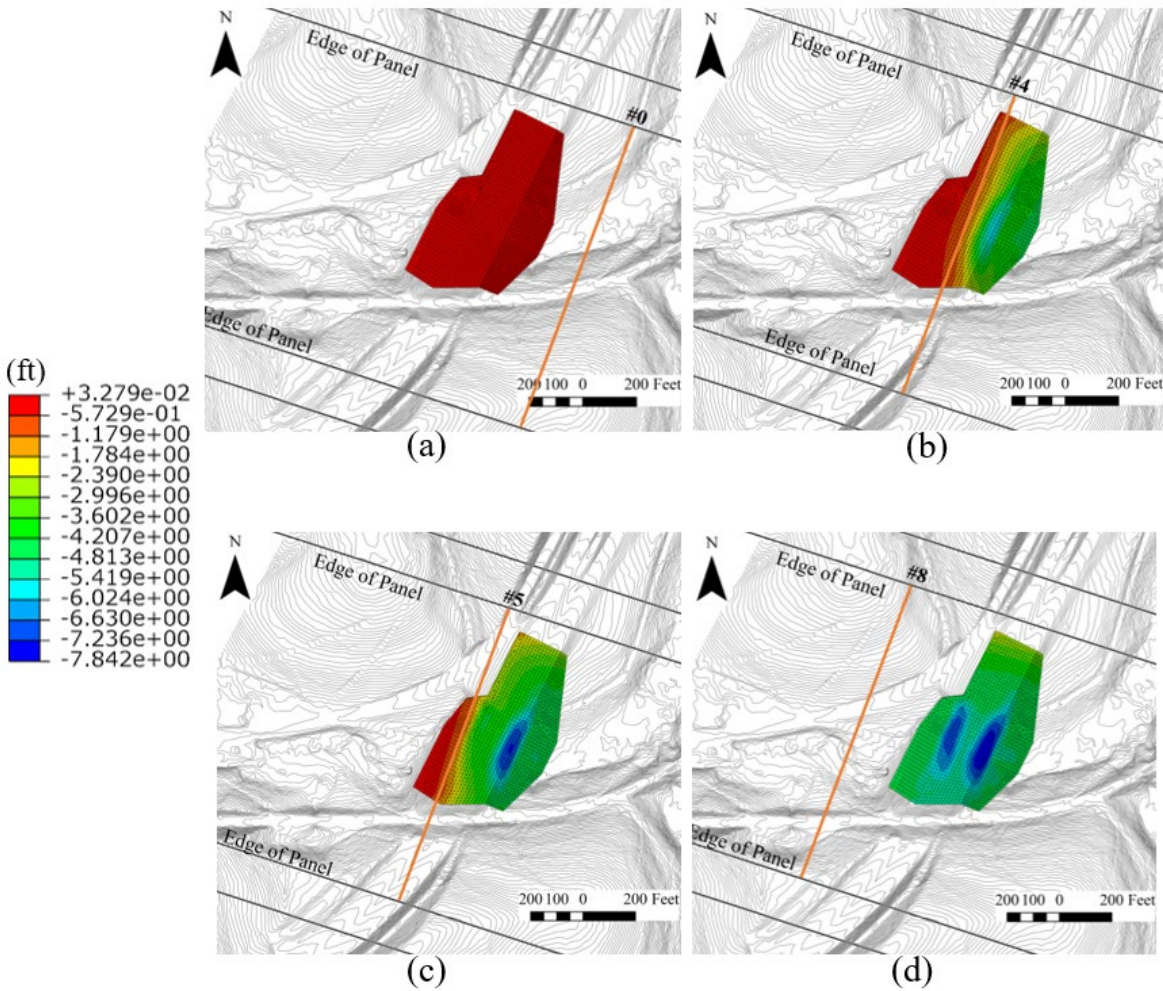


Figure 8.4. Vertical displacement on Embankment #5 with working face position (a) #0; (b) #4; (c) #5; (d) #8

Interior plastic strain was plotted in Fig. 8.6 (b) to explain how the subsidence influence the deformation of the embankment shown in Fig. 8.6 (a). After the embankment is subjected to

successive stages of subsidence, plastic strains develops beneath the crest of the southern slope and the middle of the west bound lane, forming a ‘V’ shape plastic zone. These regions with higher plastic strain correspond to the vertical deformations at the top. The region at the middle of the west bound lane and the southern crest will experienced large concentrated settlements induced by longwall mining-induced subsidence.

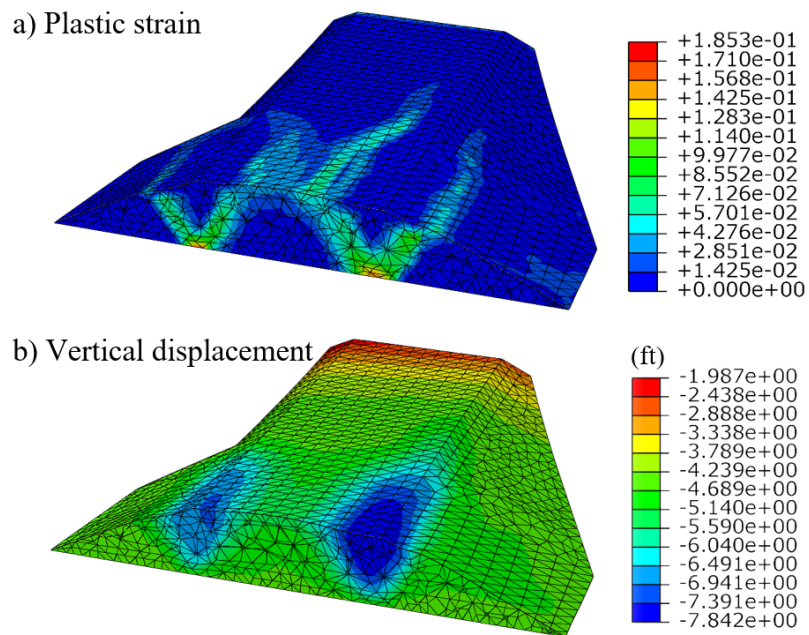


Figure 8.5. (a) Plastic strain contours and (b) Displacement inside Embankment #5 after subsidence

8.2 Slope Stability Analysis of Embankment #5

Slope stability analysis was conducted to find the critical cross section and the factor of safety of Embankment #5. First, the factor of safety of Embankment #5 was calculated under

gravity. It is shown that the critical cross section was on the north facing slope when a thick shear band associated with a region of large plastic strain (Fig. 8.6). The factor of safety under gravity was calculated as 2.8 shown in Fig. 8.7.

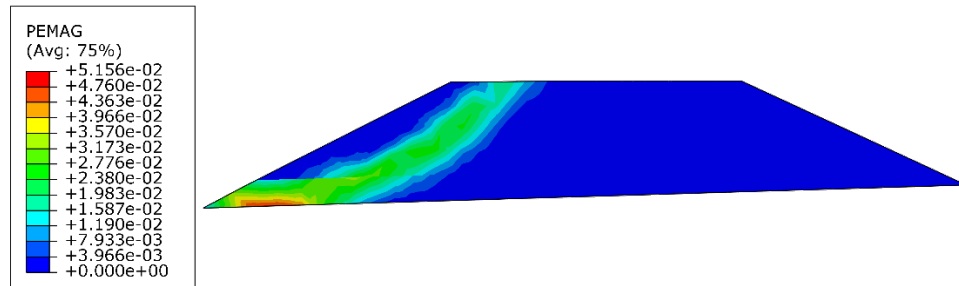


Figure 8.6. Potential slipping surface of Embankment #5 under gravity indicated by plastic strain

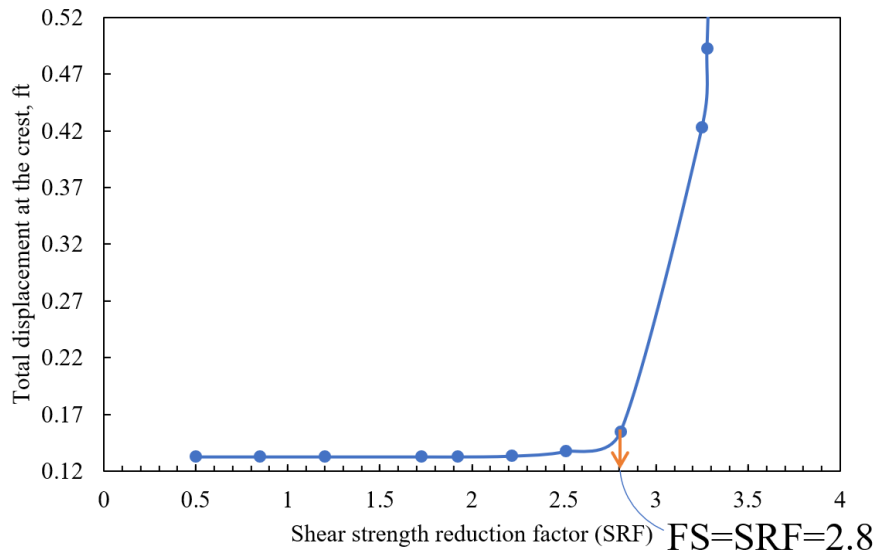


Figure 8.7. Determination of the factor of safety of Embankment #5 under gravity

Then the embankment was subjected to the subsidence. In this case, more deformation was observed before the knee point. The same methodology introduced in Chapter 6 using a lower and upper bound of the FS was applied to characterize the slope stability of Embankment #5.

The critical FS occurred when the longwall working face was located under the middle of embankment with working face #4 shown in Fig. 8.8. Fig. 8.9 indicates that the lower bound FS was found to be 0.8. Before this point, the displacement increased at a relatively low rate. After this point, the embankment presented the initial deformations. The upper bound FS was found to be 2.8, where the total displacement started to increase exponentially and the complete shear band developed at the cross section.

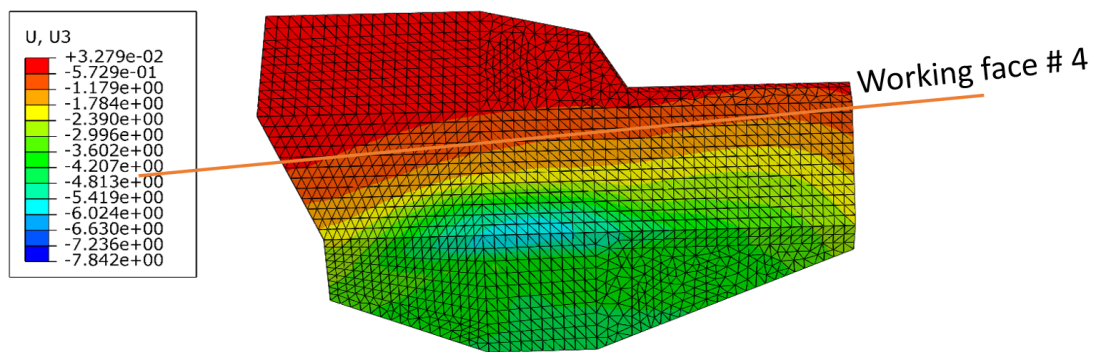


Figure 8.8. Embankment #5 subjected to subsidence from a developing longwall panel with working face #4 showing the position of the longwall face

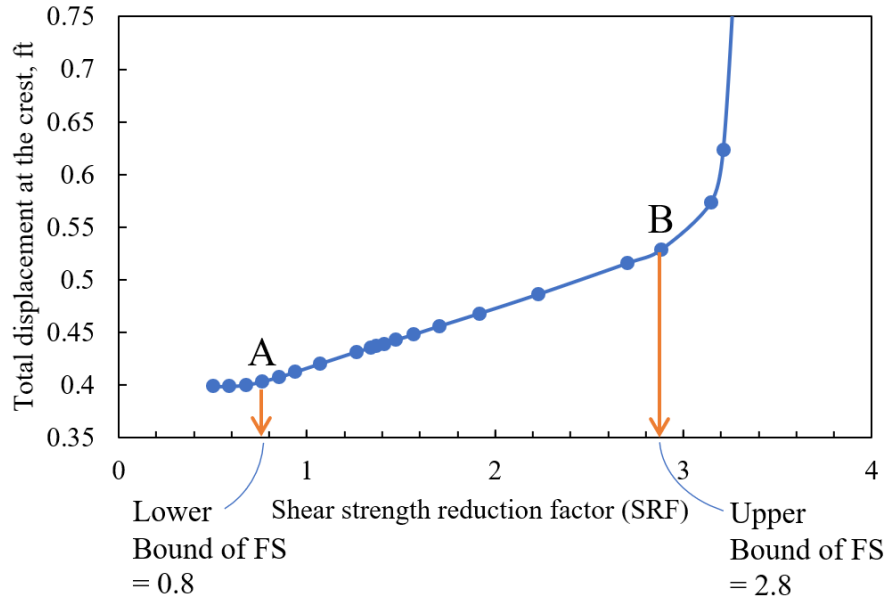


Figure 8.9. Total displacement at the crest of the critical cross section in Embankment #5 versus the shear strength reduction factor for the case with subsidence #4

The plastic strain as well as the horizontal displacement were plotted in Fig. 8.10 and 8.11, respectively. At the lower bound FS, where the small deformation happened, plastic strain initiated. At the upper bound FS, the shear band completely formed and large deformation occurred.

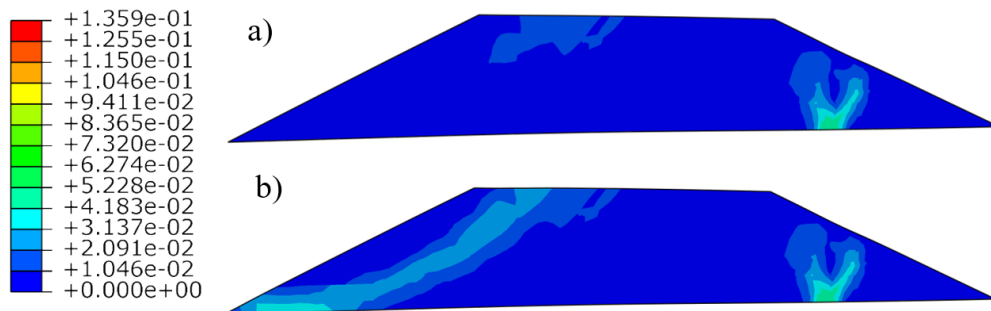


Figure 8.10. Rupture surface at the critical cross section when SRF equals to a)0.8 and b)2.8

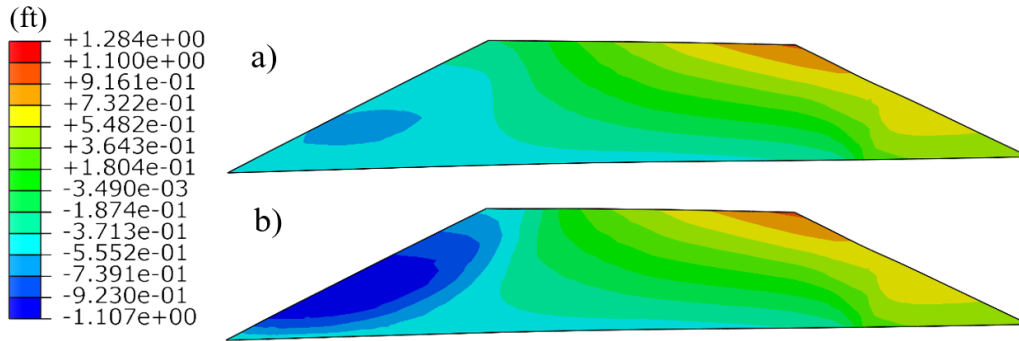


Figure 8.11. Horizontal displacement at the critical cross section when SRF equals to a)0.8 and b)2.8

The factor of safety was calculated in each step of subsidence and is shown in Fig. 8.8. The upper bound for all the factor of safeties were greater than one, indicating that Embankment #5 will be safe but will experience large deformations in the form of shear bands. In the critical stages with working face position at #4 and #5, the lower bound of factor of safety range was calculated as low as 0.8, indicating that the embankment experience plastic strains that were small and of limited extent.

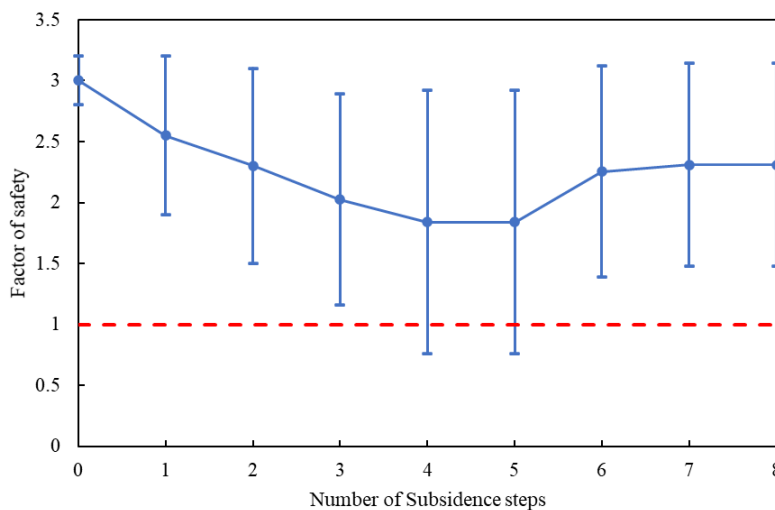


Figure 8.12. Factor of safety for Embankment #5 subjected to subsidence with different working face positions

Considering that the triaxial compression test was conducted only on one soil sample on Embankment #5. The material properties were assumed to be same as the well calibrated Embankment #1. However, there is possibility that the shear strength parameters may differ from those utilized in Embankment #1. Sensitivity tests were conducted on Embankment #5 by using different values of the cohesion (c) and $\tan \phi$ assuming their values are random variables. Random values of c and $\tan \phi$ were generated with correlations using the Monte Carlo method introduced by Griffith [59][60][61].

Two random values in the standard normal distribution $N(0,1)$ was generated using the random number generators in spreadsheet. Then, the two random values in the standard normal distribution were utilized to generate the random c and $\tan \phi$ using the following equations:

$$\begin{aligned} c &= \mu_c + X * \sigma_c \\ \tan \phi &= \mu_{\tan \phi} + \left(X * \rho + Y * \sqrt{1 - \rho^2} \right) \sigma_{\tan \phi} \end{aligned} \quad (8.1)$$

where c and $\tan \phi$ are the random shear parameters to be generated and output for factor of safety calculations in FEM, X and Y are the two random values generated from $N(0,1)$, μ_c and σ_c are the mean and the standard deviation of cohesion which is set to be 550-psf and 140-psf in this case, $\mu_{\tan \phi}$ and $\sigma_{\tan \phi}$ are the mean and the standard deviation of $\tan \phi$ which is set to be 0.72 and 0.086. ρ stands for the correlation between the variation of c and $\tan \phi$. The value of ρ is set to equal -0.3 assuming the variation of c and $\tan \phi$ are negatively correlated. In other words, when the value of $\tan \phi$ is higher than its mean, the value of c would be lower than its mean. The correlation at each generation of c and $\tan \phi$ can be checked using the following equation [62].

$$\rho = \frac{E[(\mu_c - c)(\mu_{\tan \phi} - \tan \phi)]}{\sigma_{\tan \phi} \sigma_c} \quad (8.2)$$

where E represents the expectation function.

The generated shear strength parameters were plugged into the FEM to conduct the SRM procedure in order to calculate the factor of safety for each generation. Totally 10 random c and $\tan \phi$ were obtained from the Monte-Carlo generation. The resulted mean and standard deviation of the 10 generations are checked with respect to the values of mean and standard deviations that are initially set for c and $\tan \phi$. The resulted random shear parameters are summarized in Table 8.1 and plotted in Fig. 8.13. As shown in the table, the mean and standard deviation (SD) of the shear parameters from the Monte-Carlo generation is close to the pre-defined values. Also, the generated blue points are distributed surrounding the orange point representing the defined mean values.

Table 8.1. Generated jointly random variables of shear parameters and the corresponding factor of safety

	$\tan\phi$	ϕ	c , psf	F.S.	Critical FS
1	0.73	36	650	2.5	0.50
2	0.72	36	523	2.6	0.60
3	0.71	35	703	2.7	0.70
4	0.75	37	350	2.4	0.40
5	0.86	41	507	2.6	0.60
6	0.87	41	628	2.7	0.70
7	0.63	32	549	2.4	0.60
8	0.76	37	541	2.8	0.70
9	0.62	32	556	2.4	0.50
10	0.73	36	657	2.5	0.50
mean	0.74		566.4		
SD	0.08		100.5		

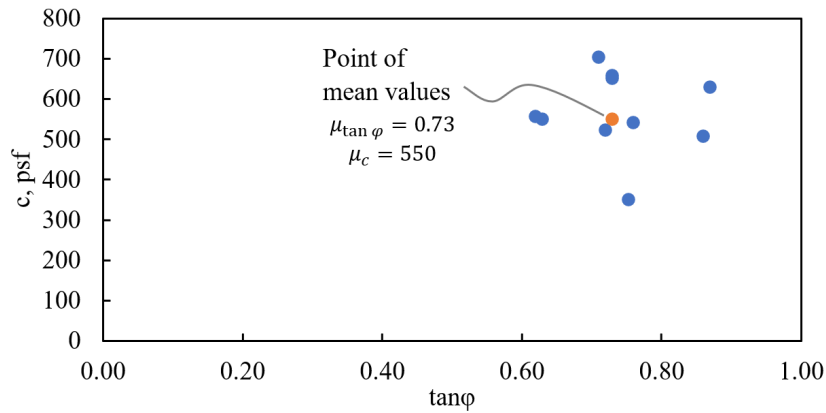


Figure 8.13. Distribution of the generated random shear parameters

The resulted factors of safety calculated using these ten random shear parameters are plotted in Fig. 8.14. It is indicated that the upper bound factor of safety (FS) ranges from 2.4 to 2.8. The lower bound FS (critical FS) ranges from 0.4 to 0.8. Through doing the sensitivity tests, the possible variation of the shear parameters was taken into consideration. The resulting factor of safety range for the upper and lower bound was obtained to better predict the stability and behavior of Embankment #5.

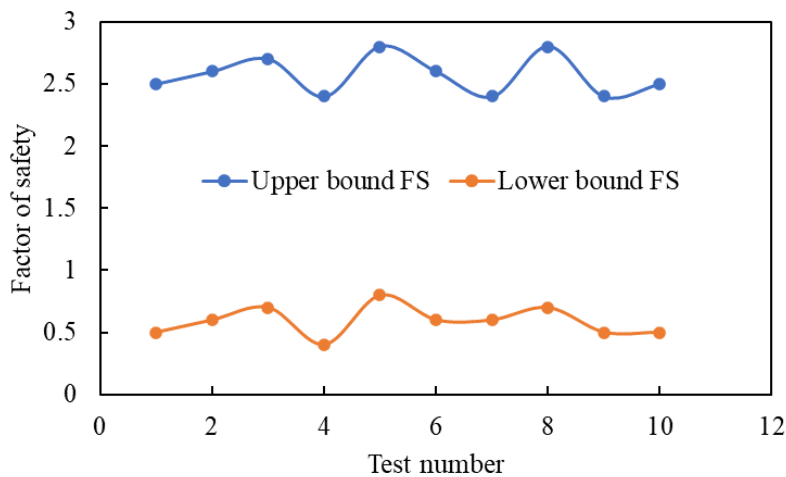


Figure 8.14. Resulting factor of safety calculated in FEM using the random shear parameters

Although Embankment #5 will be we relatively stable during subsidence, it will experience significant deformations affecting detrimentally the geometry of the embankment. Soil will settle in the embankment as much as 7.8-ft, forming a longitudinal sink at the crest of the southern slope and in the middle of west bound lane. A bulge was also caused on the slope by the basin at the crest. These levels of deformations can make the highway embankment unsafe.

The model obtained in Chapter 7 (Fig. 7.13) was used to calculate the factor of safety of Embankment #5 in function of direction of mining and levels of overburden. With an overburden of 500-ft and an orientation of 79-degree, the conservative factor of safety for Embankment #5 turns out to be 0.8 from the plot, which is identical to that from the FEM. The chart shown in Fig. 7.13 can be used to evaluate the degree of deformations and stability for highway embankments in the State of Pennsylvania that in the future will be subjected to subsidence due to longwall mining.

9.0 Conclusions

In this study, the evaluation of the influence of subsidence due to longwall mining on the deformations and stability of highway embankments located along highway I-70 near the Pennsylvania-West Virginia border was carried out. The evaluation was made using a numerical method (FEM) and field measurements. The following conclusions can be reached from this study:

1. The amount and location of the embankments' deformations obtained from the numerical analysis were compared with those obtained from field measurements (that employed slope stakes in conjunction with Lidar, inclinometers and piezometers). Both gave similar results for these parameters, indicating the feasibility of the FEM to predict the deformations of the embankments.

2. Using the FEM, a slope stability analysis of the embankments was conducted at each step of the dynamic subsidence resulting from the longwall mining. Critical sections in the embankments, representing those that experienced large deformations, were used in the stability calculations that used the strength reduction method (SRM). Factors of safety (FS) and their equivalent shear strength reduction factors (SRF) were calculated at these sections. A limit equilibrium method (LEM) that uses the software SLIDE was also used to validate the SMR results. A factor of safety range is proposed to describe the slope stability of the embankments. This range includes a lower bound and an upper bound values of the FS.

3. The lower bound of the FS identifies an embankment experiencing small and limited in extent plastic deformations. The upper bound of the FS was related to an embankment that experience large plastic deformations that were concentrated in a shear band. The presence of this shear band in one of the embankments was substantiated by inclinometers.

4. The upper bound of the FS developed as a response to the slightly strain-hardening behavior of the soils forming part of the embankments. This behavior of the soils was obtained from triaxial compression tests. Thus, as a result of deformations in the embankment induced by subsidence, the embankment becomes stronger and therefore safer with respect to slope instabilities.

5. The slightly strain-hardening behavior of the soils forming part of the embankment has two causes. One was the mobilization of the viscosity of the soils (in addition to the mobilization of their cohesion and friction) that takes place when large deformations are in effect. The other was the presence of dispersed rock fragments in the soils forming the embankments. The presence of these rock fragments increases the shear strength of the soil-rock mixtures when they experienced large deformations.

6. A parametric study that uses the FEM was conducted to explore the influence that the orientation angle of the longwall mining with respect the embankments' location, and the levels of overburden above the longwall mine have on the deformations and stability of the embankments. The numerical analysis indicated that the larger the orientation angle, the larger were the deformation levels in the embankments. Also, the lower the overburden levels, the larger were the deformation levels in the embankments. Since the soils forming part of the embankments have a slightly strain-hardening response to deformations, the stability of the embankments increased with the deformations.

7. Evaluation charts that uses relating direction of mining, overburden levels, deformation levels and the lower bound FS were developed. These charts can be used to predict instabilities of embankments subjected to future longwall mining in the state of Pennsylvania.

Appendix A Pseudo Code for Duncan-Chang's Model in UMAT Subroutine

1. Inputs:

- a. Define arrays with the correct dimensions (utility arrays defined by default in UMAT are ignored here such as the stress σ , strain ϵ , etc.): σ_p (3) to store the principal stress, $\Delta\sigma$ (6) to store the stress increments, $\Delta\sigma_t$ (6) to store the tangent stress increments, σ_t (6) to store the tangent stress with a half of strain increment.
- b. Assign the Duncan-Chang model parameters given by solution-dependent state variables (Depvar) that are defined in the material properties module in Graphical User Interface (GUI): $K, n, R_f, c, \varphi, G, D, F, K_{ur}, p_a, \Delta\phi$
- c. Assign the initial deviator stress, confining stress and the stress level given by the state variable (STATEV) defined in Key Words in GUI:

$$(\sigma_1 - \sigma_3)_{max} \leftarrow \mathbf{STATEV} \quad (1)$$

$$(\sigma_3)_{max} \leftarrow \mathbf{STATEV} \quad (2)$$

$$SL \leftarrow \mathbf{STATEV} \quad (3)$$

2. Apply subroutine function $f_{ps}(\sigma, \sigma_p, N, \text{stress})$ to calculate the principal stress and store them in the σ_p in the correct order (taking compression as positive), N. stress=6 in this case.

Subroutine function $f_{ps}(\sigma, \sigma_p, N, \text{stress})$:

Utilize the utility subroutine function $uf_{ps}(\boldsymbol{\sigma}, \boldsymbol{\sigma}_p)$ to calculate the principal stresses and store them into the $\boldsymbol{\sigma}_p$. In ABAQUS, tension is positive, compression is negative. First put them in the correct order from low to high.

For $i=1:2$

For $j=i+1:3$

If $\boldsymbol{\sigma}_p(i) > \boldsymbol{\sigma}_p(j)$, then exchange the values at these two positions

$$variable = \boldsymbol{\sigma}_p(i)$$

$$\boldsymbol{\sigma}_p(i) = \boldsymbol{\sigma}_p(j)$$

$$\boldsymbol{\sigma}_p(j) = variable$$

Then do another loop to reverse the signal of the stress:

For $k=1:3$

$$\boldsymbol{\sigma}_p(k) = -\boldsymbol{\sigma}_p(k)$$

3. Update friction angle:

$$\varphi = \varphi_0 - \Delta\varphi l g \frac{\sigma_3}{p_a}$$

4. Apply subroutine function $f_{E,v}(\boldsymbol{\sigma}_p, K, n, R_f, c, \varphi, \nu, p_a, K_{ur}, E, S, \sigma_3, G, D, F, SL, (\sigma_1 - \sigma_3))$ to calculate the tangent Young's modulus and Poisson's ratio for the current stress level.

Subroutine function $f_{E,v}(\boldsymbol{\sigma}_p, K, n, R_f, c, \varphi, \nu, p_a, K_{ur}, E, S, \sigma_3, G, D, F, SL, (\sigma_1 - \sigma_3))$:

$$S = (\sigma_1 - \sigma_3)(1 - \sin \varphi)$$

If $c \cos \varphi + \sigma_3 \sin \varphi < 0$, then $S = 0.99$;

Else, $S = S / (2 c \cos \varphi + 2 \sigma_3 \sin \varphi)$, If $S > 0.99$, then $S = 0.99$.

The tangent Young's modulus is calculated as

$$E = K p_a (\sigma_3 / p_a)^n (1 - R_f S)^2$$

To calculate the Poisson's ratio,

$$AA = \frac{D(\sigma_1 - \sigma_3)}{K p_a (\sigma_3 / p_a)^n (1 - R_f S)}$$

$$\nu = \frac{G - F \lg(\sigma_3 / P_a)}{(1 - A)^2}$$

If $\nu > 0.49$, then $\nu = 0.49$

If $\nu < 0.05$, then $\nu = 0.05$

If $S < SL$ and $(\sigma_p(1) - \sigma_p(3)) < (\sigma_1 - \sigma_3)_{max}$, then

$$E = K_{ur} p_a (\sigma_3 / P_a)^n$$

5. Calculate K, G, λ

$$3K = \frac{E}{1 - 2 * \nu}$$

$$2G = \frac{E}{1 + \nu}$$

$$G = 2G/2$$

$$3G = 3 * G$$

$$\lambda = \frac{3K - 2G}{3}$$

6. Calculate the Jacobian matrix using the subroutine function

$f_j(\bar{J}, \text{No. of stress components, No. of normal stress components, } \lambda, 2G, G)$:

Set the dimension of \bar{J} to be 6×6 ,

Set the initial value to be zero:

For $i = 1:6$

For $j = 1:6$

$$\bar{J}(i, j) = 0$$

Construct the 3×3 matrix in the upper part of Jacobian matrix:

For $i = 1:3$

For $j = 1:3$

$$\bar{J}(j, i) = \lambda$$

$$\bar{J}(i, i) = 2G + \lambda$$

Construct the diagonal in the lower part of Jacobian matrix:

For $i = 4:6$

$$\bar{J}(i, i) = G$$

7. Update the $\Delta\sigma$ from $\Delta\epsilon$ using the subroutine function

$f_s(\bar{J}, \Delta\sigma_t, \Delta\epsilon, \text{No. of stress components})$

Set $\Delta\sigma_t = 0$,

Apply subroutine function $f_s(\bar{J}, \Delta\sigma_t, \Delta\epsilon, \text{No. of stress components})$ to find $\Delta\sigma$.

Subroutine function $f_s(\bar{J}, \Delta\sigma_t, \Delta\epsilon, \text{No. of stress components})$:

Set the dimensions of the matrix and arrays: $\bar{J}(6,6)$, $\Delta\epsilon(6)$, $\Delta\sigma_t(6)$

For $i = 1:6$

For $j = 1:6$

$$\Delta\sigma_t(i) \leftarrow \Delta\sigma_t(i) + \bar{J}(i, j) * \Delta\epsilon(j)$$

8. The mid-point method is introduced. The stress state at the midpoint is updated using the half of the stress increment. The Jacobian matrix is updated using the mid-point stress state.

For $i = 1:6$

$$\sigma_t(i) \leftarrow \sigma_t(i) + 0.5 * \Delta\sigma_t(i)$$

9. Update the principal stress by conducting Step 2.

$$\sigma_p \leftarrow f_{ps}(\sigma, \sigma_p, \text{N. stress})$$

10. Update the Jacobian matrix by conducting Step 4-6.

$$E, \nu \leftarrow f_{E,\nu}(\sigma_p, K, n, R_f, c, \varphi, \nu, p_a, K_{ur}, E, S, \sigma_3, G, D, F, SL, (\sigma_1 - \sigma_3))$$

Update $\lambda, 2G, G$

$$\bar{J} \leftarrow f_j(\bar{J}, \text{No. of stress components, No. of normal stress components, } \lambda, 2G, G)$$

11. Update the stress increment with the strain increment

For $i = 1:6$

For $j = 1:6$

$$\Delta\sigma(i) \leftarrow \Delta\sigma(i) + \bar{J}(i, j) * \Delta\varepsilon(j)$$

12. Update the stress

For $i = 1:6$

$$\sigma(i) \leftarrow \sigma(i) + 0.5 * \Delta\sigma(i)$$

13. Update the Jacobian matrix by reconducting step 10.

$$E, \nu \leftarrow f_{E,\nu}(\sigma_p, K, n, R_f, c, \varphi, \nu, p_a, K_{ur}, E, S, \sigma_3, G, D, F, SL, (\sigma_1 - \sigma_3))$$

Update $\lambda, 2G, G$

$$\bar{J} \leftarrow f_j(\bar{J}, \text{No. of stress components, No. of normal stress components, } \lambda, 2G, G)$$

14. Update the State Variable (STATEV):

$$\text{If } \sigma_p(3) > (\sigma_3)_{max}, \text{ then } (\sigma_3)_{max} \leftarrow \sigma_p(3)$$

$$\text{If } (\sigma_p(1) - \sigma_p(3)) > (\sigma_1 - \sigma_3)_{max},$$

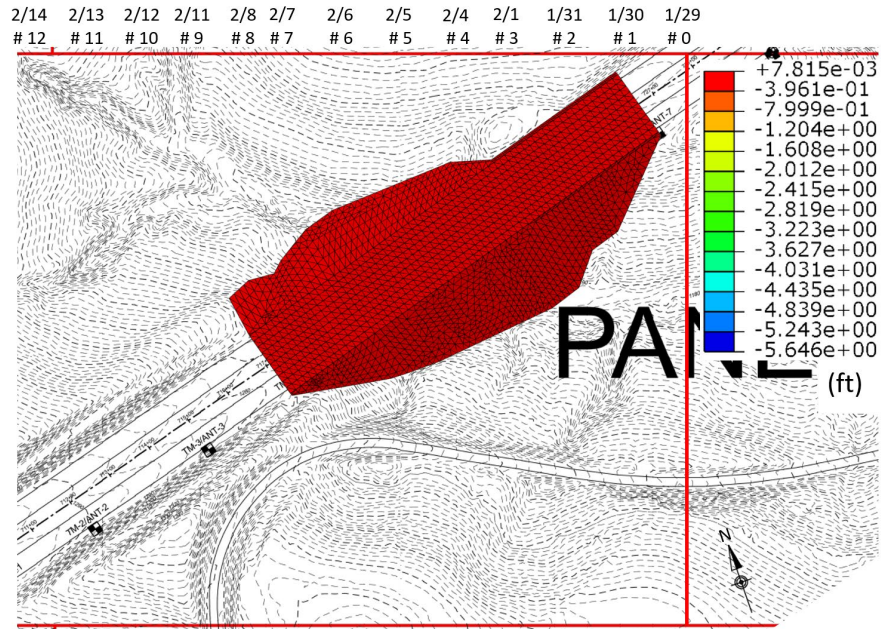
$$\text{then } (\sigma_1 - \sigma_3)_{max} \leftarrow (\sigma_p(1) - \sigma_p(3))$$

$$\mathbf{STATEV} (1) \leftarrow (\sigma_1 - \sigma_3)_{max}$$

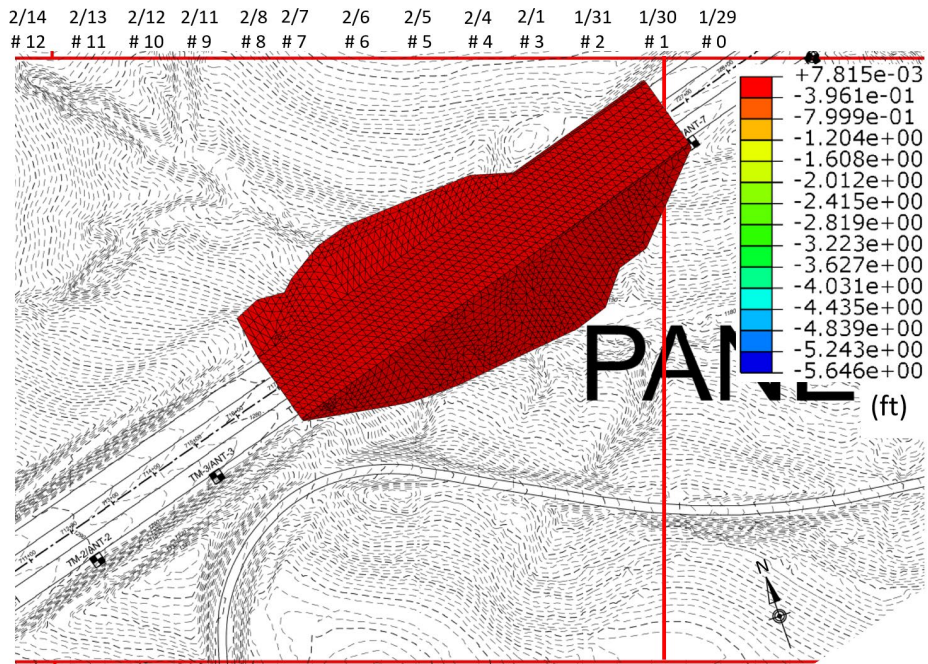
$$\mathbf{STATEV} (2) \leftarrow (\sigma_3)_{max}$$

$$\mathbf{STATEV} (3) \leftarrow SL$$

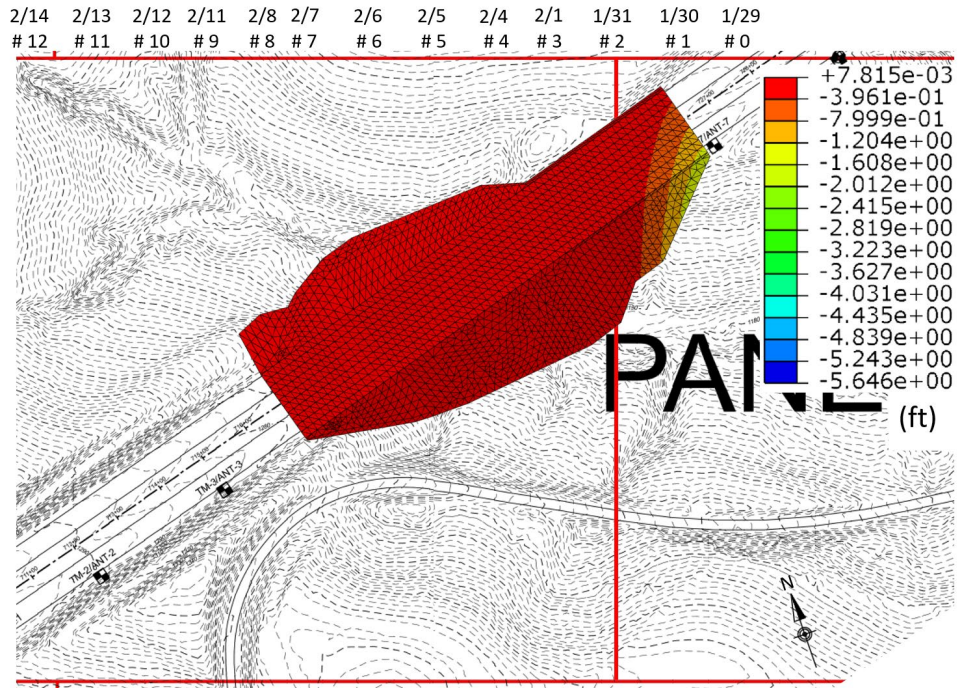
Appendix B Subsidence Contour on Embankment #1



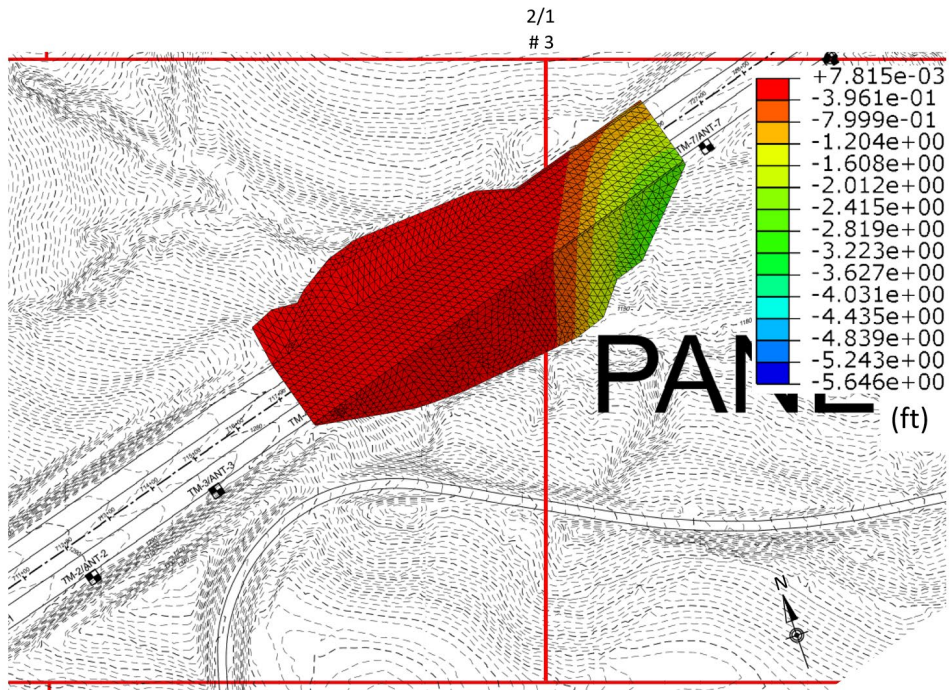
Appendix Figure 1 Vertical displacement on Embankment #1 with working face position #0



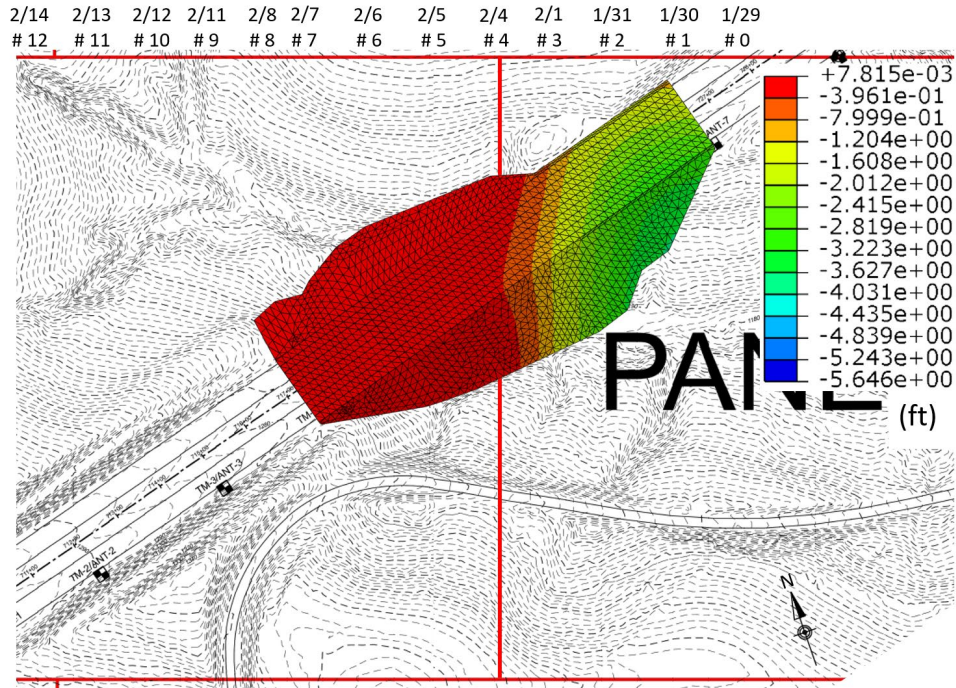
Appendix Figure 2 Vertical displacement on Embankment #1 with working face position #1



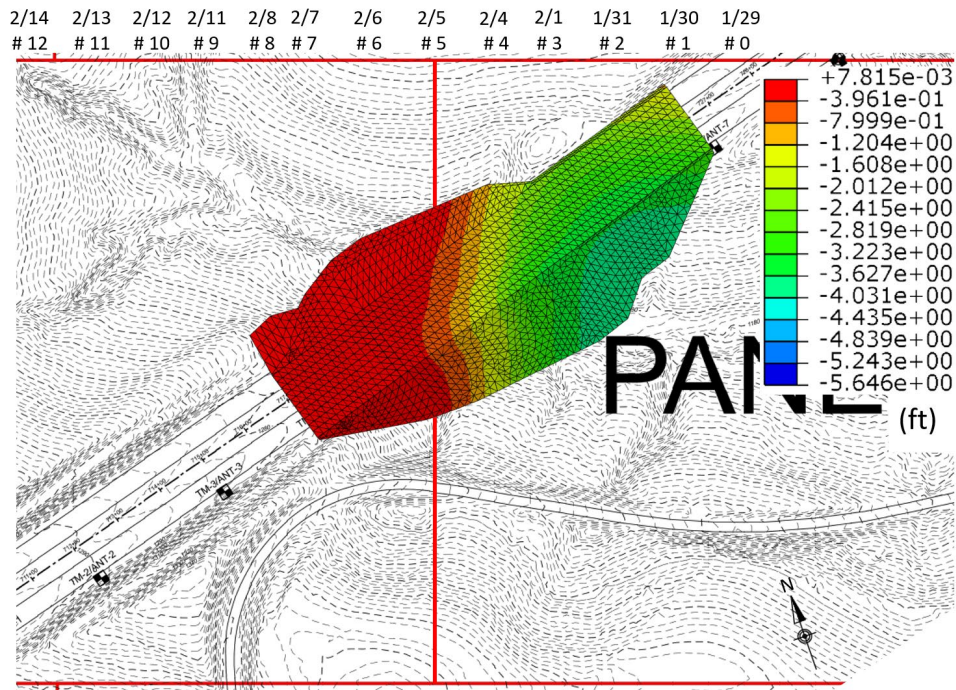
Appendix Figure 3 Vertical displacement on Embankment #1 with working face position #2



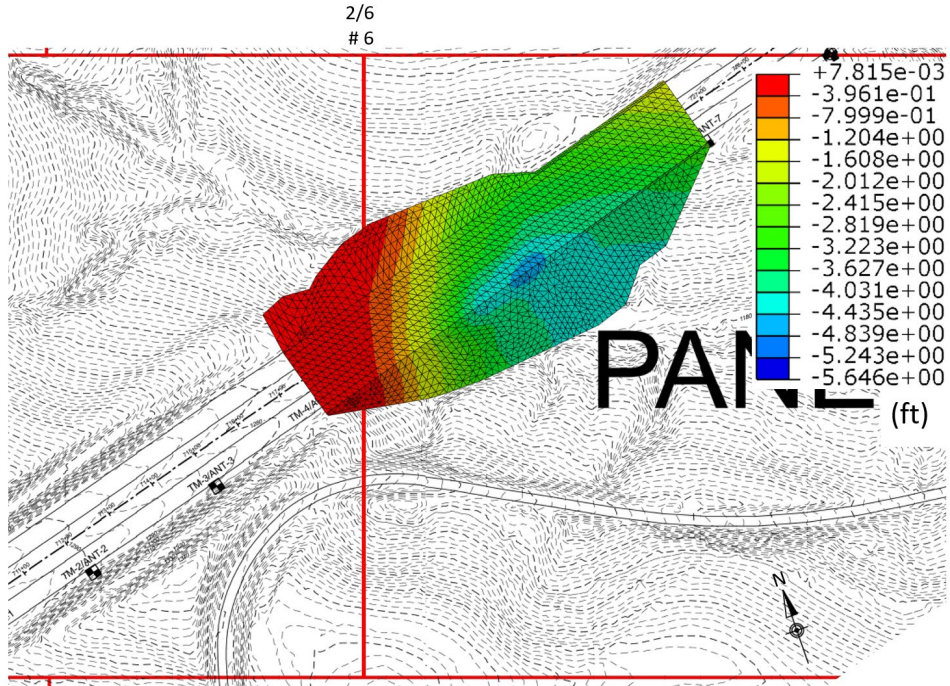
Appendix Figure 4 Vertical displacement on Embankment #1 with working face position #3



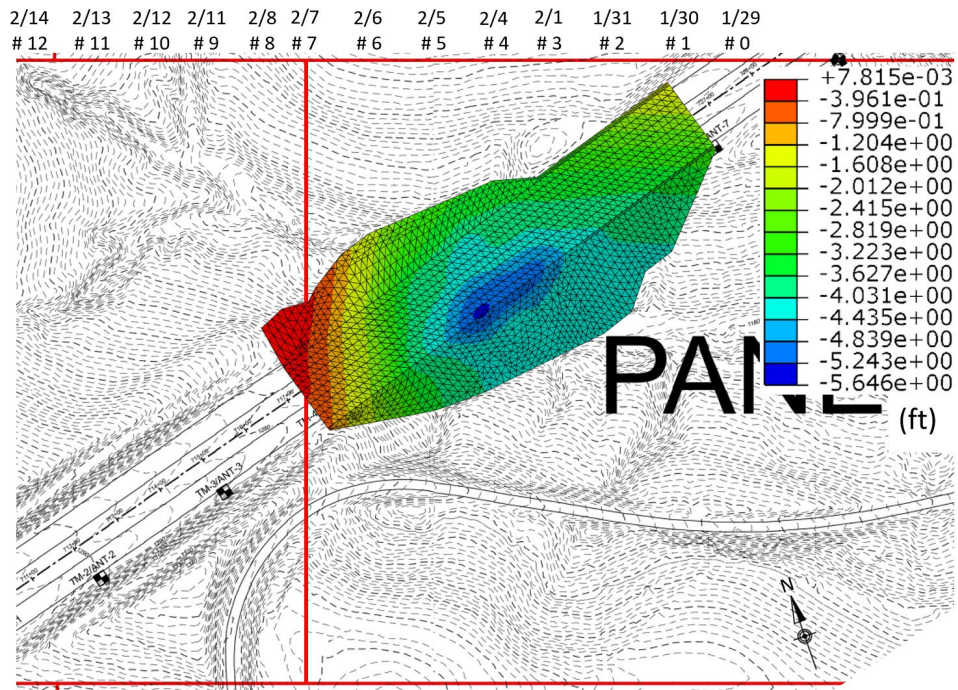
Appendix Figure 5 Vertical displacement on Embankment #1 with working face position #4



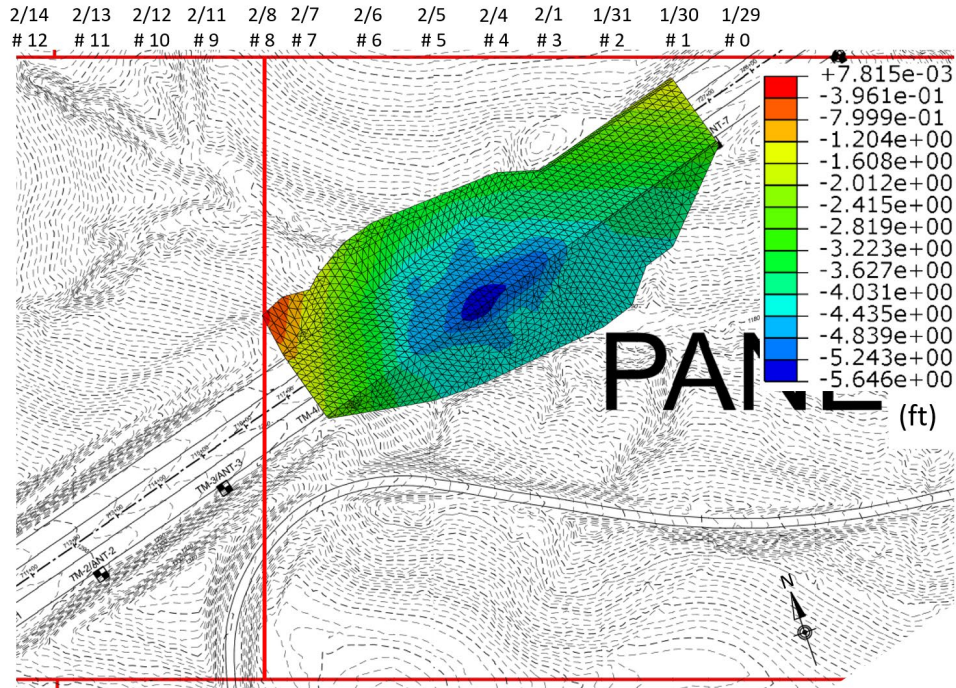
Appendix Figure 6 Vertical displacement on Embankment #1 with working face position #5



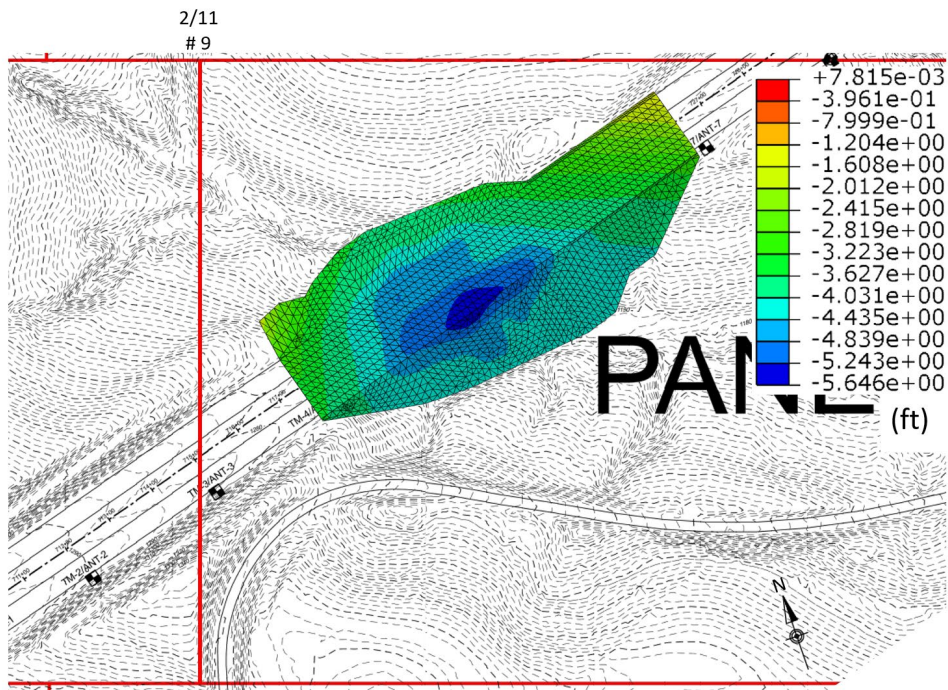
Appendix Figure 7 Vertical displacement on Embankment #1 with working face position #6



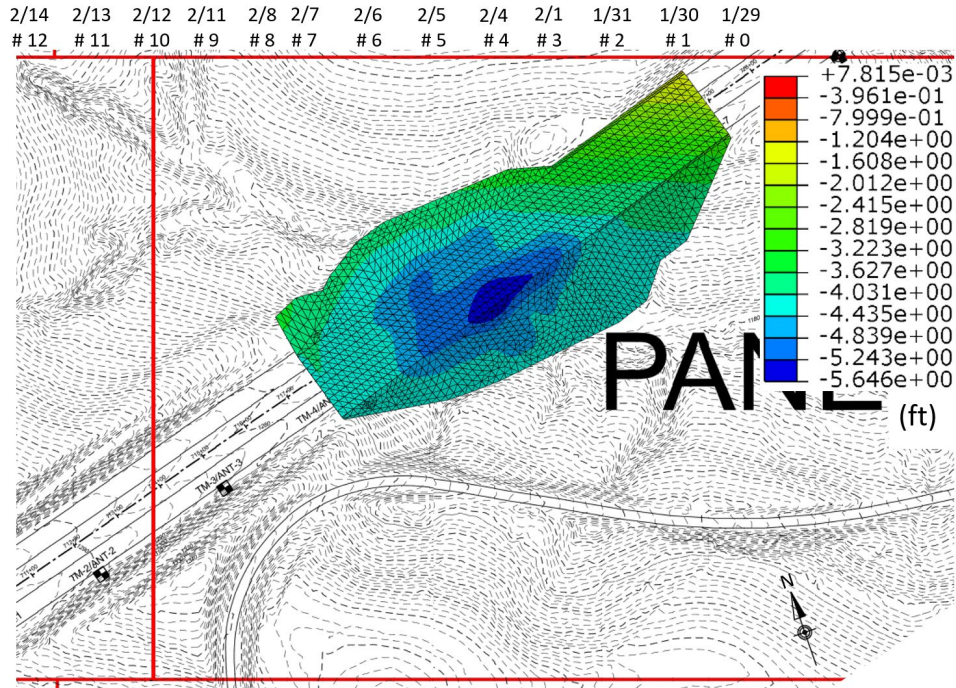
Appendix Figure 8 Vertical displacement on Embankment #1 with working face position #7



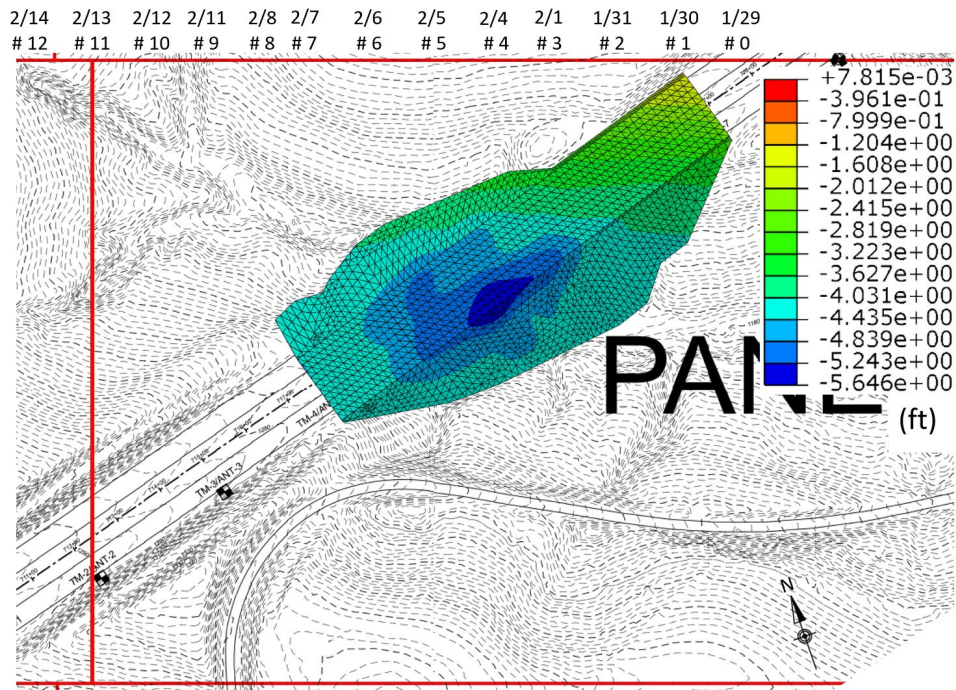
Appendix Figure 9 Vertical displacement on Embankment #1 with working face position #8



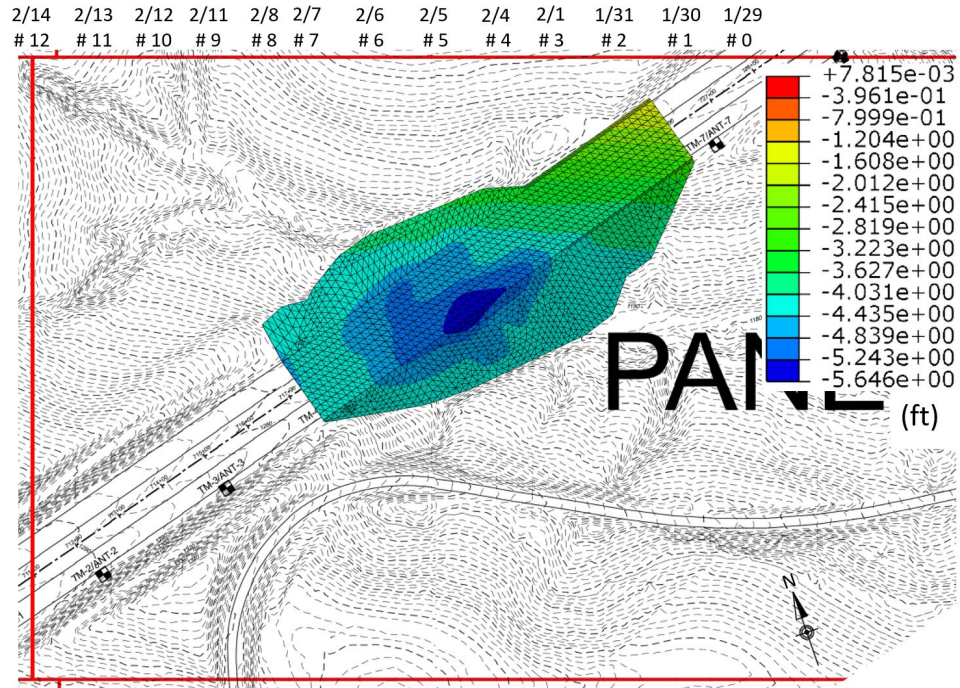
Appendix Figure 10 Vertical displacement on Embankment #1 with working face position #9



Appendix Figure 11 Vertical displacement on Embankment #1 with working face position #10

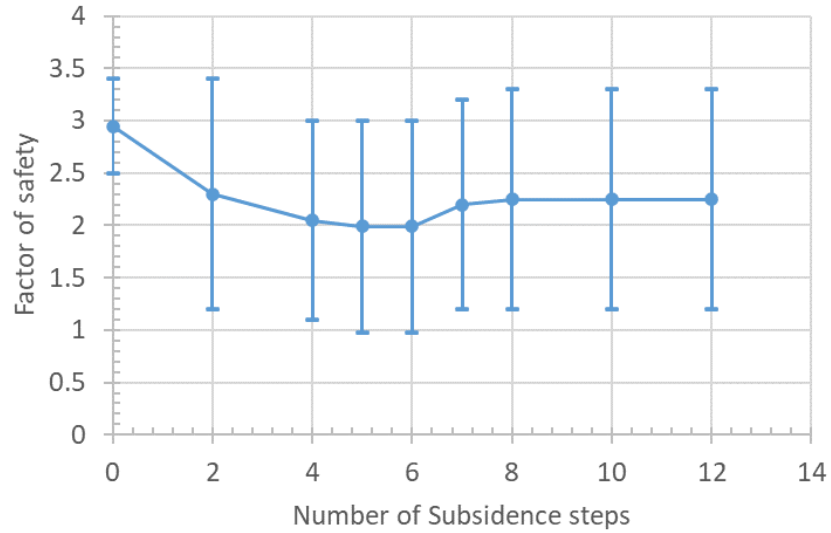


Appendix Figure 12 Vertical displacement on Embankment #1 with working face position #11

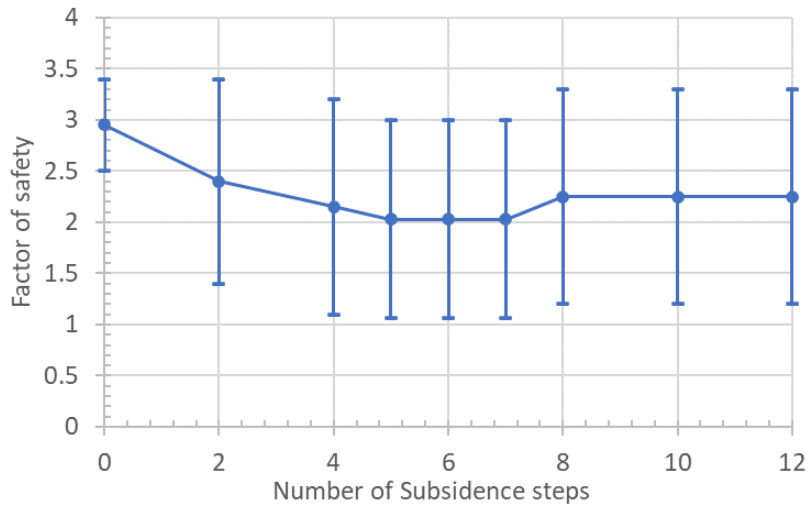


Appendix Figure 13 Vertical displacement on Embankment #1 with working face position #12

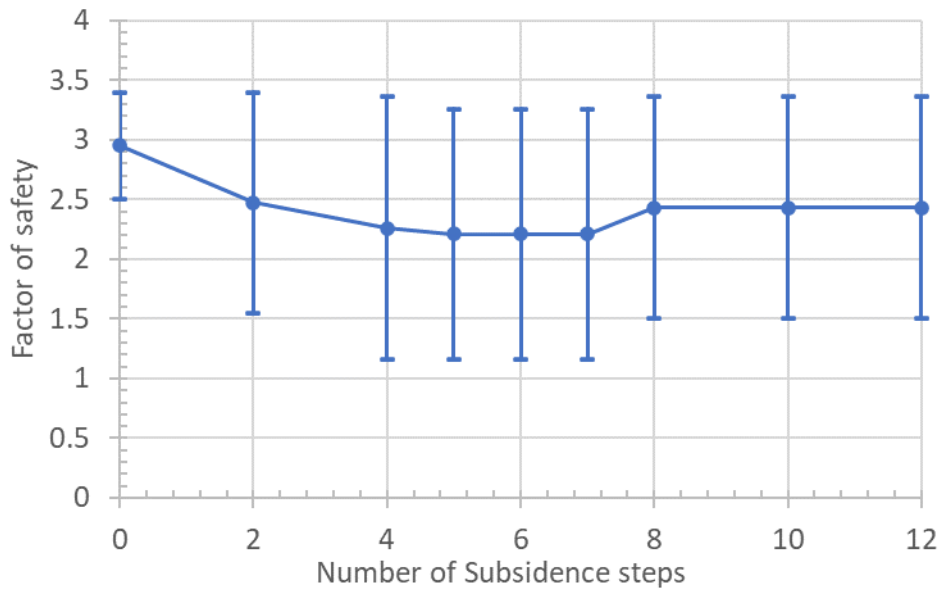
Appendix C Factor of Safety for the Case of 0-Degree with Different Overburdens



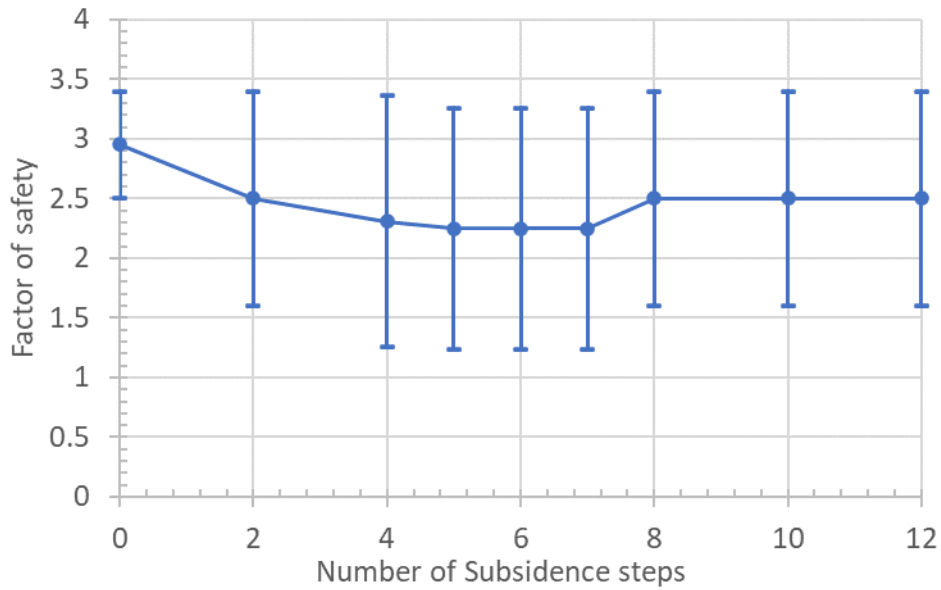
Appendix Figure 14 Variation of the FS of Embankment #1 subjected to subsidence with an orientation of 0-degree and an overburden of 400-ft



Appendix Figure 15 Variation of the FS of Embankment #1 subjected to subsidence with an orientation of 0-degree and an overburden of 500-ft

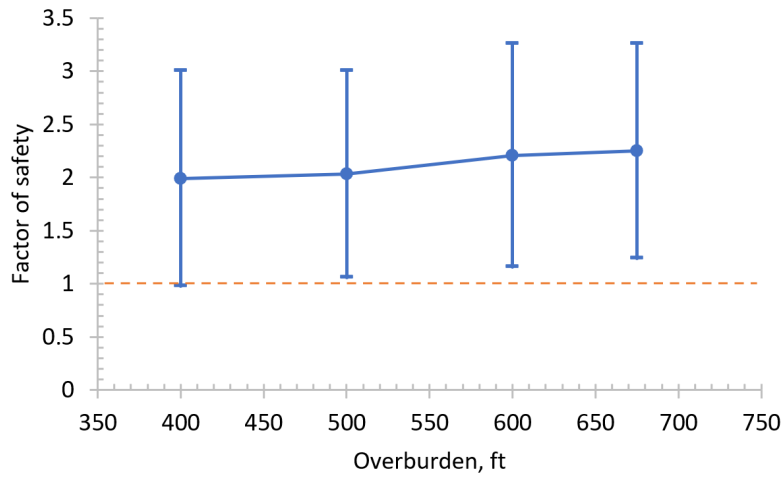


Appendix Figure 16 Variation of the FS of Embankment #1 subjected to subsidence with an orientation of 0-degree and an overburden of 600-ft



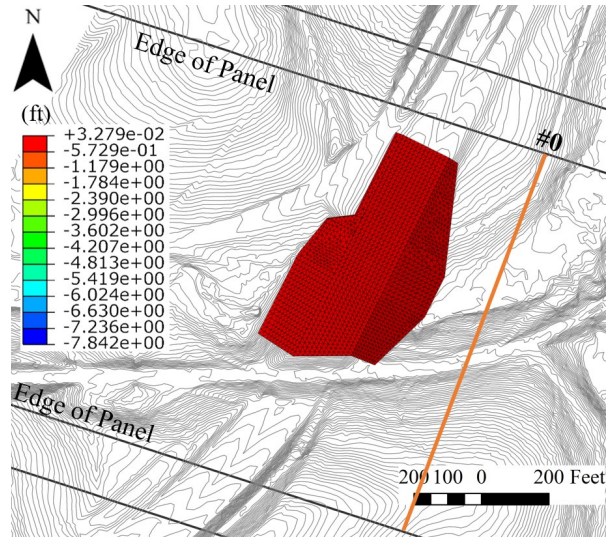
Appendix Figure 17 Variation of the FS of Embankment #1 subjected to subsidence with an orientation of 0-degree and an overburden of 675-ft

Then the critical factor of safety from the four figures above are compared as follows to investigate the influence of overburden on the factor of safety of Embankment #1 when the highway orientation with respect to the mining is 0-degree.

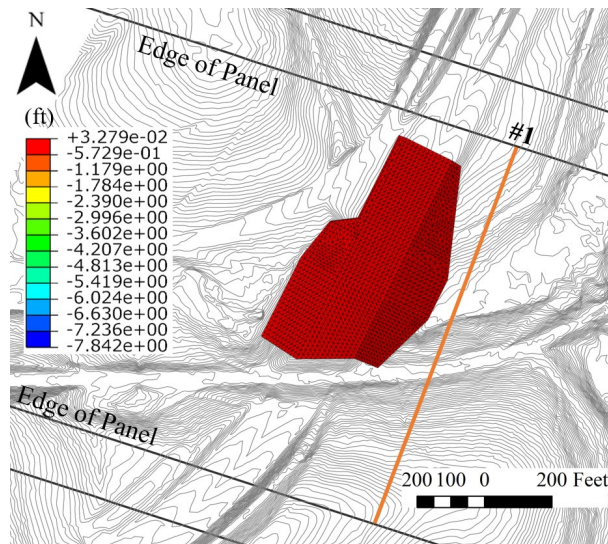


Appendix Figure 18 Influence of overburden on the factor of safety of Embankment #1 when the highway orientation with respect to the mining is 0-degree

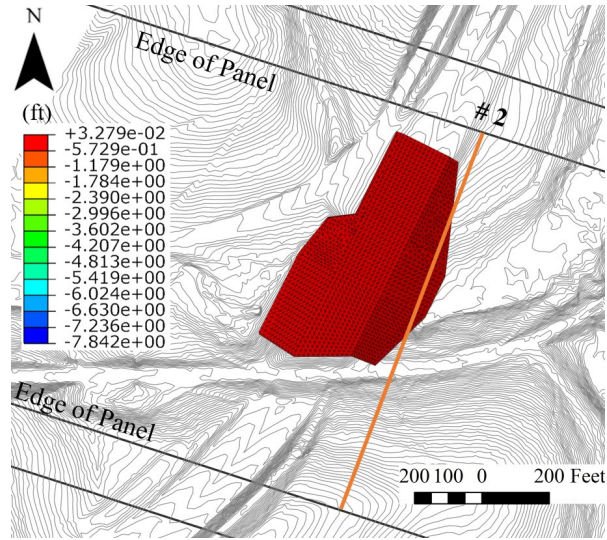
Appendix D Subsidence Contour on Embankment #5



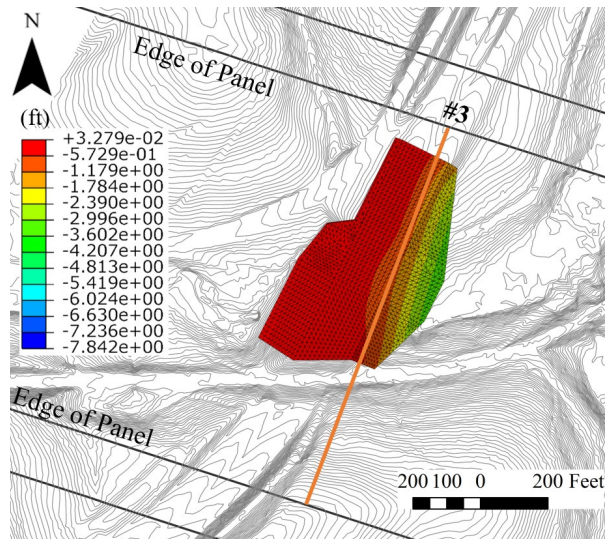
Appendix Figure 19 Vertical displacement on Embankment #5 with working face position #0



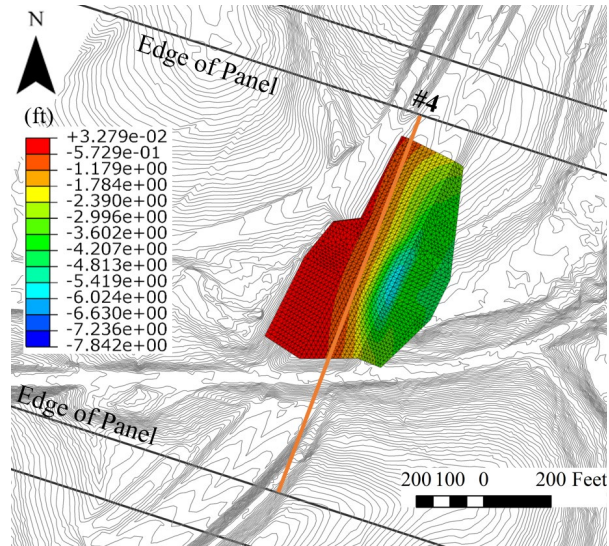
Appendix Figure 20 Vertical displacement on Embankment #5 with working face position #1



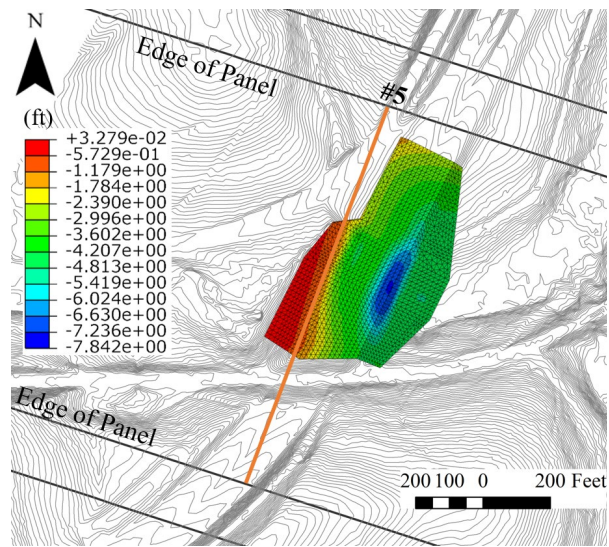
Appendix Figure 21 Vertical displacement on Embankment #5 with working face position #2



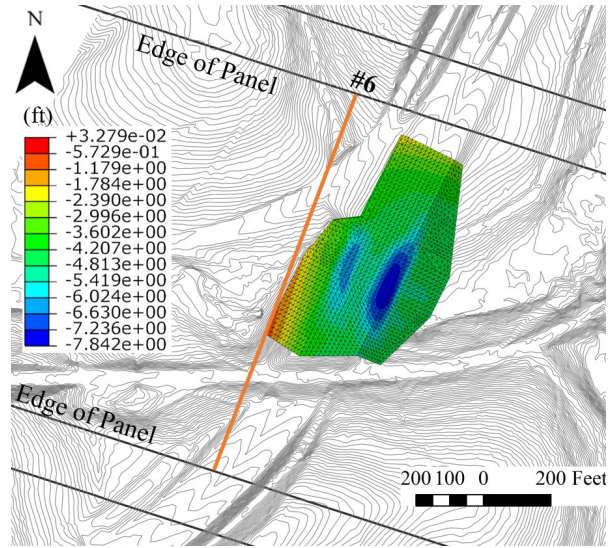
Appendix Figure 22 Vertical displacement on Embankment #5 with working face position #3



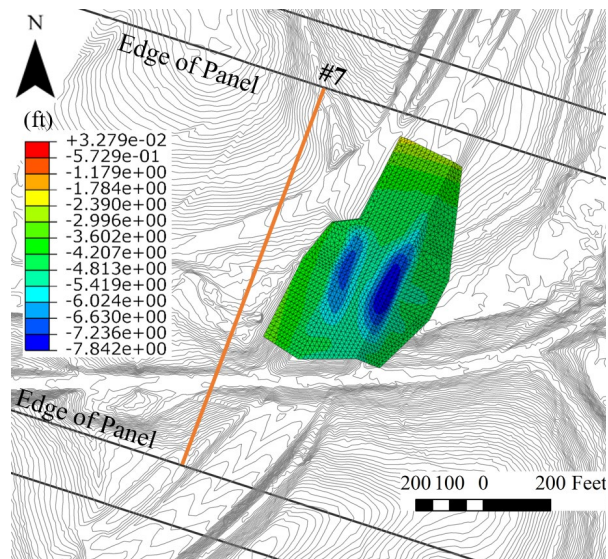
Appendix Figure 23 Vertical displacement on Embankment #5 with working face position #4



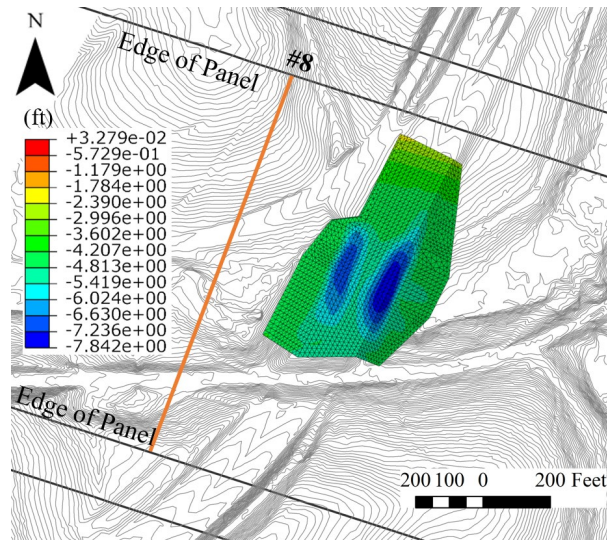
Appendix Figure 24 Vertical displacement on Embankment #5 with working face position #5



Appendix Figure 25 Vertical displacement on Embankment #5 with working face position #6



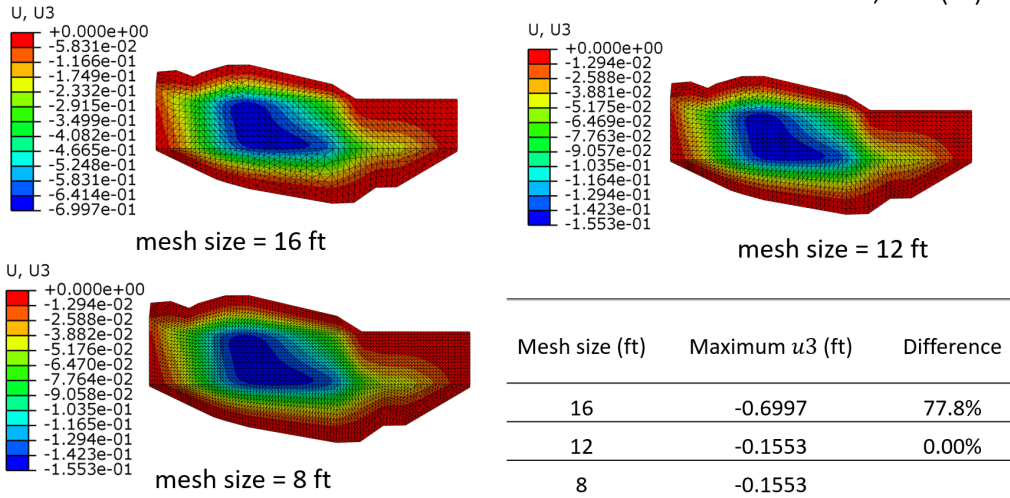
Appendix Figure 26 Vertical displacement on Embankment #5 with working face position #7



Appendix Figure 27 Vertical displacement on Embankment #5 with working face position #8

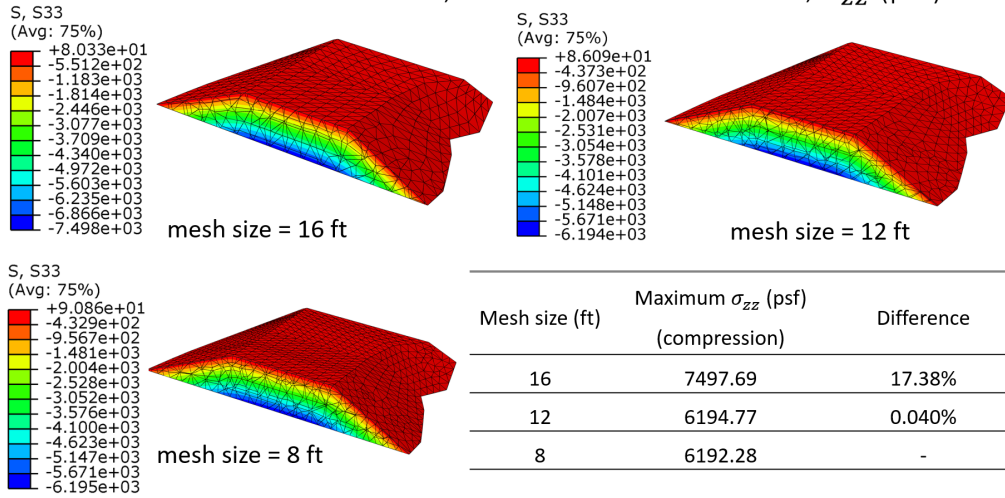
Appendix E Mesh Refinement Tests on Embankment #1

Mesh refinement tests –maximum vertical subsidence, u_3 (ft)



Appendix Figure 28 Mesh refinement tests with respect to the vertical subsidence

Mesh refinement tests – 3D, maximum vertical stress, σ_{zz} (psf)



Appendix Figure 29 Mesh refinement tests with respect to the vertical stress

Bibliography

- [1] Iannacchione, A., Vallejo, L, Li, Mingzhou, Adelson, E., and Winn, R. (2019). "Task 1: PreMining Activities Report: Identification of Factors Controlling the Development of Subsidence Impacts Forecasting Methodology to the I-70 Alignment over Longwall Mining of the Tunnel Ridge Mine," PennDOT Contract No. 4400011482, 2 July 2019, 129 p., available upon request to PennDOT or the University of Pittsburgh.
- [2] Iannacchione, A., Vallejo, L, Vandenbossche, J., Li, Mingzhou, Adelson, E., and Winn, R. (2020). "Task 2: Undermining Activities Report: Identification of Factors Controlling the Development of Subsidence Impacts Forecasting Methodology to the I-70 Alignment over Longwall Mining of the Tunnel Ridge Mine," PennDOT Contract No. 4400011482, 3 February 2020, 185 p., available upon request to PennDOT or the University of Pittsburgh.
- [3] Peng, Syd S., W. M. Ma, and W. L. Zhong. *Surface subsidence engineering*. Littleton, CO: Society for Mining, Metallurgy, and Exploration, 1992.
- [4] Jeran, Paul W., and Vladimir Adamek. *Subsidence due to undermining of sloping terrain: A case study*. US Department of the Interior, Bureau of Mines, 1988.
- [5] ABAQUS (2006). *ABAQUS Documentation*, Providence, RI.
- [6] Karmis, M., et al. "The prediction of ground movements caused by mining." *Proceedings of the third workshop on surface subsidence due to underground mining*. 1992.
- [7] Kratzsch, Helmut. "Mining subsidence engineering." *Environmental Geology and Water Sciences* 8.3 (1986): 133-136.
- [8] Reddish, D. J., and B. N. Whittaker. *Subsidence: occurrence, prediction and control*. Vol. 56. Elsevier, 2012.
- [9] Karmis, M., et al. "Mining subsidence and its prediction in the appalachian coalfield." *The 24th US Symposium on Rock Mechanics (USRMS)*. American Rock Mechanics Association, 1983.
- [10] Agioutantis, Z. and Karmis, M. (2017). SDPS: Surface Deformation Prediction System for Windows Version 6.2B (Quick Reference Guide and Working Examples). Blacksburg, Virginia, USA: Department of Mining and Minerals Engineering.
- [11] Agioutantis, Z., et al. *Prediction of ground movements due to underground mining in the eastern United States coal fields. Volume 1. Development of prediction methods. Final report*. No. PB-90-148594/XAB. Virginia Polytechnic Inst. and State Univ., Blacksburg, VA (USA). Dept. of Mining and Minerals Engineering, 1987.

- [12] Agioutantis, Z., et al. *Prediction of ground movements due to underground mining in the eastern United States coal fields. Volume 1. Development of prediction methods. Final report.* No. PB-90-148594/XAB. Virginia Polytechnic Inst. and State Univ., Blacksburg, VA (USA). Dept. of Mining and Minerals Engineering, 1987.
- [13] Naylor, D. J. "Finite elements and slope stability." *Numerical methods in geomechanics.* Springer, Dordrecht, 1982. 229-244.
- [14] Donald, I. B., and S. K. Giam. "Application of the nodal displacement method to slope stability analysis." *Fifth Australia-New Zealand Conference on Geomechanics: Prediction Versus Performance; Preprints of Papers.* Institution of Engineers, Australia, 1988.
- [15] Er-Xiang, Song. "Finite element analysis of safety factor for soil structures." *Chinese Journal of Geotechnical Engineering* 19.2 (1997): 1-7.
- [16] Chen, R. H., and J-L. Chameau. "Three-dimensional limit equilibrium analysis of slopes." *Geotechnique* 33.1 (1983): 31-40.
- [17] Ugai, Keizo, and D. O. V. Leshchinsky. "Three-dimensional limit equilibrium and finite element analyses: a comparison of results." *Soils and foundations* 35.4 (1995): 1-7.
- [18] Anthony T. Iannacchione, & Nicole E. Evaneck. (2018). 36 Years of Subsidence Reporting at the ICGM. *37th International Conference on Ground Control in Mining*, 37, 175–182. Society for Mining, Metallurgy & Exploration.
- [19] Zienkiewicz O.C., Humpheson, C., and R. Lewis. "Associated and non-associated viscoplasticity in soils mechanics." *Journal of Geotechnique* 25.5 (1975): 671-689.
- [20] Griffiths, D. V., and P. A. Lane. "Slope stability analysis by finite elements." *Geotechnique* 49.3 (1999): 387-403.
- [21] Matsui, Tamotsu, and Ka-Ching San. "Finite element slope stability analysis by shear strength reduction technique." *Soils and foundations* 32.1 (1992): 59-70.
- [22] Zheng, Ying-Ren, et al. "Geotechnical engineering limit analysis using finite element method." *Yantu Lixue(Rock Soil Mech.)* 26.1 (2005): 163-168.
- [23] Dawson, E. M., W. H. Roth, and A. Drescher. "Slope stability analysis by strength reduction." (1999): 835-840.
- [24] Matsui, Tamotsu, and Ka-Ching San. "Finite element slope stability analysis by shear strength reduction technique." *Soils and foundations* 32.1 (1992): 59-70.

- [25] Adelsohn, Emily, Anthony Iannacchione, and Robert Winn. "Investigations on longwall mining subsidence impacts on Pennsylvania highway alignments." *International Journal of Mining Science and Technology* (2020).
- [26] Iannacchione, A., Tonsor, S., Witkowski, M., Benner, J., Hale, A., & Shendge, M. (2008). A Summary of the PA DEP Observations on the Effects of Undermining Interstate 79 during the 3rd Assessment Period. In *The Effects of Subsidence Resulting from Underground Bituminous Coal Mining on Surface Structures and Features and on Water Resources, 2003 to 2008*(pp. IV_1-IV_26).
- [27] Yancich, R. D. 1986. *Surface Subsidence in Longwall Mining – A Case Study*. Master’s Thesis, Department of Mining Engineering, West Virginia University.
- [28] O’Connor, K. 2001. *The Effects of Undermining Interstate Route 70, South Strabane Township, Washington County, Pennsylvania*. Pennsylvania Department of Environmental Protection.
- [29] Gutierrez, Juan Jose. *Estimating highway subsidence due to longwall mining*. Diss. University of Pittsburgh, 2010.
- [30] Gutierrez, Juan J., Luis E. Vallejo, and Jeen-Shang Lin. *A study of highway subsidence due to longwall mining using data collected from I-79*. No. FHWA-PA-2010-009-PIT015. 2010.
- [31] Graybill, Franklin A. *Theory and application of the linear model*. Vol. 183. North Scituate, MA: Duxbury press, 1976.
- [32] Payne, Dan, et al. "Highwall stability implications from longwall mining at Broadmeadow mine." *Research Online* (2019): 91.
- [33] Sternik, K. "FEM analysis of road embankment on consolidating subsoil influenced by mining deformation." *PROCEEDINGS OF THE INTERNATIONAL CONFERENCE ON SOIL MECHANICS AND GEOTECHNICAL ENGINEERING*. Vol. 16. No. 3. AA BALKEMA PUBLISHERS, 2005.
- [34] Liu, H. L., Charles WW Ng, and Kang Fei. "Performance of a geogrid-reinforced and pile-supported highway embankment over soft clay: case study." *Journal of Geotechnical and Geoenvironmental Engineering* 133.12 (2007): 1483-1493.
- [35] Stilger-Szydło, Elżbieta, and Waldemar Tutaj. "Effect of mining deformations on stability of transport embankments." *Studia Geotechnica et Mechanica* 26.3-4 (2004): 3-22.
- [36] Clarkson, Luke. "Effect of punch longwall retreat on highwall stability." (2016).
- [37] Briaud, Jean-Louis. "Introduction to soil moduli." *Geotechnical News* 19.2 (2001): 54-58.
- [38] Wu, Tien Hsing. *Soil dynamics*. No. 272 pp. 1971.

- [39] Iannacchione, Anthony T., and Luis E. Vallejo. "Shear strength evaluation of Clay-Rock mixtures." *Slope Stability 2000*. 2000. 209-223.
- [40] Donaghe, R. T., and V. H. Torrey. "Scalping and replacement effects on strength parameters of earth-rock mixtures." *Proc. Conf. on Design Parameters in Geotechnical Engineering*. Vol. 2. 1979.
- [41] Miller, Eugene A., and George F. Sowers. "The strength characteristics of soil-aggregate mixtures & discussion." *Highway research board bulletin* 183 (1958).
- [42] Graybill, Franklin A. *Regression analysis: concepts and applications*. Duxbury Resource Center, 1994.
- [43] Johnson, Arvid M. *Physical processes in geology: A method for interpretation of natural phenomena; intrusions in igneous rocks, fractures, and folds, flow of debris and ice*. Freeman, Cooper, 1970.
- [44] Vallejo, L. E., et al. "The shear strength and stability of a soil mass containing dispersed large particles." *Landslides: evaluation and stabilization*. 2004.
- [45] Vallejo, Luis, and Sebastian Lobo-Guerrero. "The shear strength of granular materials containing dispersed oversized particles: DEM analysis." *International Journal of Geotechnical Engineering* 6.3 (2012): 371-380.
- [46] Julien, Pierre Y. *Erosion and sedimentation*. Cambridge university press, 2010.
- [47] Duncan, James M., and Chin-Yung Chang. "Nonlinear analysis of stress and strain in soils." *Journal of Soil Mechanics & Foundations Div* (1970).
- [48] Kulhawy, Fred H., and James M. Duncan. "Stresses and movements in Oroville Dam." *Journal of Soil Mechanics & Foundations Div* 98.sm7 (1972).
- [49] Xu, Yuan-jie, et al. "Development and implementation of Duncan-Chang constitutive model in ABAQUS." *ROCK AND SOIL MECHANICS-WUHAN- 25* (2004): 1032-1036.
- [50] Luo, Gang, and Jian-min Zhang. "Improvement of Duncan-Chang nonlinear model and Shen Zhujiang's elastoplastic model for granular soils." *ROCK AND SOIL MECHANICS-WUHAN- 25* (2004): 887-890.
- [51] Wang, Zhi-Liang, S. Mao-tian, and Zong-Ze Yin. "Analyses of parameters sensitivity of Duncan-Chang model in settlement calculation of embankment." *ROCK AND SOIL MECHANICS-WUHAN- 25* (2004): 1135-1138.

- [52] Wang, Zhi-liang, Zong-ze Yin, and L. Yong-chi. "Practical method for FEM analysis of embankment settlement with duncan-chang model." *ROCK AND SOIL MECHANICS-WUHAN*- 26.7 (2005): 1085.
- [53] MU, Sheng-yuan, and Zheng-zhong WANG. "Duncan-Chang Model Parameters Sensitivity and Statistical Analysis of Rockfills [J]." *China rural water and hydropower* 3 (2009).
- [54] Kondner, Robert L. "Hyperbolic stress-strain response: cohesive soils." *Journal of the Soil Mechanics and Foundations Division* 89.1 (1963): 115-143.
- [55] Kondner, Robert L., and Joseph Simon Zelasko. "Void ratio effects on the hyperbolic stress-strain response of a sand." *Laboratory shear testing of soils*. ASTM International, 1964.
- [56] Janbu, Nilmar. "Soil compressibility as determined by odometer and triaxial tests." *Proc. Europ. Conf. SMFE*. Vol. 1. 1963.
- [57] Si, H. B., and Z. E. Cai. "Development of static constitutive model library for soils based on ABAQUS." *Rock and Soil Mechanics* 32 (2011): 599.
- [58] Roscoe, K_ H_ . "The influence of strains in soil mechanics." *Geotechnique* 20.2 (1970): 129-170.
- [59] Griffiths, D. V., and Gordon A. Fenton. "Probabilistic slope stability analysis by finite elements." *Journal of geotechnical and geoenvironmental engineering* 130.5 (2004): 507-518.
- [60] Griffiths, Denwood V., and G. A. Fenton. "Risk assessment in geotechnical engineering." *John wiley&Sons, Inc* (2008): 381-400.
- [61] Griffiths, D. V., Jinsong Huang, and Gordon A. Fenton. "Risk assessment in geotechnical engineering: stability analysis of highly variable soils." *Geotechnical Engineering State of the Art and Practice: Keynote Lectures from GeoCongress 2012*. 2012. 78-101.
- [62] Griffiths, Denwood V., and Gordon A. Fenton, eds. *Probabilistic methods in geotechnical engineering*. Vol. 491. Springer Science & Business Media, 2007.